ARGONAUT

A Novel Detector for Very High Energy Neutrino Interactions

G. Harigel[†], H. Kautzky, P. McIntyre[‡], and A. Van Ginneken
Fermi National Accelerator Laboratory, Batavia, Illinois 60510

ABSTRACT

We propose to build a novel detector to study very high energy neutrino interactions. It consists of ten in-line modules, each containing a large cylindrical liquid argon bubble chamber and a magnetized iron spectrometer. Each bubble chamber is instrumented to provide segmented total-absorption calorimetry for all hadrons, photons, and electrons in the final state. A complete visual image with ~1 mm spatial resolution is provided in two stereo views. We envision using this detector to study a broad range of neutrino processes: 1) multi-lepton final states; 2) $\nu_\mu e \rightarrow \nu_\mu e$; 3) semi-leptonic scaling-variable distributions; 4) search for new phenomena in neutrino interactions using 1000-GeV protons from the Energy Doubler/Saver.

Fermilab Proposal No. 601

Scientific Spokesman:

Peter M. McIntyre
Fermilab and Harvard University

Telephone: (312) 840-4307

May 5, 1978

[†] On leave of absence from CERN.
[‡] On leave of absence from Harvard University.

143 pgs.

TABLE OF CONTENTS

Introduction

The Experimental Arrangement

A. Bubble Chamber

B. Ionization Calorimetry

C. Magnetized Iron Spectrometer

Neutrino Beam

Physics Objectives

Experimental Program

Conclusion

Introduction

We propose to build a novel detector to study very high energy neutrino interactions. The detector is optimized to identify and measure a broad range of neutrino processes: 1) multi-lepton final states; 2) $\nu_\mu e \to \nu_\mu e$; 3) semi-leptonic scaling variable distributions with large acceptance; 4) search for new phenomena in neutrino interactions using 1000-GeV protons from the Energy Doubler/Saver.

It is interesting to identify the features of a detector necessary to obtain maximum detail in studying these processes. The most obvious requirement is that the detector have a large mass active target--400 tons are required to produce approximately one event per day having a trimuon final state.[1] The second requirement is to obtain an actual picture of the event vertex. In studying rare processes, this picture helps one to distinguish clearly the process of interest from various backgrounds, such as π-μ decay in the case of multi-lepton events, and $\nu_e n \to e^- p$ in the case of $\nu_\mu e \to \nu_\mu e$. It also enables identification of K_s^o and Λ decays; in this way several bubble-chamber experiments[2] have observed enhanced strange-particle production in multi-lepton final states. The third requirement is to measure the energies and angles of all charged leptons, and the energy and angle of any hadronic system in the final state. An optimal detector must thus combine the visual imagery of a bubble chamber with the fine-grain calorimetry and muon identification of counter experiments.[3]

Happily, all of these tasks can be accomplished in a single detector. It consists of ten in-line modules, each containing a large cylindrical liquid

argon bubble chamber and a magnetized iron spectrometer (Figs. 1 and 2). Each liquid argon bubble chamber is instrumented to provide segmented total-absorption calorimetry for all hadrons, photons, and electrons in the final state. A complete visual image with ~1 mm spatial resolution is provided in two stereo views.

The bubble-chamber design described in this paper embodies several technological innovations: the use of liquid argon as fluid; electronic recording of bubble images on video tape; ionization drift over one meter distance; and a new approach to expansion bellows and cryostat design. Each of these features will be discussed in detail below. Final parameters in each case depend on prototype developement; plans for this development will be described.

The liquid argon bubble chamber serves four functions: 1) it is the massive target for neutrino interactions; 2) it provides a picture of the event vertex, and of decays and interactions of secondary particles, 3) it measures the energy E_H of the hadronic-electromagnetic cascades produced in semi-leptonic processes, and energy E_e of the electron in $\nu_\mu e \rightarrow \nu_\mu e$; 4) it aids in minimizing π-μ decay background for final-state muons by allowing identification of pion interaction kinks over several absorption lengths in liquid argon.

The magnetized iron toroid and drift chambers measure the charge momentum of high-energy muons originating in neutrino interactions in the bubble chamber.

The ten modules of the detector function largely independently, each having an event rate of ~0.2 per 10^{13} targeted protons. Separate events can be recorded in all ten modules during each beam pulse.

This detector is uniquely suited to search for new phenomena in neutrino interactions when the Energy Doubler/Saver begins producing neutrino beam. A dichromatic beam scaled from the new N-30 beam at Fermilab to accept 1000-GeV protons will produce neutrinos at energies up to ~800 GeV.[4] This new energy region promises to be at least as rich in new physics as the present one has been: 1) the $W^{\pm}$ propagator for $M_W = 60$ GeV/c^2 modulates the linearly rising neutrino cross section by ~20% at $E_\nu \sim 700$ GeV; 2) new flavors or quarks should evidence themselves through flavor cascades and soft multi-lepton events,[5] and anomalies in scaling-variable distributions;[6] 3) asymptotic freedom requires a sizable gluon contribution to neutrino scattering $E_\nu > 100$ GeV[7]--the extent of this contribution and its Q^2 dependence are of strong interest in quantum chromodynamics (QCD); 4) if there are new heavy leptons produced in neutrino interactions, the decay $L^o \to \mu^{\mp} \ell^{+} \nu_\ell$ should give an interpretable signal in multi-muon events via the μ^-/μ^+ momentum balance limits of Pais and Treiman;[8] 5) the production of Higgs bosons should increase with E_ν faster than the total cross section,[9] a search in neutrino interactions with $E_\nu \gtrsim 600$ GeV should be sensitive for masses $M_H \lesssim 10$ GeV/c^2.

We believe that the detector described here improves in many respects the information available from existing and planned detectors. With it we can advance into the frontiers of neutrino physics--the detailed study of rare leptonic processes, and the exploration of the new energy realm of the Energy Doubler/Saver.

The Experimental Arrangement

One module of the complete detector is shown in Fig. 1. The liquid argon bubble chamber has an enclosed volume of 10m length x 2. 5m diameter. Ionization electrons are drifted to a collection tube on the axis of the chamber. There they are collected in 1 7 cm longitudinal segments, amplified, and the charge is recorded as a function of drift time (hence radius). In this way we achieve fine-grain total-absorption calorimetry, segmented each radiation length in depth. An Fe-Ar or U-Ar calorimeter following the bubble chamber assures complete containment of all showers occurring within the fiducial region.

Following the bubble chamber are two magnetized iron toroids. Each toroid is 1 m thick × 7 m diameter, and is magnetized to saturation. Following each toroid are two planes of large area drift chambers which are used to measure the trajectories of muons from a neutrino interaction in the preceding bubble chamber.

The complete detector consists of ten such modules stacked in line. It is shown in Fig. 2, located behind the existing experimental areas (Labs A, C, E). Its overall length is 180 m. The bubble chambers contain in total 600 tons of liquid argon, and the toroids contain in total 6000 tons of steel.

A. Bubble Chamber

The bubble chamber uses liquid argon as its working fluid. The choice of argon derives from a number of considerations:

1) We require good electron identification and calorimetry; the ratio A/X of hadron absorption length A to electron radiation length X should thus

be maximum. We also require accurate measurement of angles θ_e, θ_H. Assuming a position measurement accuracy of δ = 1 mm, an intrinsic angular resolution can be defined as $\theta_H = \delta/A$ for hadrons, and $\theta_e = \delta/6X$ for electrons. The latter estimate uses the statistical development of an electron shower, peaked at ~6X, as will be discussed later. Figure 3 shows A/X vs. θ_H and θ_e for various materials. The joint requirements $A/X > 5$, $\theta < 2$ mrad are satisfied by only two materials: argon and Freon CF_3Br.

2) Argon does not attach electrons, so that long-drift ionization calorimetry is possible. The electron mobility is large, permitting drift collection over 1 m drift length in ~300 μsec. Electron drift is of course impossible for Freon CF_3Br.

3) Argon is abundant--indeed it comprises 1% of the air we breathe. Its cost, approximately $200 per ton, is easily affordable.

4) Argon is chemically inert and hence readily purified. It is non-toxic and non-inflammable, so that safety is easily assured.

5) Argon can be liquefied using liquid nitrogen. The cryogenic system is thus much simpler than one for neon or hydrogen.

6) Argon requires a rather modest expansion system for bubble-chamber operation. The operating pressure P is ~12 bar, compared with 18 bar for CF_3Br. The expansion ratio $\Delta V/V$ is ~(0.5 - 1)%, compared with 3% for CF_3Br.

These considerations, many of which have been detailed previously by Rubbia,[10] lead to the choice of argon as a truly optimum material for an active neutrino target.

Magnetic Field

There is no magnetic field on the liquid argon bubble chamber. This represents a major departure from conventional thought in bubble-chamber physics. To understand its motivation, consider the traditional functions of a magneticfield in a neutrino bubble chamber and how these can be accomplished in the proposed detector:

1) momenta of muons--we measure $\overline{p}_\mu$ to an accuracy of 12% in the magnetized iron toroids.

2) V^o reconstruction--we can identify V^o's in the bubble-chamber pictures, although we cannot of course distinguish K_s^o from

3) momenta of electrons--we measure E_e by calorimetry to good accuracy, although we cannot measure its sign. (Because of the short radiation length, the strongest realistic magnetic field could not measure sign in liquid argon for $E_e \gtrsim 10$ GeV.)

4) $e^\pm$ pairs from γ conversion are opened in a magnetic field--this is useful to eliminate $\nu_\mu p \to \nu_\mu p\pi^o$ events as a background for $\nu_\mu e \to \nu_\mu e$. We cannot readily distinguish such pairs from single electrons without magnetic field. However, we hav complete conversion and detection acceptance for photons. In such an event, we would see two pairs and a proton sharing a common vertex at the ν_μ interaction point--quite distinct from $\nu_\mu e \to \nu_\mu e$. Also, the π^o process is dominated by $\Delta(1232)$ production,[11] and can be kinematically isolated from the process of interest.

5) reconstruction of other secondary momenta--for the physical processes addressed in this proposal, this is useful only to obtain $\vec{p}_H$ of the hadronic vertex (hence x and y). $\vec{p}_H$ is here measured simply and accurately in the liquid argon calorimetry.

Thus we need not rely on magnetic analysis in the bubble chamber for any essential information in the study of neutrino interactions proposed here.

Bubble Chamber Properties of Argon

For unknown reasons, argon has never been used in a bubble chamber. In what follows, we attempt to estimate its operating conditions for optimum bubble formation, using its known thermodynamic properties. Table I summarizes for various bubble-chamber liquids the properties needed for calculation of bubble creation and growth. It includes established operating conditions of these liquids in large bubble chambers.

We can estimate the operating temperature for argon using the data for the other nobles gases neon and xenon (We exclude helium because of its unique thermodynamic properties). The operating point T in each case is roughly midway between the normal boiling point T_b and the critical point T_c:

$$\alpha = \frac{T - T_b}{T_c - T_b} = 0.5 \text{ for Ne, } 0.7 \text{ for Xe.}$$

The operating point for Xe was probably chosen somewhat high by the designers of the few existing chambers because of availability of commercial refrigerators. The choice $\alpha \sim 0.6$ for argon thus seems proper, implying

$$T = \alpha(T_c - T_b) + T_b \sim 120 \text{ K}.$$

The vapor pressure of argon at this temperature is $P_v \sim 12$ bar. In this respect argon presents a distinct advantage over propane and Freon and their mixtures, whose vapor pressures are 18-22 bar.

The theory of Seitz[12] assumes that bubbles are formed by heat spikes released in ion recombination at the end of energetic δ-rays. In order to be useful for bubble formation, energy must be deposited inside a sphere of critical radius r_c. The fluid pressure must be reduced rapidly by an amount ΔP, so that the critical bubble can grow independently in the now superheated fluid. ΔP and r_c are related by

$$r_c = 2\sigma/\Delta P,$$

where σ is the surface tension of the liquid at vapor pressure P_v. From a recent study by Wolff,[13] the critical radii for H_2 and D_2 are 100 Å and 150 Å. We estimate $120 < r_c < 150$ Å for argon. The pressure drop is hence $7 < \Delta P < 9$ bar.

Detailed calculation of bubble formation energy and bubble density is perilous, since such calculations for common bubble chamber fluids agree only qualitatively with observed properties. We can however make a reliable estimate of macroscopic bubble growth:

$$r(t) = \frac{2(T - T_e)}{H\rho_v} \sqrt{3k\rho c_p/\pi}\ \sqrt{t},$$

where all constants are defined in Table I, and ρ_v is the vapor density at equilibrium vapor temperature T_e corresponding to expanded pressure $P_e = P_v - \Delta P$. The vapor pressure P_v and vapor density ρ_v are plotted in Fig. 4.

Choosing $\Delta P = 8$ bar, we find $T_e = 102$ K, $\rho_v = 0.02$ g cm^{-3}. Inserting all values in the above expression for r(t) we obtain

$$r/\sqrt{t} = 0.34 \text{ cm s}^{-\frac{1}{2}}.$$

This growth rate is comparable to rates obtained in large bubble chambers using H_2 and D_2. The bubble grows to a radius 0.3mm in a time $\tau \sim 8$ ms.

The static (or chamber) pressure must be always higher than the equilibrium vapor pressure at a chosen liquid temperature in order to recompress bubbles and prevent boiling between expansion cycles. In cryogenic bubble chambers, using H_2, D_2, neon, and neon/H_2 mixtures, an overpressure of one bar is sufficient; we assume the same will be true for argon, i.e., the chamber pressure will then be about 13 bar. We must obtain a total pressure drop of ~9 bar.

The expansion ratio required to produce this pressure change has two contributions. An adiabatic PV cycle requires $\Delta V/V = \beta \Delta P$, where β is the isentropic compressibility. This corresponds to $\Delta V/V = 0.25\%$ for $\Delta P = 9$ bar. In a practical chamber, the parasitic boiling from the surfaces of the chamber and along the particle tracks creates a vapor load during operation. The vapor load increases the effective compressibility and can easily double the required expansion ratio. We estimate that an expansion ratio $\Delta V/V \lesssim 1\%$ allows comfortable operation for liquid argon.

With the expansion membrane arranged along the cylindrical wall, the pressure wave travels a distance of only ~2.2 m to expand all of the chamber liquid. The total cycle should last about 100-200 ms. This fairly long duration presents three advantages:

1) long sensitive time (20 ms), to accomodate beam jitter or long spill,

2) homogeneous sensitivity across the visible volume,

3) minimization of vibrations in the chamber vessel.

A long cycle duration does however increase parasitic boiling and dynamic heat load, which may adversely influence track position and reconstruction accuracy. An optimum cycle must be found in actual operation.

In conclusion one can state that almost all thermodynamical and physical properties of argon, as given in Table I, are well within the range of values for liquids in use today. The heat conductivity of liquid argon is large enough to assure proper regulation of uniform temperature throughout the chamber liquid. It is clear, however, that experimental tests in a small bubble chamber are crucial to further specify operating characteristics.

Operational tests of bubble-chamber operation with argon will clarify two other uncertainties. First, argon is a scintillator. It may turn out that ionizing high-energy particles, traversing the liquid, deposit only a small part of their energy in heat spikes, but most of it as light. The latter energy is then unavailable for the creation of a critical bubble. This kind of effect arises in xenon and is cured by adding a few per cent of ethane as a light-quenching agent. Scintillation in argon is expected to be slightly more than in neon but less than in xenon. If scintillation is troublesome and must be quenched, there are several liquids which mix with liquid argon: CH_4, H_2, and C_2H_6. A successful additive would have to 1) quench scintillation; 2) not affect bubble-chamber operation; and 3) not attach electrons during ionization calorimetry. Clearly, operational tests are required.

Second, argon has a radioactive isotope with relatively long lifetime: Ar^{39}, 265 years, β^- 0.56 MeV. Ar^{39} is a cosmogenic radionuclide, made in cosmic-ray collisions by K^{39} (n,p) Ar^{39}, Ar^{38} (n,γ) Ar^{39} and spallation. Its abundance in atmospheric argon has been measured:[14] $Ar^{39}/Ar^{40} \simeq 7\times10^{-16}$. In the bubble chamber, a camera would see ~40 decays/m^2 during the chamber sensitive time of 20 msec. The mean β energy corresponds to a range of ~0.5 mm. Thus each β should make one bubble.[15] This small background is comparable to the frequency of blemishes in the CCD arrays (~10^{-4}), and should be no problem. If it is troublesome, we could use argon purified from well gas. It constitutes ~0.1% of typical well gas, and it is essentially free of Ar^{39}.

Pressure Vessel and Cryostat

The bubble-chamber pressure vessel is 11 m long × 2.5 m diameter. Its construction is detailed in Fig. 5. The pressure vessel is made of 2.5 cm thick stainless-steel plates which are rolled and welded. Onto the outer wall is welded a pattern of stainless-steel tubes, each 15 cm long × 5 cm diameter × 1 mm wall thickness. These tubes are welded end-on to the pressure vessel, in a 30 cm grid. The outer end of each tube is capped by a G-10 disc. A thin (1.5 mm) stainless-steel membrane is then stretched over the tube grid and seam-welded to form a vacuum enclosure. When evacuated, the membrane is pressed against the tubes to form a stable catenary surface.

A 1 cm stainless-steel tube runs parallel to each longitudinal row of support tubes, spaced 1 cm from the pressure vessel wall. The tube is wrapped once around each support tube and brazed to its surface. High-pressure liquid nitrogen (LN_2) flows through these tubes, providing a heat

barrier to control the pressure vessel temperature. By varying the boiling pressure of the LN_2 in the tubes, we can stabilize the bubble chamber at any desired operating temperature from 80 K (P_v = 20 psi) to 122 K (P_v = 400 psi). Returning LN_2 is heat-exchanged in a cold box with normal LN_2 (77 K) to complete the cooling circuit. The boil-off vapor from the cold box flows through a second set of tubes, wrapped around each support tube half-way along its length. The vapor thus precools the support tubes and intercepts approximately one-half the heat leakage before it reaches the pressurized LN_2 loop on the bubble chamber wall.

The heat load conducted through the support tubes to the LN_2 heat exchanger is $Q_c \sim 1$ kW per module. The heat radiated from the vacuum membrane to the pressure vessel is Q_r = 4 kW. The radiative load can be reduced by a factor of ~10 by locating a multi-layer sandwich of super-insulation foils over the entire surface between support tubes, alternate layers running longitudinally and azimuthally on the pressure vessel wall. The total heat load to the pressurized LN_2 is then $Q \lesssim 1.5$ kW per module or $Q_T \sim 15$ kW for the entire detector.

In the heat exchanger the heat is removed by boiling LN_2. The heat of vaporization of LN_2 is H = 200 J/g = 160 KJ/liquid liter. The closed loop refrigeration system thus uses Q_T/H = 350 liters per hour of LN_2. A large LN_2 storage tank provides buffer capacity and open loop refrigeration in event of a power failure.

It is essential in a large bubble chamber to avoid temperature variation within the liquid volume. This can occur if local cells are allowed to stabilize by density stratification. The heat-exchange system described above

allows a particularly simple way of avoiding this problem. We can regulate the pressure in the cooling tubes to achieve a slight temperature gradient across the chamber: warmer (higher LN_2 pressure) at the bottom than at the top. This forces a natural convection in the chamber volume and prevents cell formation.

The one-body Dewar design provides mechanical strength at low cost, modest heat load, and easy access for supports, expansion valves, and optics ports. One end is flanged to provide access for assembly and maintenance inside.

Expansion System

The expansion system is shown in Fig. 6. A stainless-steel base plate, 10 m long × 1 m wide × 2.5 cm thick, is seam-welded to the wall of the cylindrical vessel along its entire length. The expansion plate, 8 m long × 1 m wide × 7 cm thick, is suspended above the base plate with a 20 cm space between them. It is made of low-density aluminum honeycomb, with a thin metal skin laminated to each face. It is supported in the chamber by a series of cold gas expansion valves.

The space between plates is sealed by a U-shaped membrane of thin stainless steel, bowed inward and seam-welded to each plate along its edge. Hydrostatic pressure forms the membrane to a half-circle cross section, with excess length pressed flat to each plate wall. The membrane is loaded almost only in tension. To expand the chamber the expansion plate is

stroked toward the base plate; the membrane deforms to a somewhat smaller radius, displaced inward between the plates.

It remains to seal the U-membranes at each end of the expansion plate. At the end of the base plate, a vertical end block is mounted, 18 cm high, 1 m wide, and 2.5 cm thick. The expansion plate tapers in thickness during the last 1 m at each end, and it is welded to each end block as shown in Fig. 6. The U-membrane continues right up to each end block and is seam-welded to it across the full contour of the U. The displacement stroke grows in amplitude from 0 to full stroke during a 1 m length inward from each end block. An expansion ratio $\Delta V/V = 1\%$ requires a stroke of 5 cm.

Two features of this design are highly advantageous for stable, long-life performance:

1) the membrane is in a configuration of static and dynamic stability and minimum stress;

2) the seam welds between membrane and plates have no flexion at any point in the expansion cycle. This latter feature is quite important for long membrane life.

Optics

The camera port design is shown in Fig. 7. It consists of a set of two hemispherical (fisheye) windows, a wide-angle lens having about 110° total opening angle, and a visual charged-coupled-device (CCD) array in the focal plane. The space between the fisheye windows and between the small window and the lens are evacuated in order to maintain the lens and image plane at ambient temperature.

The dimensions of the two windows of a fisheye set should be as small as possible for thermodynamic and financial reasons. Using as a guideline the small windows of the 15-ft bubble chamber, we envisage outer diameters of 25 and 15 cm, respectively. Both windows will probably be made of quartz, cut from the same block. This allows rapid cooldown and warmup of the chamber, and provides maximum safety.

The photographic lens has a small front element ($\lesssim$ 5 cm diameter) to provide adequate space for the illumination system, which is close to the optical axis. Barrel distortion of $\lesssim$ 20% of the lens at the border of the image is acceptable from the point of view of reconstruction with each camera pair, and of connecting track images from pair to pair.

The bubble chamber is viewed by two rows of five cameras, paired along the length of the chamber. Each pair provides 90° stereo views as shown in Fig. 1. Figure 8 shows a cross section of the chamber and the projected limits of the field of view. One limit is the 60 cm minimum depth of focus; a second is the intersection of the 110° acceptance cones for adjacent cameras. There is a 2.0 m diameter fiducial region in which acceptance is 99%.

The focal length of the overall assembly--its two windows, the lens, and the refractive chamber liquid--is about 30 mm. We hope to use a commercially available lens, thus saving development costs. The depth of focus should reach from about 60 cm up to 250 cm distance from the lens (40% light intensity in the center of the image as compared to the image in the object focal plane).[12] An F-stop of 17-20 is appropriate.

There are a total of 100 cameras in the complete detector. We could achieve 1 mm spatial resolution using inexpensive 35 mm film cameras. An appealing alternative is the use of visual charge-coupled-device (CCD) arrays to record the bubble images on video tape. The technology of large CCD arrays is today achieving commercial viability and has been used to advantage in recording streamer-chamber tracks.[18] Fairchild now markets a 256 × 256 element array,[19] and is developing a 388 × 480 element array. With the advent of new production techniques (such as using short-wavelength synchrotron light for mask registration,[20]) it is likely that element spacing will decrease and array size increase markedly in the coming two years. Growing demand and volume production can be expected to reduce cost.

The arrays can be readily mounted side-by-side in a larger matrix to form a 2000 × 2000 array, corresponding to 1 mm spatial resolution. The space between the active areas of adjacent arrays is ~ 5% and 10% in the two dimensions. This dead region might cause some inconvenience in track reconstruction; optical beam splitters could be used to piecewise displace the images and eliminate the gaps.

The properties of CCD image sensor arrays are well-suited to bubble-chamber photography. The CCD stores a charge proportional to the incident light energy ($\Gamma \simeq 1$). Saturation occurs at 0.2 $\mu J/cm^2$; average peak dark signal corresponds to ~0.6 nJ/cm^2. The useful signal/noise ratio is thus S/N ~ 100:1. The sensitivity and element spacing are each about a factor 2 larger than the typical values for bubble-chamber film used today.

One other important aspect of the camera design is the image size. A CCD image sensing element has dimensions of 14 $\mu m \times 18$ μm. Projecting such an element backward with the proposed optics into the object space results in 0.4 × 0.5 mm. This corresponds to the resolution when only one image sensing element is centrally illuminated by light rays from a bubble in dark-field illumination (or not being illuminated, in bright-field). Because each bubble will probably grow to about 0.6 mm diameter, its image may be seen by two neighboring cells. For this resolution, the quality requirements on lens and window design and manufacturing are moderate.

For bubble-chamber illumination we choose bright-field illumination, as shown in Fig. 7. The chamber's interior would be wallpapered with Scotchlite reflector.[21] The light source has its virtual origin close to the entrance pupil of the lens. This is achieved using a light pipe parallel to the lens and projected via a prism into the liquid. This scheme for illumination, suggested by Ballam, eliminates the small-radius ghost image observed by Freytag[22] when using a ring flash tube around the optics port. The bubble shadow should provide an ~3:1 modulation of ambient bright-field illumination. We estimate an illumination of ~0.1 $\mu J/cm^2$ in the image plane, well matched to CCD sensitivity.

Dark-field illumination from ~90° would also be possible in liquid argon. The relatively large refractive index (1.19) produces a more gradual decrease of the geometrical scattering function (Fig. 9) than in the case of hydrogen or neon. The required flash-tube arrangement is complicated, however, and requires image baffles between tubes and camera; for this reason we prefer bright-field illumination.

Visual Analysis

Readout of the CCD cameras involves shifting the charge out in bucket-brigade fashion, at a rate of 250 kHz (see Fig. 10). This clock rate corresponds to the input data rate for a typical analog video-tape recorder[23] using modest tape speed. The CCD output level (0-1 V) interfaces directly to the video-tape input buffer. The video tape reproduces stored analog information with a signal/noise ratio S/N = 100:1, well-matched to the CCD performance.

Each CCD camera ($2000 \times 2000 = 4 \times 10^6$ analog bits) is recorded on an individual video-tape channel. The 10 cameras on each module thus occupy 10 channels on a 14-channel video tape. Two channels are used to record digitized charge information from the liquid argon calorimetry (see Section B). The total recording time for an event is 13 seconds (higher recording speeds can be accommodated if necessary, up to 2 MHz). Each tape will accommodate 2 hours of continuous recording.

Electronic image recording provides great flexibility in its use on the bubble chamber. First, we can use ionization and drift-chamber information to decide whether an interesting event occurred in each module. If not, its

images need not be recorded. Second, the record format on video tape is a television scan raster with contrast. We can thus reproduce the image directly onto a television or high-resolution plotter with no computer interface. Selection of track information relevant for analysis can then be performed using a light pen, and the (much reduced) information transferred to an input buffer for computer analysis. Furthermore, the track information is already digitized by the readout format. A simple threshold requirement can be used to identify bubbles in the selected track region. The total measuring and computing requirements of this detector should thus be much more modest than those for film analysis, and should allow rapid analysis of events.

B. Ionization Calorimetry

The ionization calorimetry arrangement is shown in Figs. 1 and 11. The entire volume of liquid argon is used as a drift-ionization calorimeter, sampled each radiation length to resolve in detail the shower development. An Fe-Ar or U-Ar calorimeter similar to Willis' design[24] is located behind the chamber and provides total containment over the full length of the chamber. This arrangement permits us to 1) measure hadron energy electron energy E_e; 2) identify single electrons for $\nu_\mu e \rightarrow \nu_\mu e$; 3) measure energy flow in neutral current interactions; 4) extend muon identification to the lowest possible momenta to obtain flat acceptance in the scaling variables x, y, and maximum detection efficiency for multi-lepton events.

Electron Drift

The mobility of electrons in pure liquid argon has been studied extensively.[25,26] Figure 12 shows the field dependence of drift velocity.

The electron velocity is proportional to applied field (constant mobility μ_0) up to the velocity of sound ($u = 0.85 \times 10^5$ cm/sec). For higher fields ($E > 200$ V/cm), the velocity increases more slowly with applied field and saturates at ~ 10u. In the range 1-50 kV/cm,

$$v \simeq 2.1 \times 10^5 \, E^{1/3} \text{ cm/sec},$$

where E is in kV/cm.

The low-field mobility gradually decreases with increasing temperature.[26] At our operating point μ_0 (120 K) ~ 0.6 μ_0 (84 K).

Swan[25] has studied the effect of impurities on drift velocity. A small concentration (0.24%) of hydrogen in solution increases the drift velocity by about a factor 2 (see Fig. 12). This effect may prove useful in achieving uniform collection in the chamber volume.

Drifting electrons are readily attached by an electronegative impurity, such as oxygen or to a lesser extent nitrogen. The attachment process has been studied by several authors.[27] Its cross section is a rapidly decreasing function of average electron energy. The corresponding attachment length λ is observed to increase linearly with applied field E:

$$\lambda p/E = 0.15 \text{ ppm cm}^2/\text{kV},$$

where p is the concentration of O_2. We thus require an oxygen concentration < 1 part per billion in order to provide efficient drift over 1 m distance.

We would achieve this purity by mixing a small quantity of hydrogen with welding-grade argon gas and passing it through a catalytic mesh to induce $2H_2 + O_2 \rightarrow 2H_2O$ with high efficiency. The resulting water content is readily removed in the liquefication process. The liquid argon, once clean,

should stay cleanfor long periods, since each chamber is sealed and surface gas diffusion is insignificant at cryogenic temperatures.

Figure 13 shows the collection time and charge fraction as a function of radius.

Charge Collection

The scheme for ionization calorimetry is shown in Fig. 11. Ionization electrons from a neutrino interaction are collected on a thin tube, supported by insulators on the axis of the bubble chamber, and held at high voltage (+ 500 kV) with respect to the body of the chamber. This tube produces a radial electric field E(r) = 100 kV/r, where r is in cm. It is segmented longitudinally into lengths X = 17 cm.

Each drifting electron induces an image current on the collection tube:

$$i(r) = ev(r)/r \ell n\,(R/r_0),$$

where R and r_0 are the radii of the chamber and collection tube, respectively. The total induced charge at collection is

$$q(r) = e\frac{\ell n\,(r/r_z)}{\ell n\,(R/r_0)}.$$

The induced current distributes over a length $z \sim r$ of the tube. But we wish to segment the ionization calorimetry in slices $\delta z \sim X = 17$ cm. Hey, presto, we reinvent the triode. We insert a grid on radius $r_g \sim 2r_0$. The grid is held at neutral potential so that is is transparent to the drifting electrons. No charge is induced on the collection tube until an electron passes through the grid. The result is 1) localized charge collection; 2) constant charge response--the total induced charge is now $q \equiv e$, independent of where an electron starts.

The collection tube is a hollow plastic cylinder, vented to the chamber. Its outer surface is copper-clad, with narrow circular bands etched to form

discrete conductor segments of length δz = 17 cm. A signal lead connected to each segment connects through a hole in the tube to the FET receiver of a charge-sensitive amplifier mounted in the bore of the collection tube.[28] A JFET driver transmits the resulting voltage signal down a balanced transmission line to the end of the chamber. Each chamber contains a total of 60 segments. All signals emerge through a ceramic feedthrough in the upstream end dome. The final amplifiers and digitizing electronics are mounted outside on this feedthrough, in a large SF_6-filled enclosure. They are powered by storage batteries to avoid isolation difficulties.

Radeka[24] has calculated the optimum equivalent noise charge Q_n of a charge-sensitive amplifier on an ionization calorimeter:

$$Q_n = 4\ e_n\sqrt{2C_dC_a/\tau}$$

The segment capacitance is $C_d = 700\ \varepsilon\ \delta z/\ell n\ (r_g/r_0)$ = 240 pF. The amplifier input capacitance is $C_a \sim 30$ pF. The resolving time is $\tau \sim 1\ \mu$sec. The rms spot noise for the amplifier FET is $e_n \lesssim 1\ nV/\sqrt{Hz}$. Optimum noise charge is then $Q_n \sim 5\times10^{-4}$ pC.

The analog signal from each segment is clocked into a 256-channel linear CCD array at a rate of ~ 1 MHz. In this way we provide radial segmentation of ~ 1 cm in the ionization measurement. The charge stored in each CCD element is then converted to digital format using a 10-bit ADC.

A parallel data bus accesses all 60 ADC's; clock, address, and data lines connect via light links to receivers at ground potential. The digital data is stored temporarily in a RAM, and pulse-encoded onto two channels of the video-tape recorder.

Calorimetry for Minimum-Ionizing Tracks

The energy loss per ion-electron pair in liquid argon is W = 24 eV. The charge release per GeV of ionization is $dQ/dE = e/W = 6.7$ pC/GeV. The line density of ionization from a minimum-ionizing track is then $dQ/dz = \frac{e}{W}\frac{dE}{dz} = .014$ pC/cm. In one sample length this yields $Q_o = X\ dQ/dz = 0.24$ pC. The electronic noise $Q_n = 5\times10^{-4}$ pC corresponds to a signal/noise ratio S/N = 500 for a minimum ionizing track.

The r.m.s. fluctuation of the number N_e of electron-ion pairs produced by ionization is $N_F = \sqrt{F\ N_e}$, where F is the Fano factor [29]. For liquid argon, F = 0.10 [30] and the charge fluctuation on a minimum ionizing track segment is $Q_F = \sqrt{F \cdot Q_o \cdot e} = 6\times10^{-5}$ pC. Fluctuations are thus less than electronic noise for less than 8 minimum ionizing tracks per segment.

Electromagnetic Cascades

In an electromagnetic cascade, nearly all energy is converted into ionization, and nearly all cascade tracks are minimum ionizing (e^+, e^-). Figure 14 [31] shows the cascade development in liquid argon for various electron energies. We have calculated cascade development using the Monte-Carlo program AEGIS [32] to study both longitudinal and lateral cascade development. Essentially complete (>99%) containment is obtained in a length ~20 X, radius ~X from interaction vertex. Angular measurement σ_θ~1.5 mrad

should be possible using the statistical shower development up to its peak population.

For electron calorimetry, the resolution on ionization is determined by noise and Fano fluctuations. Assuming complete containment in 20 X, we have

$$\sigma_E = (dQ/dE)^{-1} \sqrt{20\ Q_n^2 + Q_p^2} = \sqrt{(3.3\times10^{-4})^2 + (5\times10^{-5})^2\ E}$$

σ_E varies from .3 MeV to .6 MeV for electron energies from 1 GeV to 100 GeV.

Hadron Showers

We have calculated shower development for hadrons of various energies, using the Monte-Carlo program CASIM [33]. The hadron shower process is more complex, with energy being distributed to 1) charged secondaries (~40 %); 2) π^o's, hence electromagnetic cascade (~40 %); 3) π, K rest mass, released in part as ionizing particles (μ, e) in their decay (~5 %); 4) nuclear excitation (~15%).

Energy resolution of hadron calorimetry is mainly determined by containment (*absorption length A = 90 cm*) and *fluctuations in* the way the incident energy is distributed among the above mechanisms. Figure 15 shows the fraction of total energy contained and detected as ionization, as a function of length and radius from beam center. Here we have assumed the initial hadron is produced by an interaction occuring with equal probability anywhere in a 0.4 m radius neutrino beam. This corresponds approximately to the K-decay neutrino distribution in the new dichromatic beam [4]. We achieve near total containment in the

1.25 m radius of the liquid argon chamber. A total absorption Fe-Ar or U-Ar calorimeter is located immediately following the chamber vessel to provide full longitudinal containment for any hadron originating in the chamber volume.

We have simulated showers for hadron energies from 10 GeV to 200 GeV. The detected ionization is proportional to the initial hadron energy (fig.16). The containment is essentially complete for hadrons having angles $\theta_H < 10^o$. For larger angles, some energy escapes radially for interactions in the upstream part of the chamber, as shown in Fig.17. By restricting fiducial volume to the downstream 7 m, we can extend calorimetry up to angles $\theta_H \sim 20^o$.

The fraction (~15 %) of hadron energy deposited in nuclear excitation, ultimately produces low-energy protons, neutrons and nuclear fragments. The tracks of these particles have large specific ionization. Column recombination [31] limits the fraction η of ionization which can be separated from the ionization column. Fig.12 shows η_α as a function of drift field E. Fluctuations in the fraction of energy going to nuclear excitation will probably limit hadron energy resolution to $\sigma_E/E \sim 5 - 10$ %.

The intrinsic accuracy of angle measurement θ_H is $\sigma_\theta \sim \delta/A = 1.1$ mrad. The multiple scattering error is $\sigma_{ms} = \frac{.015}{\sqrt{3}\,p}\sqrt{A/X} = 20$ mrad/p. The actual measurement error is the larger of the two for any given momentum p.

Compatibility of Calorimetry and Bubble Chamber Operation

The combination of ionization calorimetry and bubble chamber operation is a unique feature of this detector. It is important to examine the compatibility of the two techniques.

1) Electron drift does not affect the bubble formation process. Bubbles form around heat spikes from high energy δ-rays, as discussed earlier. An energy of ~1000 eV is deposited in a cell of critical radius r_c ~ 150 Å. This corresponds to ~40 electron-ion pairs, with local space charge field $E_o = \frac{\varepsilon q}{4\pi \varepsilon_o r_c^2}$ ~ 4 MV/cm. at the critical radius. The applied field thus should not hinder the local recombination process that releases heat for bubble formation.

2) Bubble formation does not hinder electron drift for calorimetry. Ionization electrons not originating in a heat spike begin immediately to drift toward the chamber axis with a velocity $v_\perp$ ~ 5×10^5 cm/sec. Meanwhile bubbles grow to a radius 0.3 mm in a time τ ~8 msec. The drifting electrons have by then been collected and recorded for calorimetry.

3) The bubble chamber expansion cycle may affect ionization grid/collector system in two ways. First, any motion of grid with respect to collector causes a variation in capacitance and hence induced charge (microphonics). Second, the volume expansion produces a ~0.25 % change in density and a corresponding change in dielectric constant. Each of these effects may be understood as a change in capacitance C_d = 240 pF between collector and grid:

$$\frac{\partial C_d}{\partial r_g} = -\frac{C_d}{r_g \ln(r_g/r_o)} \qquad \rho \frac{\partial C_d}{\partial \rho} = C_d(\varepsilon - 1)/\varepsilon$$

$$\delta C[\text{pF}] = 350\ \delta r_g[\text{cm}] + 60\ \delta\rho/\rho$$

Assuming $\delta r_g \sim 5\,\mu m$, $\delta\rho/\rho \sim 0.25$ %, we obtain $\delta C = 0.3$ pF. This induces a charge $Q_I = V_g\,\delta C = 26000$ pC between grid and collector. The charge is divided between them according to their supply impedance. The charge-sensitive amplifier has an effective impedance $R_c \sim 10^5\ \Omega$. The grid is a low-impedance voltage source, $R_g \sim 0.1\ \Omega$. The charge induced on the collector is then $Q_c \sim Q_I R_g/R_c = .026$ pC. This corresponds to about 10 % of a minimum-ionizing pulse height. The bulk of this charge is delivered during the expansion and compression strokes; only a small fraction of it should appear during the ionization drift time.

The microphonics problem requires careful quantitative study in the prototype development. Displacement effects could be minimized by located expansion plates symmetrically on opposite walls of the chamber. The collector and grid must both be designed to have no vibration modes in the .1 - 10 kHz region; this could be accomplished on the collector by locating damping material inside, and on the grid by making it of wire mesh rather than free-supported wires.

Cosmic Ray Background

The cosmic ray flux at sea-level is $r_c \sim 10^{-2}\ cm^{-2}s^{-1}ster^{-1}$. The total rate in each module is $R_c \sim r_c\ 4LR = 5\times10^3\ s^{-1}$. During the gate time (300 μs) for ionization calorimetry, ~2 cosmic rays traverse each module. During the bubble chamber

sensitive time (~20 msec), ~100 traversals occur. There should be little difficulty in either case.

Muon Identification

The liquid argon bubble chamber provides excellent discrimination between prompt muons and muons originating in π-μ decay.

Muon candidates are selected on the basis of

1) penetration through one or both steel toroids following the module containing a neutrino interaction; or

2) a minimum-ionizing track which is observed in the bubble chamber to not interact over a distance of several absorption lengths.

The probability that a pion not interact in a length z is $P_\pi = e^{-z/A}$. The probability that a pion of energy $\gamma m_\pi c^2$ decays to a muon within a length z is $P_{\pi-\mu} \sim z/\gamma c\tau_\pi$. Fig.18 shows $P_\pi(z)$, $P_{\pi\mu}(z,E_\mu)$. The π-μ decay background is thus $P_\mu = A/\gamma c\tau = 1.8\ \%/E_\mu[\text{GeV}]$. The elimination of π-μ decays after pion interactions allows a substantially lower π-μ contamination then in existing experiments using segmented calorimetry or external muon identification.

V^0 Identification

We can identify the decays $K_s^o \to \pi^+\pi^-$ and $\Lambda \to p\pi^-$ in the bubble chamber image of an event. The Jacobean peak ($\theta_{cm} = 90^o$) in each case corresponds to an opening angle (in radians) $\theta_o \sim 0.9/E_o$, where $E_o|\text{GeV}|$ is the energy of the parent hadron. We could identify a V^o if its opening angle is sufficient to resolve the two tracks within ~ one radiation length of the decay vertex: $\theta_{min} \sim 2$ mm/X = .012 rad, or $E_o^{max} = \theta_{min}/\theta_o \sim 75$ GeV.

We can improve V^0 identification in two ways. First, we can require the V^o to vertizice to the neutrino interaction point. Second, we can require rough agreement between θ_o and E_o in those cases where calorimetry of the V^o is distinct from the other interaction products. The laboratory opening angle decreases a factor of 2 only for $\theta_{cm} \lesssim 15^o$ (3 % of decays). The requirement $.45 < \theta E_o < .9$ GeV thus suppresses backgrounds without rejecting real decays.

C. Magnetized Iron Spectrometer

A toroidal magnetized iron spectrometer follows each liquid argon bubble chamber, as shown in Fig.1. It consists of two toroids, each 1 m thick × 7 m diameter, magnetized to partial saturation (B ~ 2 Tesla). A muon track is measured in the bubble chamber before and after the toroids, and in drift chambers located behind each toroid.

The deflection of a muon by the toroidal magnetic field is

$$\theta_B = 0.3\ B\ell/p = 1.2/p\ \text{[GeV]}$$

The principal error in measuring θ_B comes from multiple scattering θ_I in iron:

$$\theta_I = \frac{.015}{p}\sqrt{\ell/X_I} = 0.16/p\ \text{[GeV]}$$

The momentum resolution is $\delta p/p \sim \theta_I/\theta_B = 13\ \%$.

The drift chambers in the gaps between toroids allow momentum measurement of soft muons, and aid pattern recognition in multi-muon events.

Neutrino Beam

We anticipate using ARGONAUT to study neutrino processes in several neutrino beams:

1) N-30 dichromatic beam [4] - the event spectrum is shown in Fig.19 for charged- and neutral-current processes in ν_μ and $\bar{\nu}_\mu$ beams. Here we assume 500 GeV incident protons, and a 350 GeV/c tune. Fig.20 shows the energy-radius correlation produced by the decay kinematics in the momentum-selected meson beam.

2) ν_e beam [34] - the event spectrum is shown in Fig.21 for ν_e and $\bar{\nu}_e$ interactions. Both are present in equal number in the beam, since the ν_e source is K_L^o decay. ν_μ and $\bar{\nu}_\mu$ backgrounds contribute about 10 % of the events.

3) Dichromatic beam for Energy Doubler/Saver - Mori has calculated a neutrino spectrum for 1000 GeV incident protons, assuming a (hypothetical) 700 GeV tune of the N-30 dichromatic beam [4]. Fig.22 shows the corresponding event spectrum. Note that useful event rate extends beyond 700 GeV.

Physics Objectives

We envision using ARGONAUT to study a broad range of neutrino processes: 1) multi-lepton final states; 2) $\nu_\mu e \rightarrow \nu_\mu e$; 3) semi-leptonic scaling variable distributions; 4) search for new phenomena in neutrino interactions using 1000 GeV protons from the Energy Doubler/Saver. Table III presents event rates

for the various processes 1-3. Of particular interest is the expected rate of 1 event/day for $\nu_\mu N \rightarrow \mu^-\mu^+\mu^- X$, and 3 events/day for $\nu_\mu e \rightarrow \nu_\mu e$. A proper study of these rare processes requires the enormous mass (360 tons fiducial) of the ARGONAUT.

The total event rate is $\sim 2.5/10^{13}$p. Since each module functions largely independently, we can analyze several events per beam pulse on the average with no dead time losses.

Comments are presented below on the capabilities of ARGONAUT for studying each of the main physics objectives:

1) Multi-Lepton Final States - ARGONAUT provides excellent muon identification for muons down to energies of a few GeV. It should have near total acceptance for final state muons, and allow momentum measurement to ±13 %. Electron calorimetry is excellent, and angle measurement should have an accuracy ~1.5 mrad. We should thus be able to reconstruct the visible leptonic final state, and investigate the origin of the observed multi-lepton events. Associated V^o decays can be identified, and used to signal flavor cascade as an origin for some of these events.

Many mechanisms have been proposed to explain the origin of trimuon production in neutrino interactions. The mechanisms can be distinguished to some extent in their predictions of various kinematic distributions among the lepton momenta, as calculated by Albright[9]. Related processes should occur for some mechanisms: opposite sign trimuons ($\nu_\mu N \rightarrow \mu^-\mu^+\mu^+ X$), tetramuons, multi-leptons in $\bar{\nu}_\mu$ interactions, $\mu^-e^-e^+$, etc. ARGONAUT has the combination of target mass and measurement capability to refine and extend the study of these processes.

2) $\nu_\mu e \to \nu_\mu e$ - Neutrino-electron scattering provides an opportunity to study in pure form the structure of the weak neutral current. Sehgal has shown[35] that the elastic cross-sections must obey several general constraints:

$$\sigma(\bar{\nu}_\mu e) < 3\sigma(\nu_\mu e) \qquad \sigma(\nu_e e) < 3\sigma(\bar{\nu}_e e)$$

$$\sigma(\nu_e e) - \sigma(\nu_\mu e) = 3\left[\sigma(\bar{\nu}_e e) - \sigma(\bar{\nu}_\mu e)\right]$$

ARGONAUT provides excellent electron calorimetry and angular measurementfor studying these processes. The bubble chamber image allows strong rejection of beckground processes such as $\nu N \to \nu N \pi^0$, $\nu_e n \to p e^-$ by observation of the recoil nucleon. Additional kinematic separation, as discussed by Walker[36], should further reduce background to a small fraction of expected signal rate.

3) Scaling Variable Distributions- ARGONAUT measures $E_H, \theta_H, \vec{p}_\mu (\vec{p}_e)$. We know E_ν approximately from the energy/radius correlation in the dichromatic beam. These quantities allow us to calculate $q^2 = 4E_\nu E_\mu \sin^2\theta_\mu/2$, $x = q^2/2m_p E_H$, $y = E_H/E_\nu$. Asymptotic freedom requires a sizable gluon contribution to neutrino scattering for $E_\nu > 100$ GeV.[7] The size of this contribution and its q^2 dependence are of strong interest in QCD. The q^2 and x distributions are sensitive to the abundance of sea quarks, and to their masses; in this respect we obtain a picture of the well-dressed hadron.

The y distribution is sensitive (through E_H) to the production of new heavy flavors (high y anomaly[6]), and to admixtures of left- and right-handed currents which would cross the pure forms $d\sigma/dy = 1$ for ν, $(1-y^2)$ for $\bar{\nu}$.

Figure 23 shows the kinematic correlations amongst $x, y, E_\mu, \theta_\mu, E_H, \theta_H$ for 250 GeV neutrino interactions. ARGONAUT provides two important features which allow thorough study of scaling variable distributions. First, it has large, flat acceptance for the range $.1 < x < .9$, $.05 < y < .95$. Second, the resolution on x and y is everywhere good, ≤15%.

Experimental Program

We envisage a three-step program to build ARGONAUT:

1) Prototype Tests - Design development and prototype tests are necessary for five aspects of the detector: a) operating characteristics of liquid argon in a bubble chamber; b) cryostat design; c) expansion system; d) CCD camera and imaging system; e) long-drift ionization calorimetry. In each case we would require substantial Laboratory support. Specific plans will be developed with the Neutrino and Physics Departments. Some aspects of these developments could be carried out by university-based collaborators.

2) Construct One Module - We propose to construct one complete module, as an experiment. The module could be installed in one of the existing buildings in the neutrino area, and used for experiments with the new dichromatic beam. In this way we would gain operating experience with the detector, and refine its design for the full ARGONAUT.

A cost estimate is presented in Table IV for the single module. It includes all components of the liquid argon bubble chamber/calorimeter, but not the toroids or building.

3) ARGONAUT - The full ARGONAUT detector would be built as a facility. It could serve many experimenters, just as does the 15' bubble chamber. The full detector would be the primary focus of the neutrino program with the Energy Doubler/Saver, exploring neutrino interactions up to $E_\nu \sim 700$ GeV.

A cost estimate for the full detector is presented in Table IV. It includes toroid spectrometers and the buildings for the detector and for the support equipment.

During recent monthswe have analyzed the conceptual design of ARGONAUT in the detail presented in this proposal. We are now beginning to solicit a strong collaboration, in which to perform the prototype tests and build the first module. There is a possible interest in some aspects of the prototype development at other laboratories (SLAC, CERN). We will inform the Laboratory as the collaboration develops.

Conclusion

ARGONAUT provides a unique combination of information about neutrino interactions. The bubble chamber image is valuable for isolating rare processes from backgrounds, and for identifying muons and strange particle decays. The calorimetry allows accurate measurement of E_H, E_e. The independent modular structure accomodates several interactions per beam pulse.

The detector design embodies several technological innovations: liquid argon as a bubble chamber fluid; electronic recording of bubble images on videotape; ionization drift over one meter distance; a new approach to expansion bellows and cryostat design.

We believe that the detector described here improves in many respects the information available from existing and planned detectors. With it we can advance into the frontiers of neutrino physics - the detailed study of rare leptonic processes, and the exploration of the new energy realm of the Energy Doubler/Saver.

ACKNOWLEDGMENTS

We gratefully acknowledge helpful conversations with J. Ballam, R.M. Barnett, D. Freytag and B. Richter (SLAC), D. Boyce (Univ. of Chicago), R.R. Huson and S. Mori (Fermilab), H. Georgi and S. Glashow (Harvard), L. Jones (Univ. of Michigan), and U. Camerini and J. Fry (Univ. of Wisconsin). We thank B. Perington and R. Donaldson for valuable help in preparing the manuscript, and E. Luisada, R. Sidwell and K. Skraboly for drafting assistance.

REFERENCES

1. M. Holder et al., Phys. Letters 73B, 105 (1978). B. C. Barish et al., Phys. Rev. Letters 38, 577 (1977). M. Holder et al., Phys. Letters 70B, 393 (1977). A Benvenuti et al., Phys. Rev. Letters 38, 1110 (1977). A. Benvenuti et al., Phys. Rev. Letters 38, 1183 (1977). A. Benvenuti et al., Phys. Rev. Letters 40, 488 (1978). A. E. Asratyan et al., Proceedings of the International Neutrino Conference, Aachen (1976).
2. J. Blietschau et al., Phys. Letters 60B, 207 (1976). J. Von Krogh et al., Phys. Rev. Letters 36, 710 (1976). P. Bosetti et al., Phys. Rev. Lett. 38, 1248 (1977). C. Baltay et al., Phys. Rev. Lett. 39, 62 (1977). H. Ballagh et al., Phys. Rev. Lett. 39, 1650 (1977). P. Bosetti et al., Phys. Rev. Letters 73B, 380 (1978). R. J. Loveless et al., submitted to Phys. Rev. Letters. H. Wachsmuth, Varenna School on Weak Interactions (1977). V.Z. Peterson, Neutrino Conference, Elbros, Caucasus (1977). D. C. Cundy, International Neutrino Conference, Budapest (1977). K. Schultze, Hamburg Conference, International Symposium on Lepton and Photon Interactions, Hamburg (1977).
3. A. Benvenuti et al., Nucl. Instrum. Methods 125, 447 (1975); Nucl. Instrum. Methods 125, 457 (1975).
4. D. Edwards, S. Mori, S. Pruss, 350 GeV/c Dichromatic Neutrino Target Train. Fermilab Report TM-661 (1976) and S. Mori, private communication.
5. See for instance, A. de Rújula, "Quark-Tasting with Neutrinos", Proc. of 1976 Coral Gables Conference (1976).

6. B. Aubert et al., Phys. Rev. Letters 33, 984 (1974), A. Benvenuti et al., Phys. Rev. Letters 36, 1476 (1976), M. Holder et al., Phys. Rev. Letters 38, 433 (1977), T. Y. Ling et al., "Criticism of Recent Data on the y Distributions of Neutrinos and Antineutrino Scattering". International Symposium on Lepton and Photon Interactions at High Energies (1977).

7. H. Georgi and H. D. Politzer, Phys. Rev. Letters 36, 1281 (1976). R. M. Barnett, H. Georgi and H. D. Politzer, Phys. Rev. Letters 37, 1313 (1976).

8. A. Pais and S. Treiman, Phys. Rev. Letters 35, 1206 (1975). P. H. Cox and A. Yildiz, Phys. Rev. D16, 2897 (1977).

9. J. M. Losecco, "Higgs Boson Production in Neutrino Scattering", unpublished (1976). C. H. Albright, J. Smith and J. A. M. Vermaseren, "A Comparison of Trimuon Production Mechanisms". Fermilab Report 78/14 THY (1978).

10. C. Rubbia, "The Liquid-Argon Time Projection Chamber: A New Concept for Neutrino Detectors", CERN EP Internal Report 77/8 (1977).

11. S. J. Barish et al., Phys. Rev. Letters 33, 448 (1974).

12. R. P. Shutt, Bubble and Spark Chambers, Vol. I, Academic Press, New York, London (1967).

13. S. Wolff, Dissertation, "Blasenbildung und Blasenwachstum in einer mit Wasserstoff und Deuterium gefullten Blasenkammer", Hamburg, (1969) unpublished.

14. H. Loosli and H. Oeschger, Earth and Planetary Science Lett. 5, 191

(1968); Earth and Planetary Science Lett. 7, 67 (1969) H. Loosli, H. Oeschger and W. Wiest, J. Geophys. Res. 75, 2895 (1970).

15. For comparison with tritium contamination in D_2, see G. Horlitz et al., "Bubble Creation by Electrons from Tritium Decay in a Hydrogen Bubble Chamber", DESY 73/31 (1973).

16. O. Manuel, private communication (1978).

17. R. Huson, ed. 15-ft. Bubble Chamber Safety Report. Vol. 2, pp. 1-53. Fermilab (1972).

18. F. Villa and L. C. Wang, "Recording Streamer Chamber Tracks with Charge Coupled Devices", SLAC PUB 1890 (1977).

19. Fairchild CCD 211 and related models.

20. E. M. Rowe and J. H. Weaver, "The Uses of Synchrotron Radiation", Scientific American, p. 32, June 1977.

21. M. Bougon, "Investigation of Dark Field Scotchlite", Proc. of Int. Conf. on Bubble Chamber Tech., Heidelberg (1967).

22. D. Freytag, "Tests of Linear Image Sensors for Detection of Tracks in a Bubble Chamber", SLAC Group BC, Internal Report (1976).

23. Ampex FR-1900.

24. W. J. Willis and V. Radeka, Nucl. Instrum. Methods 120, 221 (1974). C. W. Fabjan et al., Nucl. Instrum. Methods 141, 61 (1977). T. A. Gabriel and W. Schmidt, Nucl. Instrum Methods 134, 271 (1976).

25. D. W. Swan, Proc. Phys. Soc. 83, 659 (1964).

26. L. S. Miller, S. Howe, and W. E. Spear, Phys. Rev. 166, 871 (1968).

27. D. W. Swan, Proc. Phys. Soc. 82, 74 (1963). W. Hoffman et al., Nucl. Instrum. Methods 135, 151 (1976).

28. A similar amplifier configuration is used for Ge-Li solid state detectors. There the input FET is located in the LN_2 vessel containing the detector. It is amusing to note that our bubble chamber operating temperature T~120 K is the minimum-noise temperature for FET's.

29. U. Fano, Phys.Rev. 72, 26 (1947).

30. T. Doke et al., Nucl.Instr.and Methods 134, 353 (1976).

31. E. Segre, ed. Experimental Nuclear Physics p 267. John Wiley & Sons. New York (1953). H.A. Kramers, Physica 18,665 (192).

32. A. van Ginneken, "AEGIS - A Program to Calculate the Average Behavior of EM Showers", Fermilab report FN-309 (1978).

33. A. van Ginneken, "CASIM, Program to Simulate Hadronic Cascades in Bulk Matter". Fermilab report FN-272 (1975).

34. S. Mori, "Improved Electron Neutrino Beam". Fermilab report TM-769 (1978).

35. L.M. Sehgal, Phys. Lett. 48B, 60 (1974).

36. P. Berge et. al., "Proposal for a new Neutrino Detector at Fermilab", Fermilab Proposal (1977).

Table I.

		$_2He^4$	$_1H^1$	$_1D^2$
Triple point	T[K],p[bar]	- -	14.0 0.07	18.7 0.17
Normal boiling point	T[K]	4.2	20.4	23.6
Critical point	T[K],p[bar]	5.2 2.3	33.2 13.0	38.4 16.7
Bubble chamber operation:				
Temp., pressure	T[K],p[bar]	3.2 0.4	26 4.0	30 4.5
Liquid density	ρ[g/cm^3]	0.14 (0.12)	0.06 (0.07)	0.14 (0.17)
Pressure drop (vapor to operation)	Δp[bar]	0.28	2.5	2.8
Expansion ratio	$\Delta V/V$[%]	0.75	0.7	0.6
Isentropic compressibility	β[bar^{-1}]x10^3	-	1.97	1.06
Sound velocity	S [m/s]	215 (180)	923 (1040)	778 (-)
Expansion cycle time	τ [ms]	-	~ 90	~ 90
Heat of vaporization	H [J/g]	23.6 (20.9)	390 (440)	260 (304)
Thermal conductivity	k [mW/K m]	22.4 (27.1)	132 (119)	147 (134)
Specific heat	C_p[J/g·K]	2.7 (4.5)	13.2 (9.8)	9.2 (6.2)
Surface tension	σ [mN/m]	0.19 (0.10)	1.0 (2.9)	1.9 (3.2)
Viscosity	η [mP]	0.037 (0.036)	0.09 (0.13)	0.18 (0.29)
Index of refraction	n	1.025 (-)	1.10 (-)	1.10 (-)
Dielectric constant		1.05	1.20	-
Radius of critical bubble	r [Å]	83	100	150
Absorption length	A [cm]	- (-)	887 (760)	403 (332
Radiation length	X [cm]	1027 (1200)	~ 1000 (860)	~ 900 (740)

Note: values in brackets are for normal boiling point.

$_{10}Ne^{20}$	$_{18}Ar^{40}$	$_{54}Xe^{131}$	C_3H_8 44	CF_3Br 148
24.5 0.4	83.8 0.7	161.4 0.8	85.9 -	105.2 -
..1	87.3	165.0	231.1	215.4
44.4 26.5	150.8 48.9	289.7 58.4	370.0 44.0	340.2 39.6
36 7.8	~120 ~12	252 26	333 22	303 18
1.02 (1.21)	~ 1.16 (1.39)	2.3 (3.04)	0.43 (0.58)	1.50 (8.71)
$\gtrsim$ 5	~ 9	-	~ 12	~ 10
0.5	~1.0	~ 2.5 est.	~ 3	~ 3
0.6	0.27	-	1.03	-
~ 400 (_)	584 (875)	- (650)	470 (970)	- (_)
150	100 - 200	-	~ 200	~ 200
67 (86)	- (163)	- (96)	255 (426)	- (119)
95 (114)	81 (121)	- (73)	100 (119)	- (59)
2.4 (1.9)	- (~1.0)	- (~0.3)	3.1 (2.2)	0.91 ( )
> 1.5 extr. (4.8)	4.97 (12.5)	3.96 (18.46)	3.08 (15.5)	- (4)
0.6 (1.25)	1.16 (2.57)	- (5.07)	0.65 (2.00)	- (2.12)
1.10 (-)	- (1.23)	1.18 (-)	1.25 (-)	1.24 (-)
1.16	1.41	-	-	-
-	-	-	70	63
89 (75)	97 (81)	- (-)	176 (130)	73 (13)
27 (24)	17 (14.3)	3.9 (3.0)	110 (82)	11 (2)

References for Table I.

1. R. P. Shutt, Bubble and Spark Chambers, Vol. I, Academic Press, New York, London (1967).

2. S. Wolff, Dissertation, "Blasenbildung und Blasenwachstum in einer mit Wasserstoff und Deuterium gefullten Blasenkammer", Hamburg, (1969) unpublished.

3. V. P. Kenney, W. D. Shephard, W. B. Madden, E. A. Harrington, "Design Considerations for the use of Neon-Hydrogen Mixtures in the 12' Hydrogen Bubble Chamber", Argonne National Laboratory, ANL-BBC 92, June (1967 unpublished.

4. G. G. Harigel, "Operating Conditions for Big Bubble Chambers (15' Chamber) Filled with Neon/Hydrogen Mixtures", National Accelerator Laboratory, TM-532, 2600.0, June (1974) unpublished.

5. Selected Cryogenic Data Notebook, BNL 10200 (1966).

6. Comprehensive Inorganic Chemistry, Pergamon Press, Oxford, New York, Toronto, Sydney, Braunschweig (1973), p. 164-165.

7. Cryogenic Data, Cryenco, Denver Colorado.

8. G. Harigel, "Numerical Calculations of Recompression Time of Bubbles in Helium Bubble Chambers", Internal Note/BEBC/OP-17, May (1970) unpublished.

9. G. Harigel, J. Riche, G. Horlitz, S. Wolff, Numerical Calculations of the Recompression Time of Bubbles in Liquid Hydrogen Bubble Chambers, April (1968) unpublished.

10. G. Harigel, J. Riche, "Numerical Calculations of Recompression Times of Bubbles in Liquid Deuterium Bubble Chambers", Internal Note BEBC/OP-13, May (1970) unpublished.

11. F. Din, Thermodynamic Functions of Gases, Vol. 2, The British Oxygen Company, Limited Research and Development Centre, London, Butterworths (1962) p. 146-199, F. Din: "Argon".

12. F. Din, Thermodynamic Functions of Gases, Vol. 2, The British Oxygen Company, Limited Research and Development Centre, London, Butterworths (1962) p. 115-145, N. R. Kuloor, D. M. Newitt, J. S. Bateman: "Propane".

13. A. M. Clark, F. Din, J. Robb, A. Michels, T. Wassenaar, and Th. Zwietering, Physica XVII, no. 10, 876 (1951).

14. K. Goldman and N. G. Scrase, Physica 45, 1 (1969).

15. M. J. Terry, J. T. Lynch, M. Bunclark, K. R. Mansell and L. A. K. Staveley, J. Chem. Thermodynamics 1, 413 (1969).

16. A. Michels, J. M. Levelt and W. De Graaff, Physica XXIV, 659 (1958).

17. Equilibrium concentration N-Ar mixtures (gas and liquid, mole percent up to 103 K), NBC Report AD 272769, December (1969) p. 1604.9.

18. Velocity of sound in Liquid Argon, NBC Report AD 272769, December (1969).

19. C. C. Lim and R. A. Aziz, Can. J. Phys. 45, 1275 (1967).

20. W. Van Dael, A. Van Itterbeek, A. Cops and J. Thoen, Physica 32, 611 (1966).

21. A. A. Vasserman and V. A. Rabinovich, IFZh [Journal of Engineering Physics], 13 No. 2, 106 (1967).

22. B. J. Bailey and K. Kellner, Physica 39 , 444 (1968) and Brit. J. Applied Physics 18, 1645 (1967).

23. F. B. Sprow and J. M. Prausnitz, Trans. Faraday Soc. 63, 1097 (1966).

24. N. F. Zhdanova, Sov. Phys. JETP 4, No. 5, 749 (1957).

25. N. S. Rudenko, J. Techn. Phys. (USSR), 18, 1123 (1948).

26. L. Bewilogua, A. Handstein, and H. Hoeger, Cryogenics 6, 21 (1966).

27. P. Kunkel, "Erzeugung und Wachsen von Blasen im Arbeitsbereich einer Druckstabilisierten Propan-Blasenkammer", Dissertation, Würzburg (1967) unpublished.

28. G. Christenn, "Die Stoffkonstanten der Blasenkammerflüssigkeit Propan und ihre Wiedergabe durch Analytische Approximation", Diplomarbeit, Wuerzburg (1969), unpublished.

29. DuPont, "Freon" Technical Bulletin B-2 (1957).

30. DuPont, "Kinetic" Technical Bulletin B-4 (1954).

31. DuPont, "Thermodynamic Equations for 'Freon-13B1'", D-8 (1953).

32. Proc. Intern. Conf. Bubble Chamber Technology, ed., M. Derrick, Argonne National Laboratory, ANL (1970), p.543 R.W. Newport, "The Refractive Indices of Neon and Neon Hydrogen Mixtures".

33. G. Horlitz, S. Wolff, G. Harigel, DESY 68/43 (1968)

34. Proc. Intern. Conf. Bubble Chamber Technology, ed., M. Derrick, Argonne National Laboratory, ANL (1970), p.424, G. Harigel, G. Horlitz, S. Wolff, "The Influence of Parasitic Boiling and Expansion Speed on the Dynamic Pressure in a Bubble Chamber".

35. Proc. Intern. Conf. Instrum. for High-Energy Physics, LBL (1960), p. 110.

36. D. Güsewell, F. Schmeissner, J. Schmid, Cryogenics 11, 311 (1971)

37. Th.G. Trippe et al., Rev.Mod.Physics 48, S50 (1976).

38. Proc. 1966 Intern.Conf.Instrum. : High Energy Physics, ed., D.M. Ritson, Stanford, M. Derrick, "Bubble Chambers 1964-1966".

39. Preliminary Data Sheet: Fairchild Charge Coupled Device CCD211, March (1976).

40. W.B. Street, J. Chem.Phys. 46, 3282 (1967)

41. Proc. 1966 Intern. Conf. Instrum. for High Energy Physics, ed., D.M. Ritson, Stanford, M.M. Block, I.R. Kenyon, J. Keren, D. Koetke, P. Malhotra, R.J. Walker, H. Winzeler, p.134, "The Northwestern University 50-cm Liquid-Helium Bubble Chamber".

Table II. Electron Drift Properties in Liquid Argon

density	ρ	1.16	g/cm^3
radiation length	X	17.	cm
absorption length	A	97.	cm
ionization loss	dE/dx	1.75	MeV/cm
critical energy	E_o	30.	MeV
Fano factor		0.11	
electron-ion energy	W	24.	eV
electron mobility	μ_o	475.	$cm^2 s^{-1} V^{-1}$
electron diffusion	D	28.	$\mu m/mm^{\frac{1}{2}}$
O_2 - electron attachment coefficient	$\lambda p/E$	0.14	$cm^2 \cdot ppm/KV$

Table III

Event Rates

Beam	Event Type	Events/(Day Module) E < 150 GeV	E>150 GeV	Total
N-30 (ν)	ν_μ charged current	400	320	720
"	ν_μ neutral current	140	110	250
"	ν_μ wide-band background	1.8	.04	1.8
"	$\bar{\nu}_\mu$ background	.05		.0
				970
N-30 ($\bar{\nu}$)	$\bar{\nu}_\mu$ charged current	43	7.4	50
"	$\bar{\nu}_\mu$ neutral current	16	2.8	
"	$\bar{\nu}_\mu$ wide-band background	0.2	.001	0.2
"	ν_μ background	0.2		0.2
				70
ν_e Beam	ν_e charged current			22
	ν_e neutral current			6.4
	$\bar{\nu}_e$ charged current			10
	$\bar{\nu}_e$ neutral current			4
	$\nu_\mu, \bar{\nu}_\mu$ neutral current background			3.3
				46
		E<350	E>350	
N-30 (ν)				
ED/S	ν_μ charged current	102	134	236
	ν_μ neutral current	29	39	
				304
N-30 ($\bar{\nu}$)	ν_μ charged current	7.4	2.6	10
ED/S	ν_μ neutral current	3.0	1.0	4
				14

Rare Processes

Beam	Event Type	Events/(Day Module)
N-30	$\nu_\mu N \rightarrow \mu^- \mu^+ X$	7.
	$\nu_\mu N \rightarrow \mu^- \mu^+ \mu^- X$	.07
	$\nu_\mu e \rightarrow \nu_\mu e$	.3

Table IV. COST ESTIMATES

(in 1000 $)

	1 Module	10 Modules
Pressure vessel		
Stainless steel (20 to/module)	60	600
Port structures	10	100
Fill with liquid argon (60 to/module)	12	120
Refrigeration		
Coldbox	40	200
Liquid nitrogen compressor	60	300
Argon purifier	10	20
Storage dewar for argon	30	90
Valves, cryo-loop, transfer lines	10	100
Vacuum pump	12	120
Vacuum piping	20	200
Expansion system		
Cold gas expansion valve	100	1000
Expansion membrane	10	100
Optics		
Fisheye windows	250	1250
Wide-angle lens	40	250
Film camera	10	(100)
CCD's (1 camera only for 1st module)	40	1000
Video tape	70	700
Scotchlite	5	50
Flash & power supply	12	120
Electronics		
Timing and synchronization	5	50
500 kV power supply for calorimter	100	500
CCD channels, digitizers	40	400
Drift chambers	40	400
Consultants	30	-
Toroids	-	3000
Buildings	-	2000
Total	996	12670

List of Figures

1. Cross-section of one detector module.
2. Artist's conception of complete detector.
3. Ratio A/X of hadron absorption length to electron radiation length vs. intrinsic angular resolution, for various materials.
   ● = electron angular resolution,
   □ = hadron angular resolution.
4. Vapor pressure (curve a) and vapor density (curve b) vs. temperature for liquid argon.
5. Detail of pressure vessel/cryostat construction.
6. Expansion system.
7. Optics and flash tube arrangement.
8. Chamber cross section showing limits for depth of field and intersection of angular acceptance for adjacent cameras.
9. Geometrical scattering function for liquid argon.
10. Video tape recording system for bubble-chamber images.
11. Ionization calorimetry arrangement.
12. Electron drift velocity (v) and column recombination (η_α) as a function of applied field.
13. Collected charge fraction and collection time as a function of radius. An oxygen concentration of 1 ppb is assumed.
14. Electron shower distribution in liquid argon.
15. Average hadron shower distribution in liquid argon: a) 10 GeV, b) 100 GeV. Containment contours are shown as fraction of total hadron energy in collected ionization.

16. Hadron energy response. Monte Carlo calculations at four energies indicated show linear response (±3%).

17. a) Hadron shower containment vs. angle θ_H.

    b) Fiducial length for complete shower containment vs. angle θ_H.

18. Background π-μ decay probability in liquid argon

19. Event spectrum using the N-30 beam, 500-GeV incident protons and a 300-GeV tune: a) neutrino interactions; b) antineutrino interactions.

20. Energy-radius correlation for neutrinos in the N-30 beam (500-GeV protons).

21. Event spectra for ν_e beam: a) ν_e interactions; b) $\bar{\nu}_e$ interactions.

22. Event spectra for neutrinos and antineutrinos using the N-30 beam, 1000-GeV incident protons and a hypothetical 700-GeV tune.

23. Kinematic correlations for 250 GeV neutrino scattering:

    a) ($E\mu$, $\theta\,\mu$, x, y); b) (E_H, θ_H, x, y).

24. Bubble chamber events in BEBC with zero magnetic field. The chamber is filled with a Ne-H_2 mixture: X=41cm, A=140 cm.

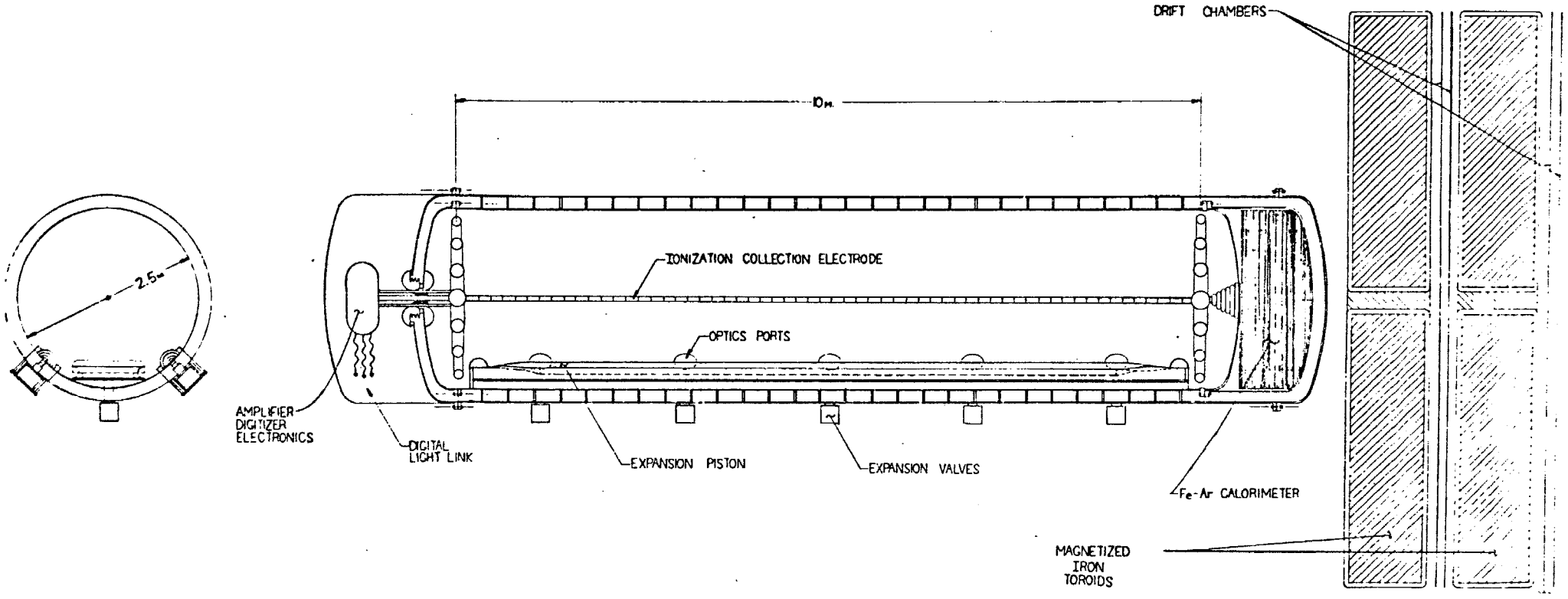
2.5m
10m
DRIFT CHAMBERS
IONIZATION COLLECTION ELECTRODE
OPTICS PORTS
AMPLIFIER
DIGITIZER
ELECTRONICS
DIGITAL
LIGHT LINK
EXPANSION PISTON
EXPANSION VALVES
Fe-Ar CALORIMETER
MAGNETIZED
IRON
TOROIDS

Figure 1a

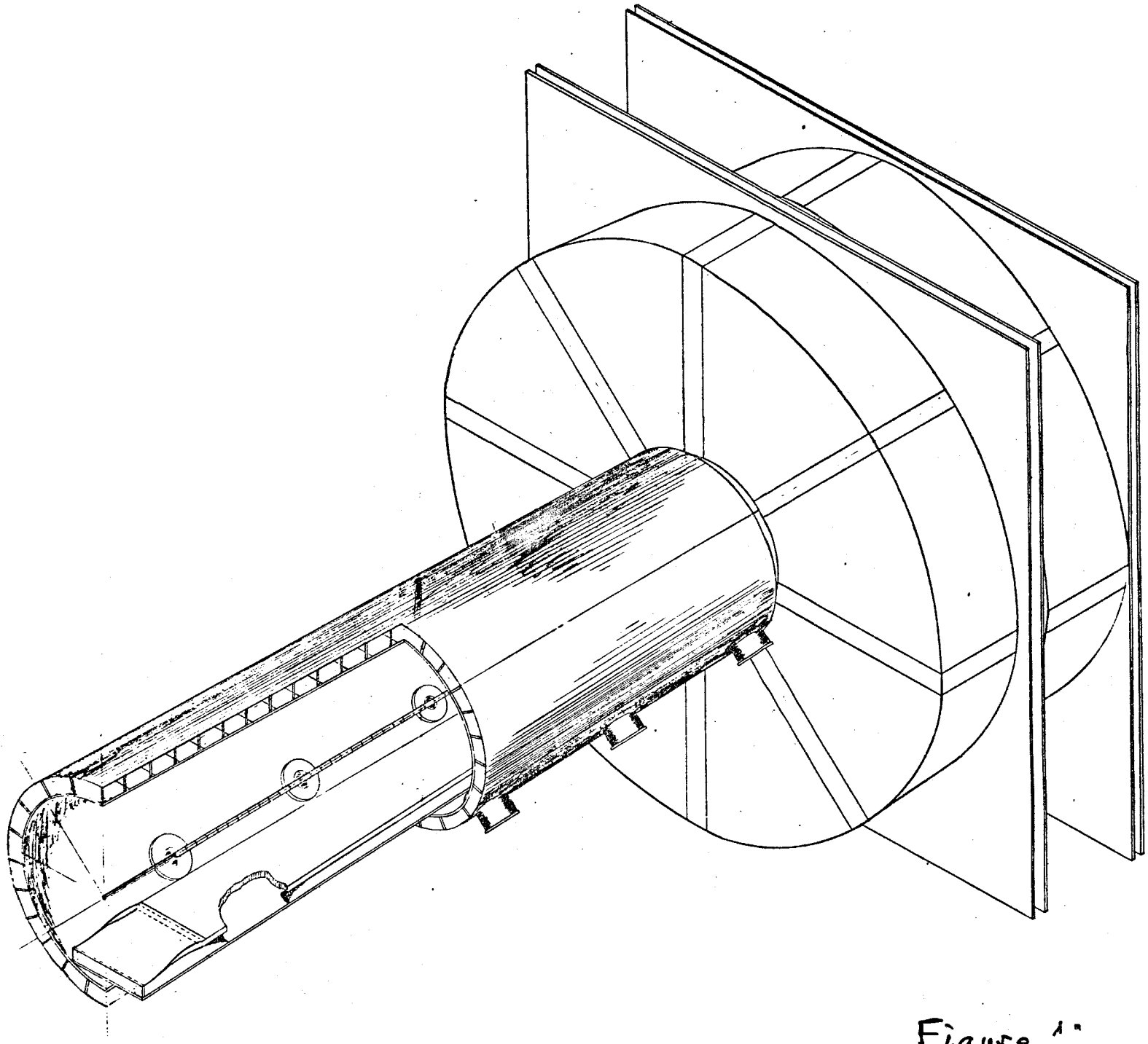

Figure 1

Figur 7.

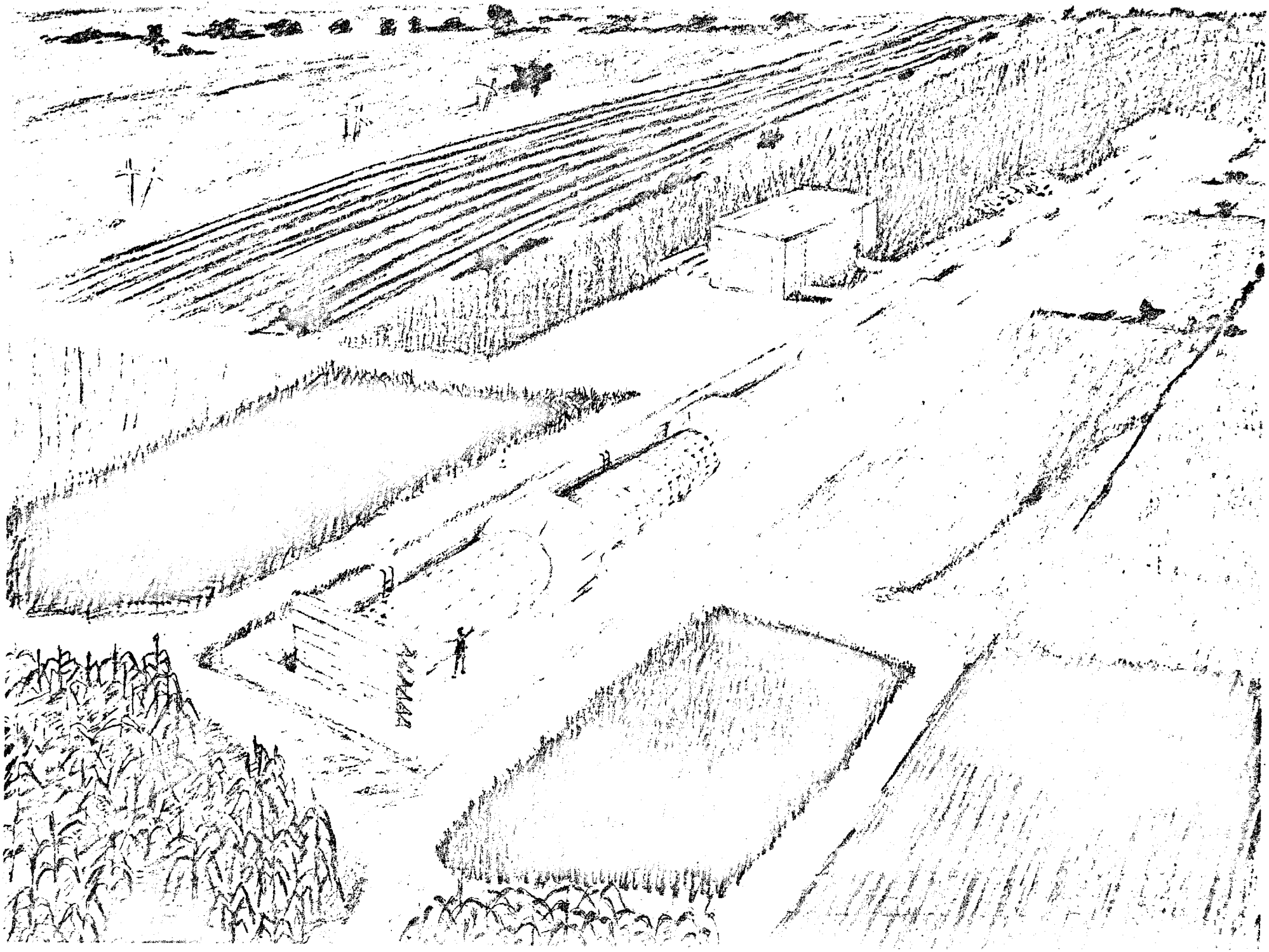

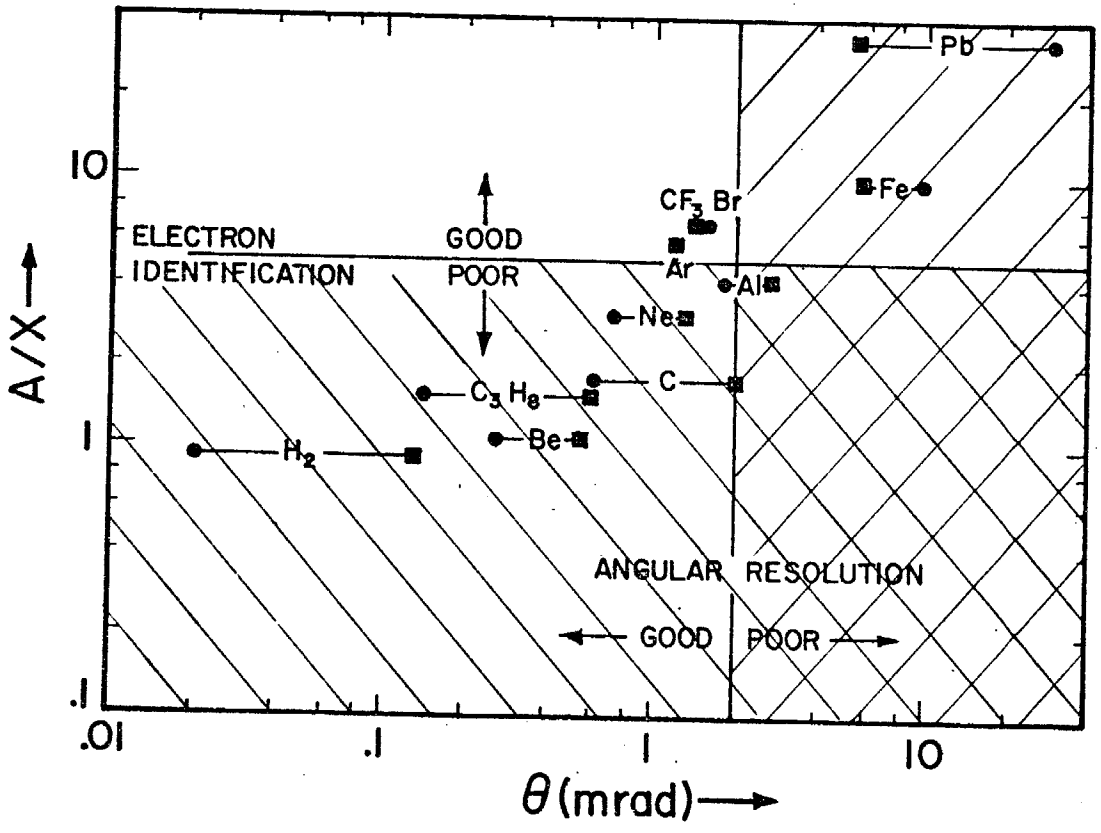
Pb
Fe
CF_3Br
Ar
Al
Ne
C
C_3H_8
Be
H_2
ELECTRON IDENTIFICATION
GOOD
POOR
ANGULAR RESOLUTION
GOOD
POOR
A/X
10
1
.1
.01
.1
1
10
θ (mrad)

Figure

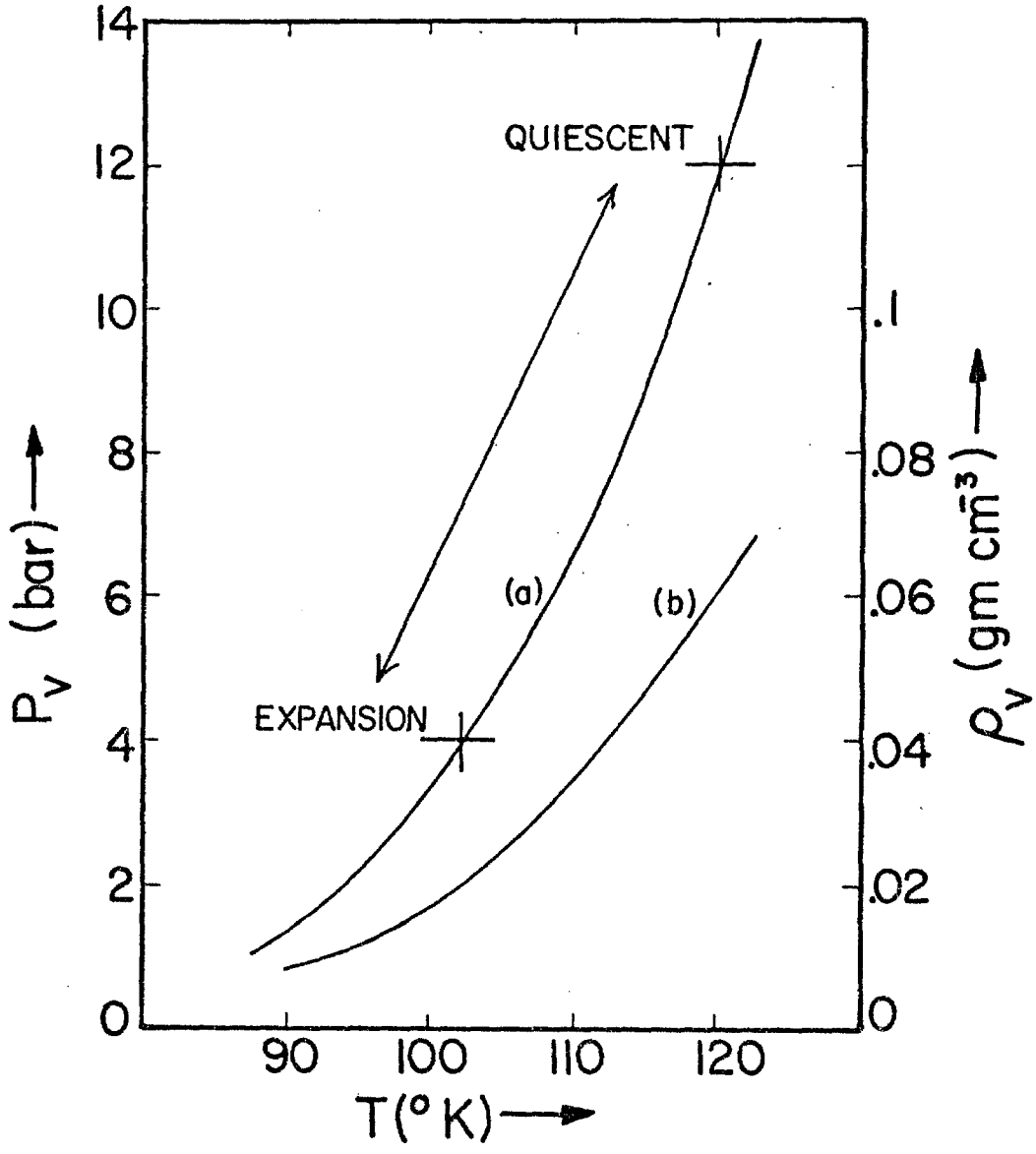
14
12
10
8
6
4
2
0
.1
.08
.06
.04
.02
0
90
100
110
120
QUIESCENT
EXPANSION
(a)
(b)
P_v (bar)
ρ_v (gm cm^{-3})
T(°K)

Figure 4

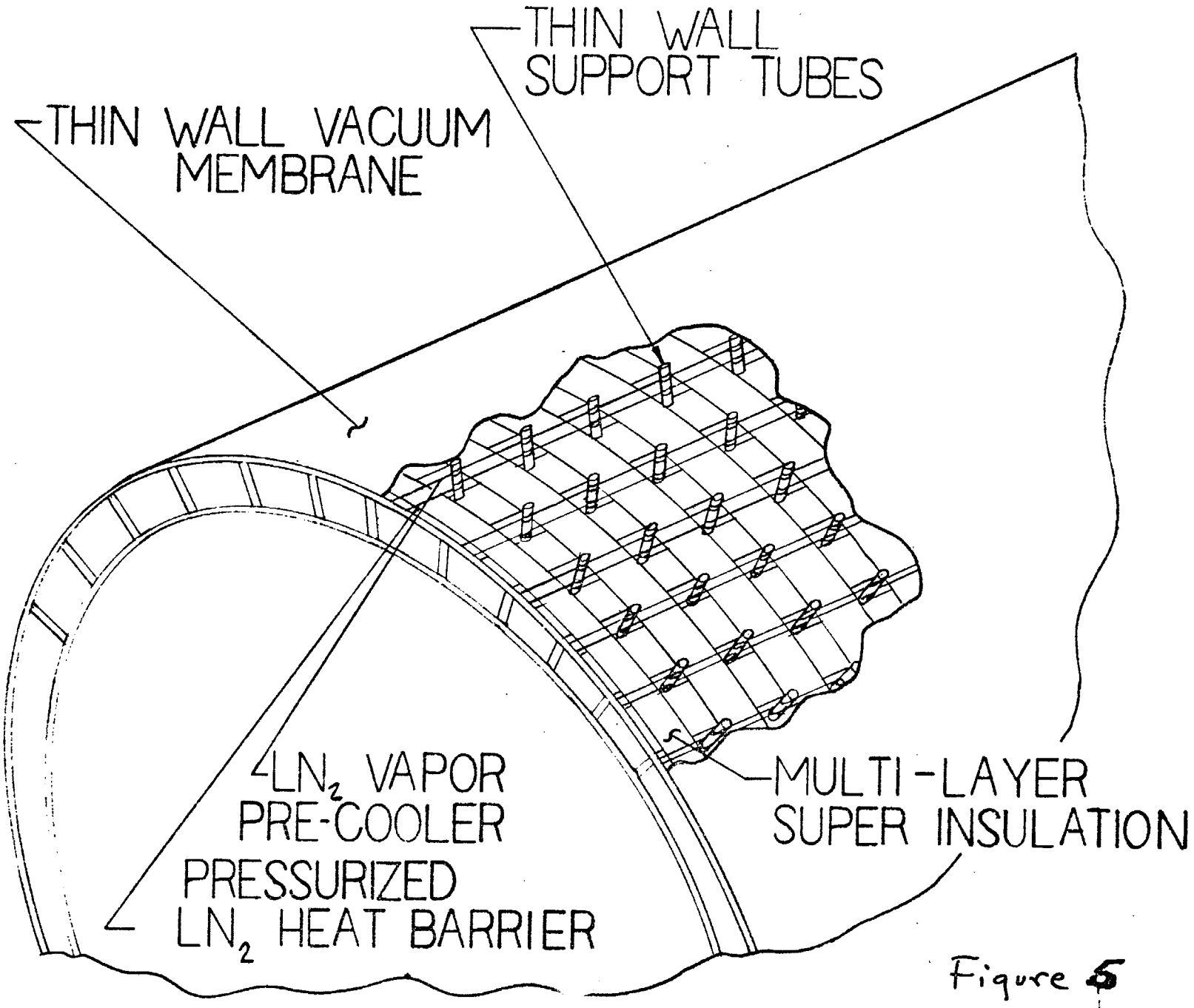
THIN WALL
SUPPORT TUBES
THIN WALL VACUUM
MEMBRANE
LN_2 VAPOR
PRE-COOLER
PRESSURIZED
LN_2 HEAT BARRIER
MULTI-LAYER
SUPER INSULATION

Figure 5

Figure 6

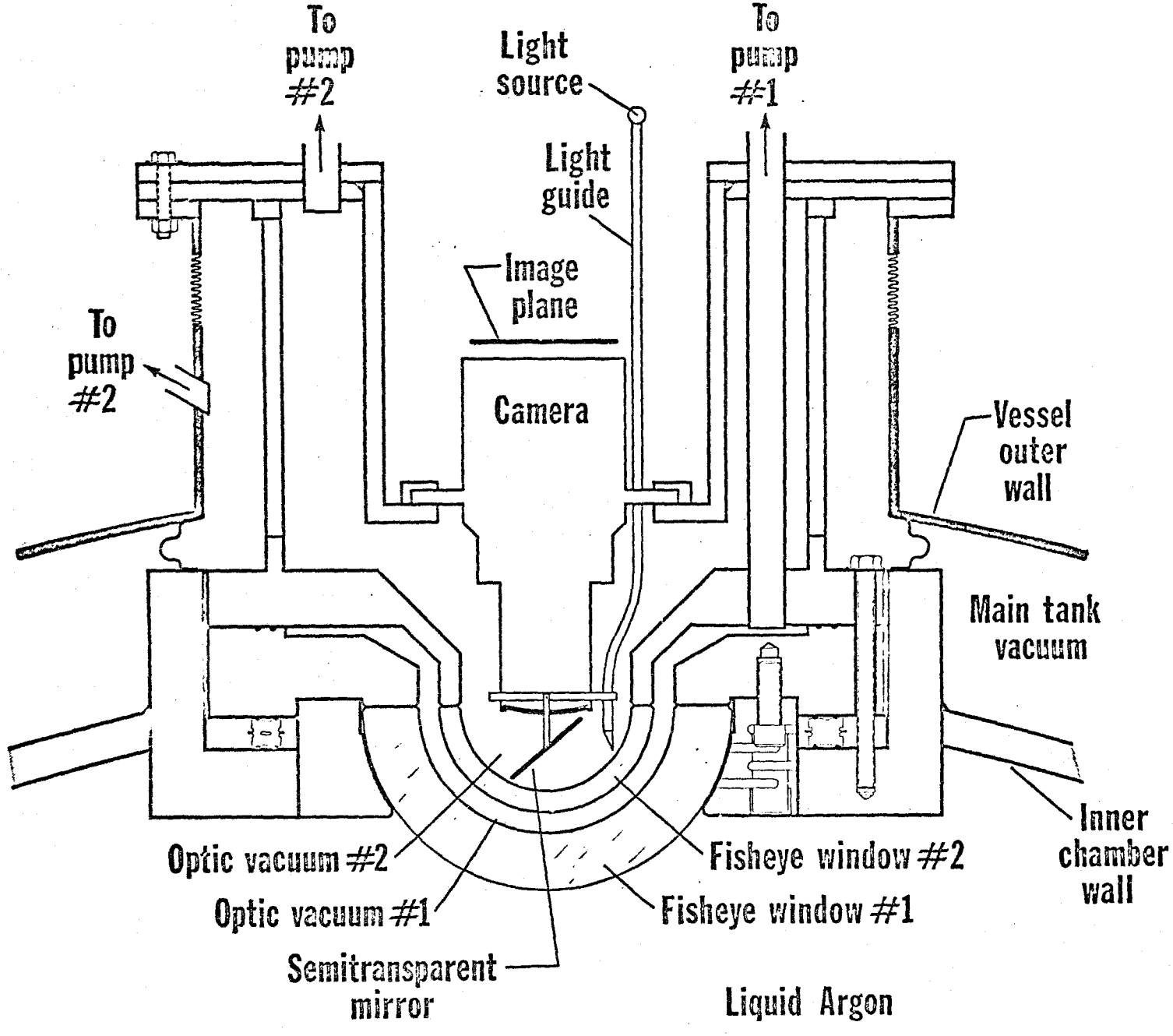
To pump #2
Light source
To pump #1
Light guide
Image plane
To pump #2
Camera
Vessel outer wall
Main tank vacuum
Optic vacuum #2
Optic vacuum #1
Semitransparent mirror
Fisheye window #2
Fisheye window #1
Liquid Argon
Inner chamber wall

Fig. 7

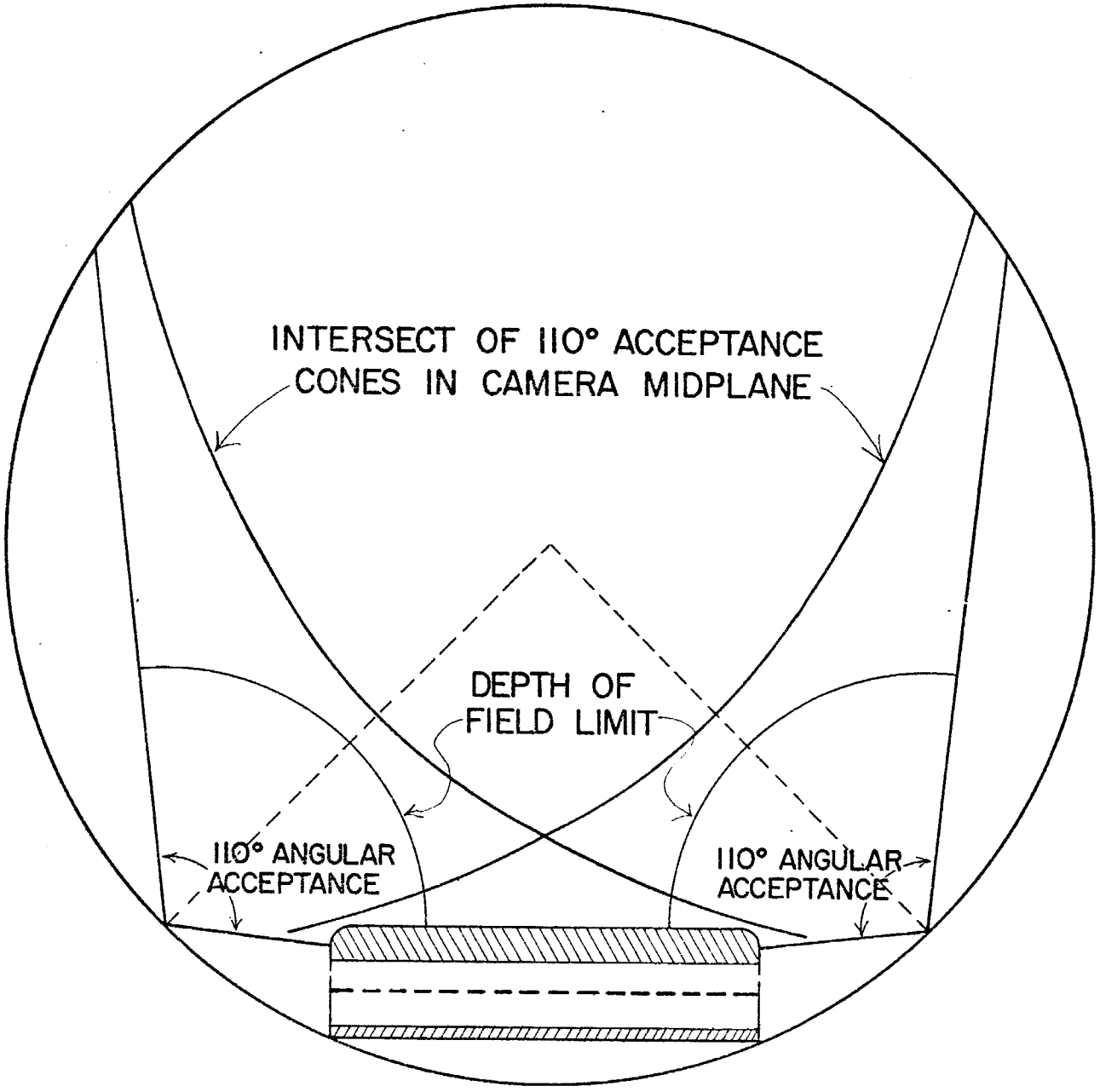
INTERSECT OF 110° ACCEPTANCE
CONES IN CAMERA MIDPLANE
DEPTH OF
FIELD LIMIT
110° ANGULAR
ACCEPTANCE
110° ANGULAR
ACCEPTANCE

Figure 8

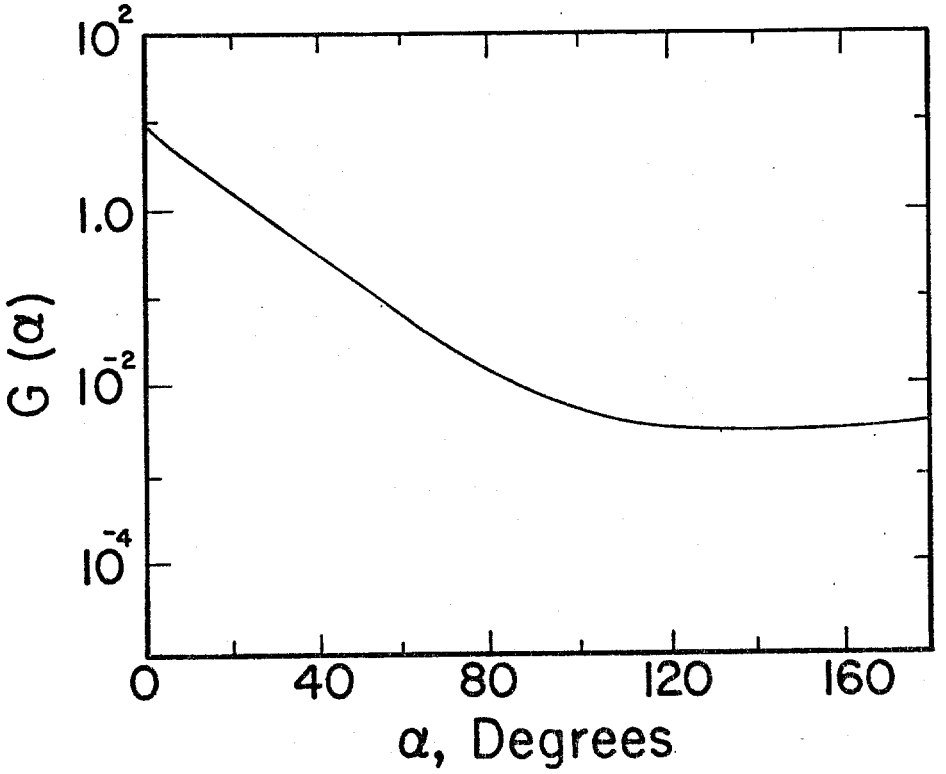

GEOMETRICAL SCATTERING n=1.20

Figure 9

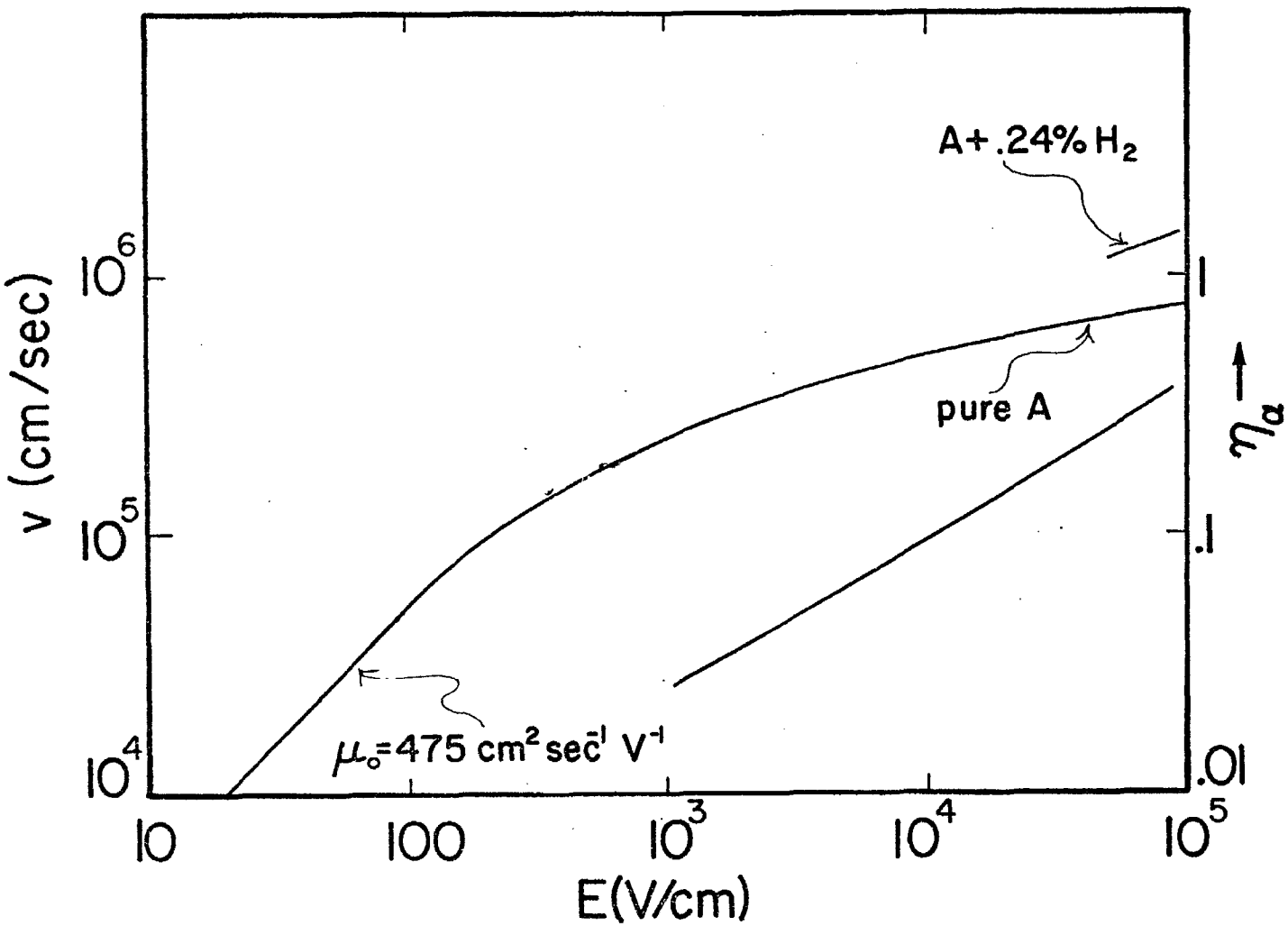
A+.24% H_2
pure A
μ_o=475 $cm^2 sec^{-1} V^{-1}$
v (cm/sec)
10^6
10^5
10^4
1
.1
.01
η_a
10
100
10^3
10^4
10^5
E(V/cm)

Figure 12.

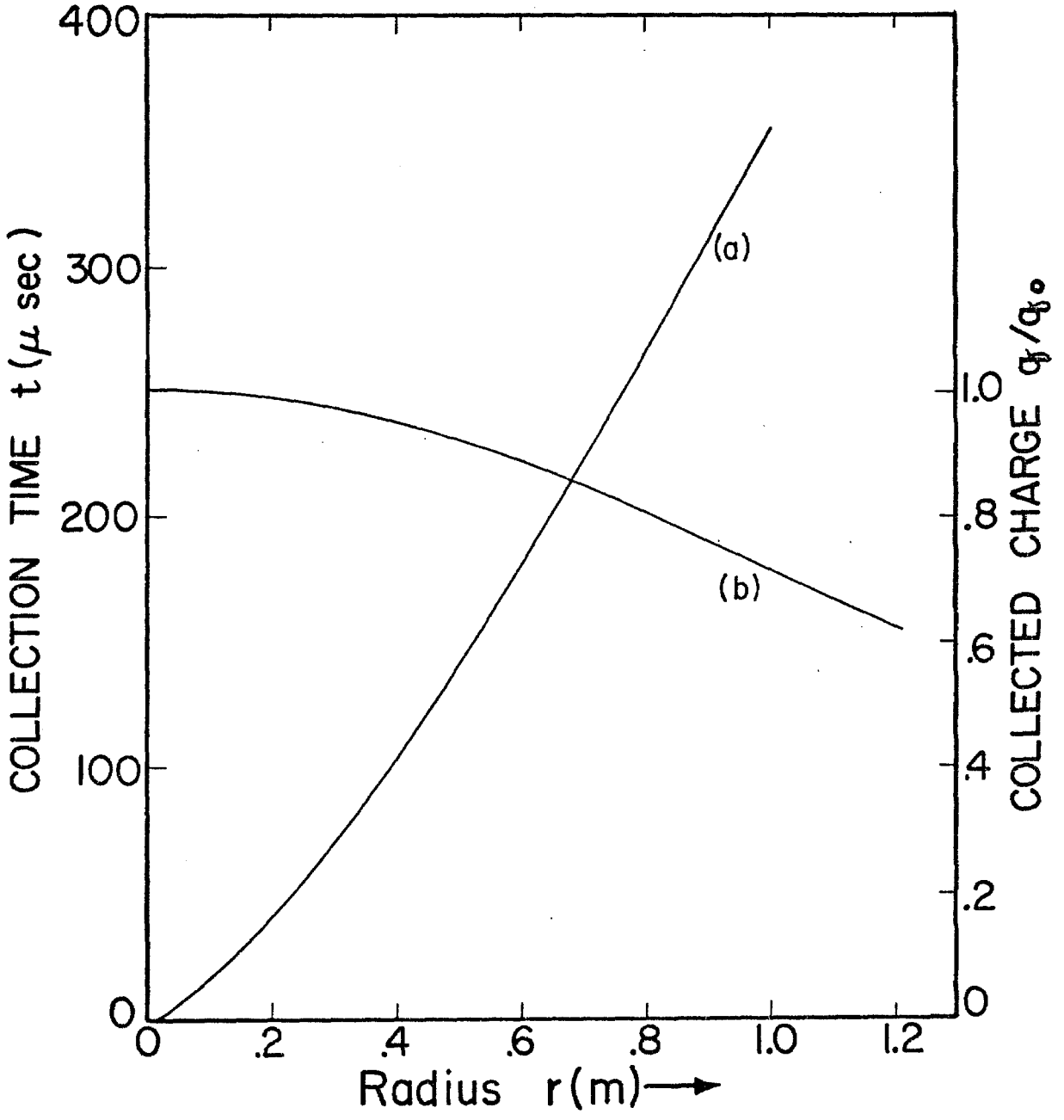
400
300
200
100
0
COLLECTION TIME t (μ sec)
(a)
(b)
1.0
.8
.6
.4
.2
0
COLLECTED CHARGE q/q₀
0
.2
.4
.6
.8
1.0
1.2
Radius r(m)

Figure 13

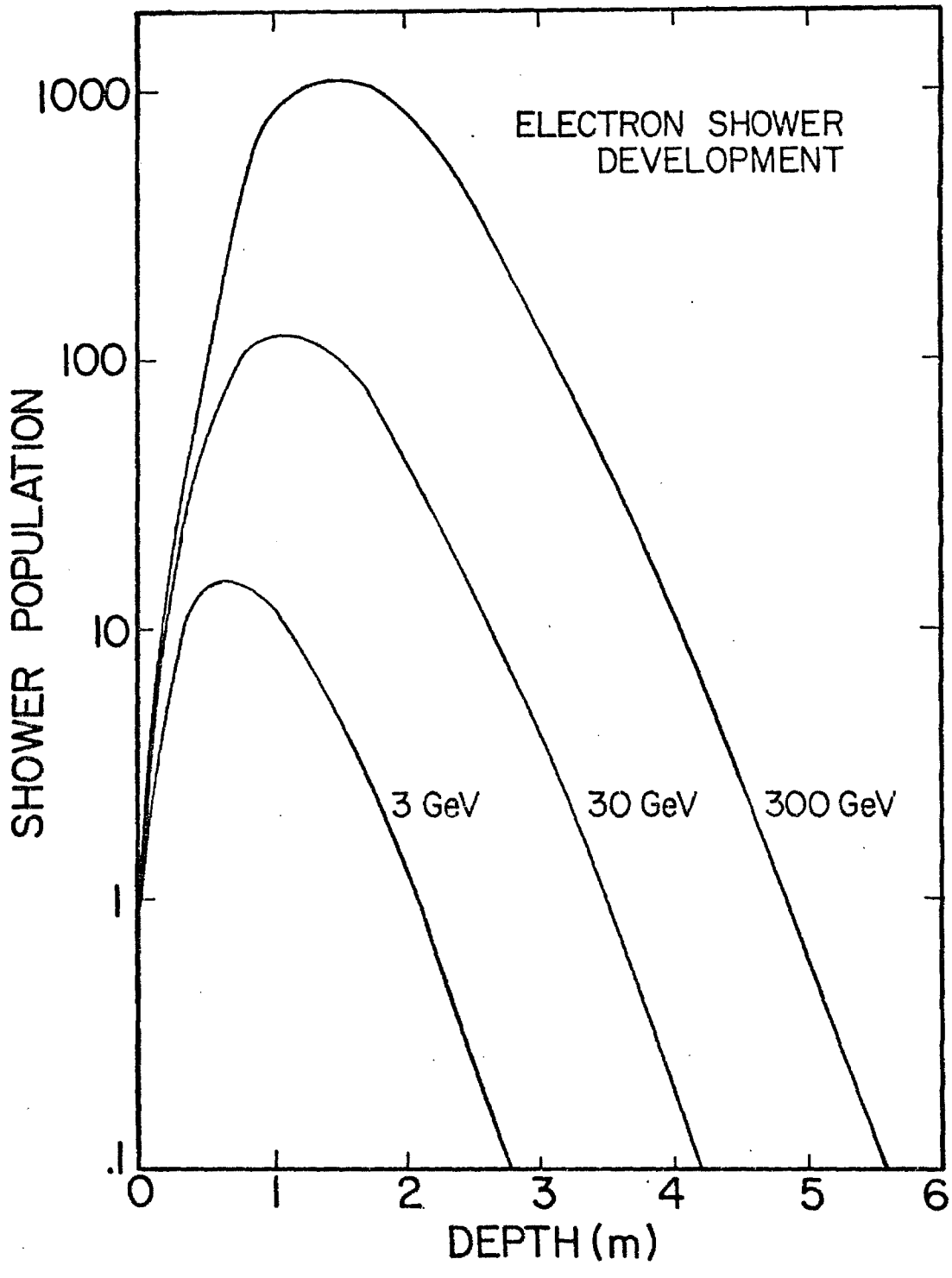
ELECTRON SHOWER
DEVELOPMENT
SHOWER POPULATION
1000
100
10
1
.1
3 GeV
30 GeV
300 GeV
0
1
2
3
4
5
6
DEPTH (m)

Figure 14

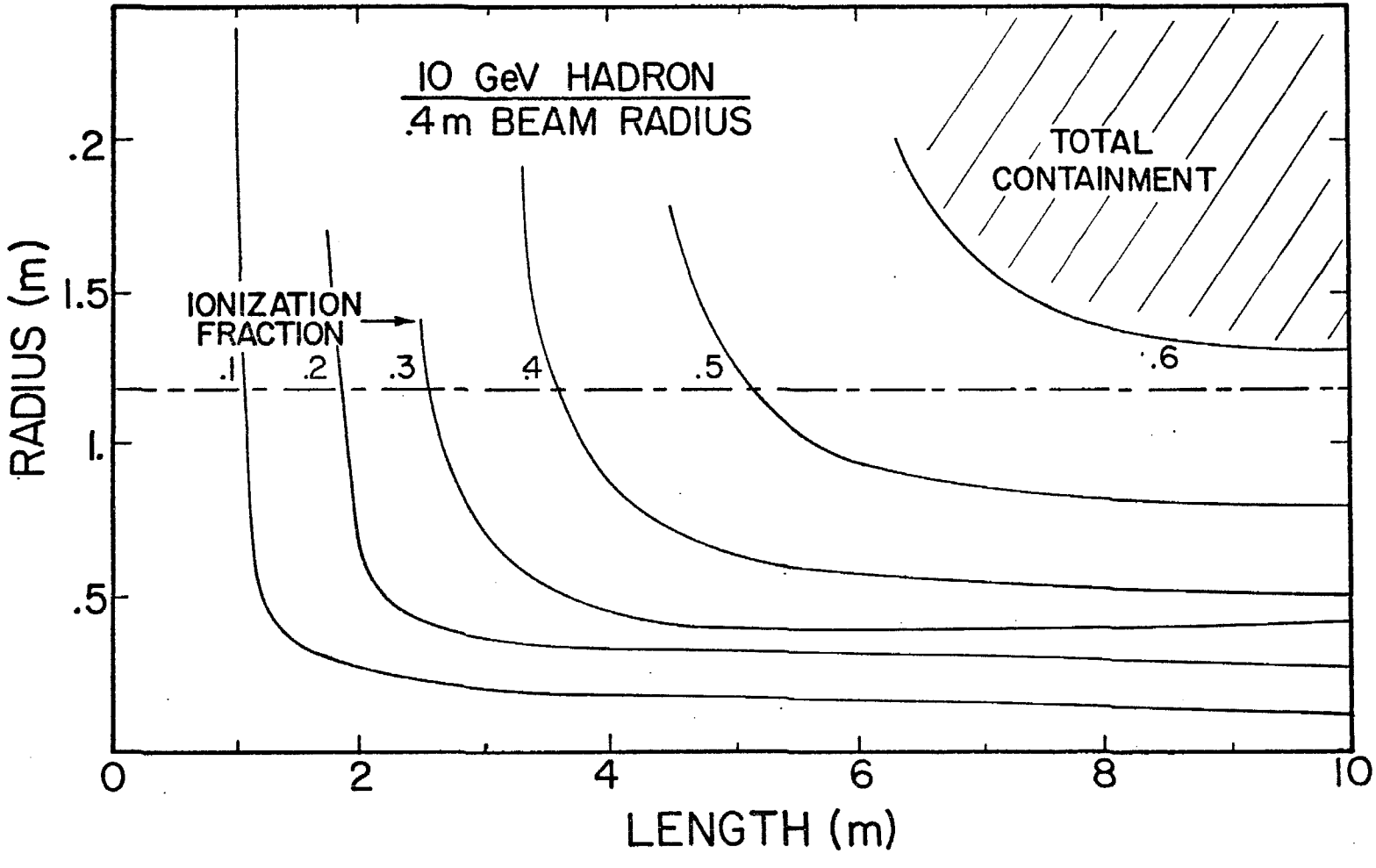
10 GeV HADRON
.4m BEAM RADIUS
TOTAL
CONTAINMENT
IONIZATION
FRACTION
.1
.2
.3
.4
.5
.6
RADIUS (m)
.2
1.5
1.
.5
0
2
4
6
8
10
LENGTH (m)

Figure 15.

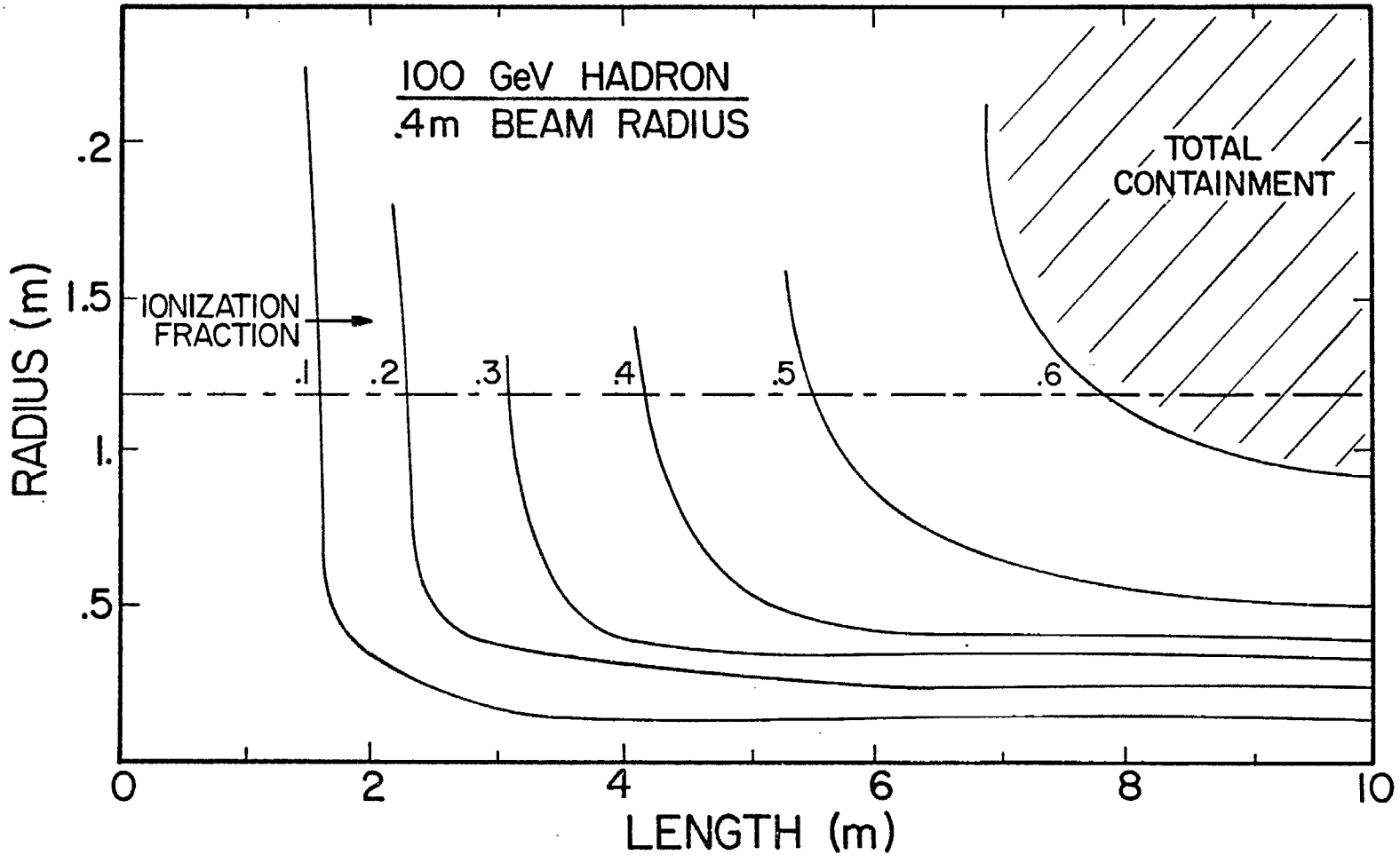
100 GeV HADRON
.4m BEAM RADIUS
TOTAL
CONTAINMENT
IONIZATION
FRACTION
.1
.2
.3
.4
.5
.6
RADIUS (m)
.2
1.5
1.
.5
0
2
4
6
8
10
LENGTH (m)

Figure 15b

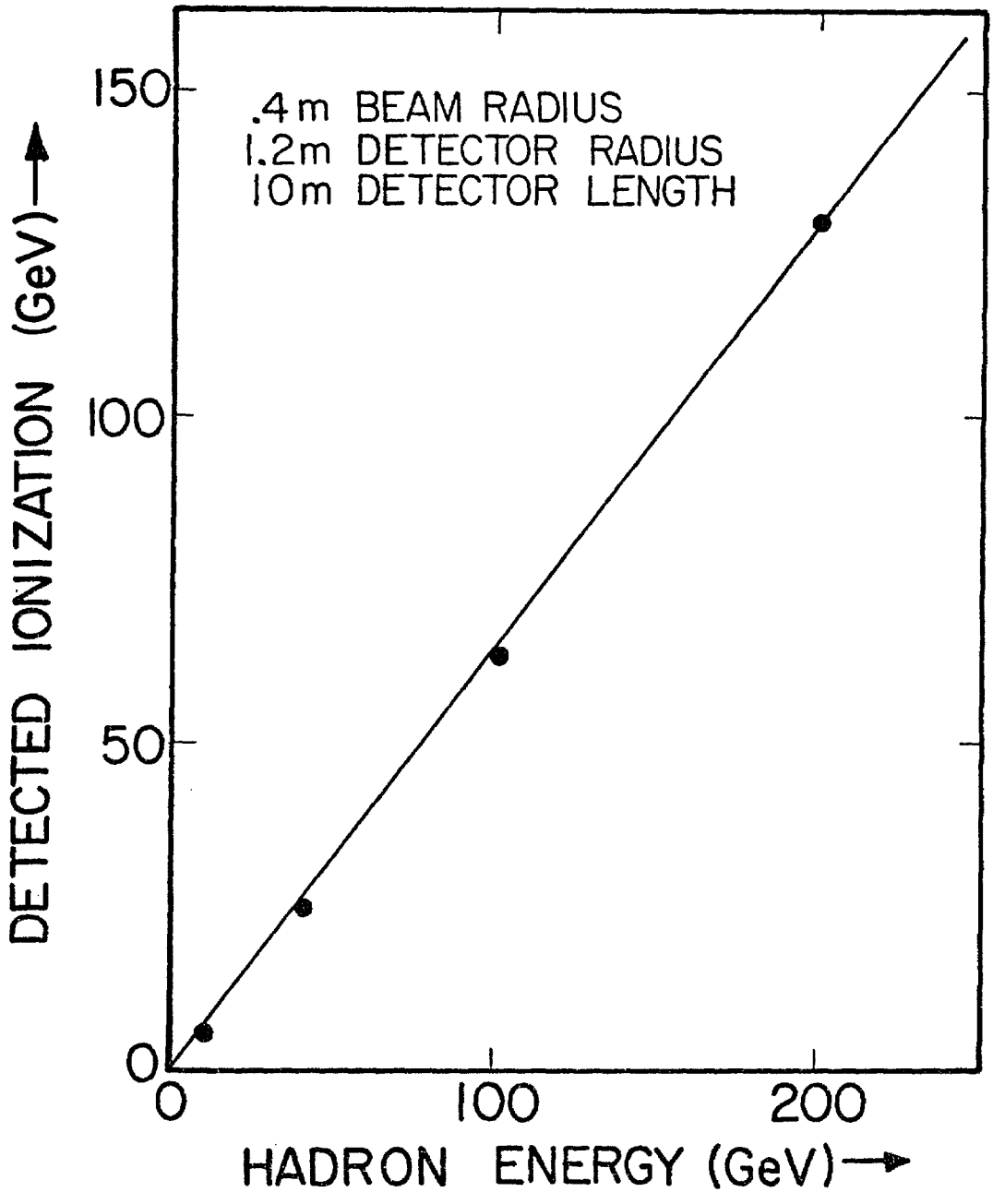
.4m BEAM RADIUS
1.2m DETECTOR RADIUS
10m DETECTOR LENGTH
DETECTED IONIZATION (GeV)→
HADRON ENERGY (GeV)→
0
50
100
150
0
100
200

Figure 16

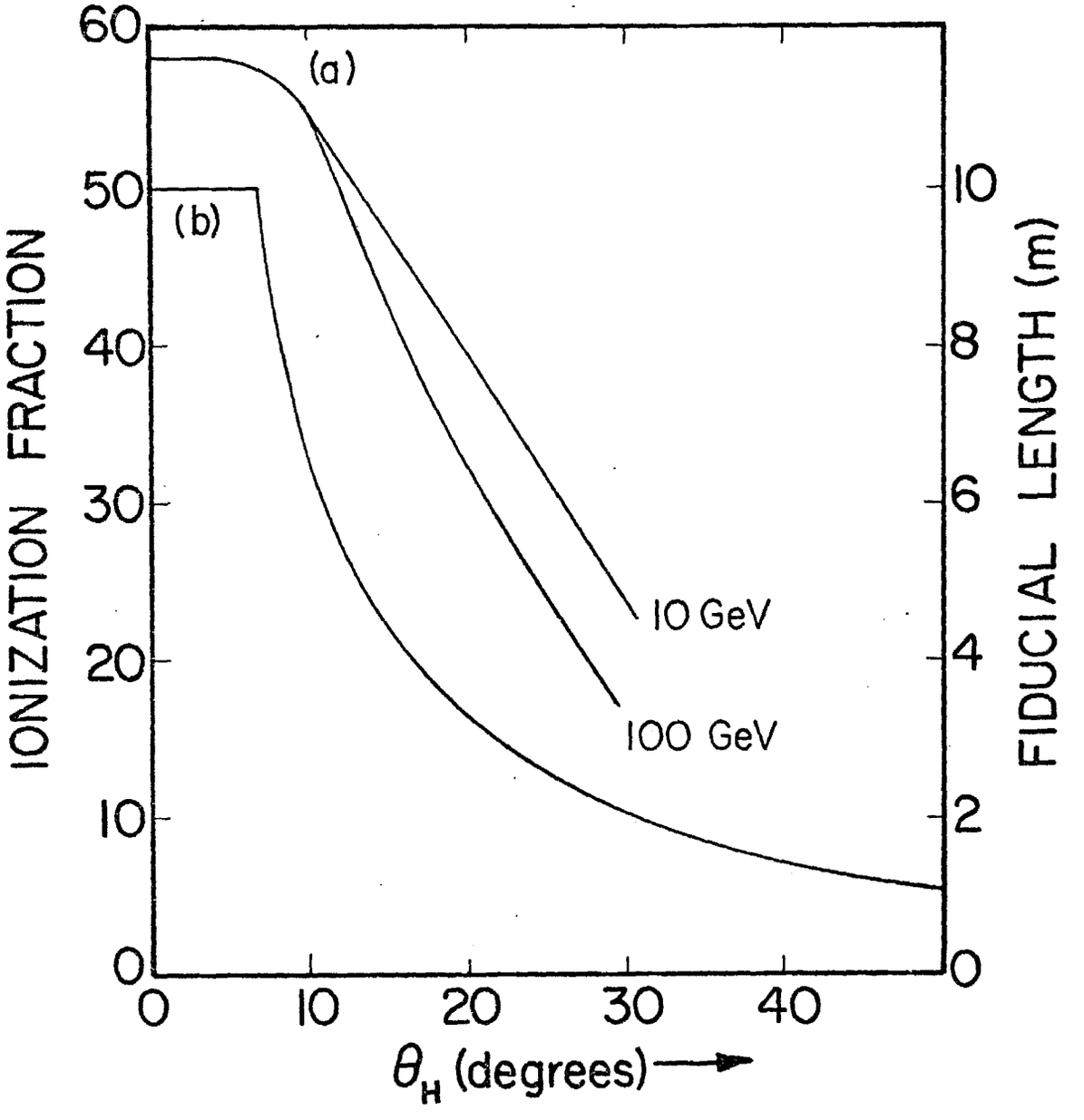
60
50
40
30
20
10
0
(a)
(b)
10 GeV
100 GeV
IONIZATION FRACTION
FIDUCIAL LENGTH (m)
10
8
6
4
2
0
0
10
20
30
40
θ_H (degrees)

Figure 17

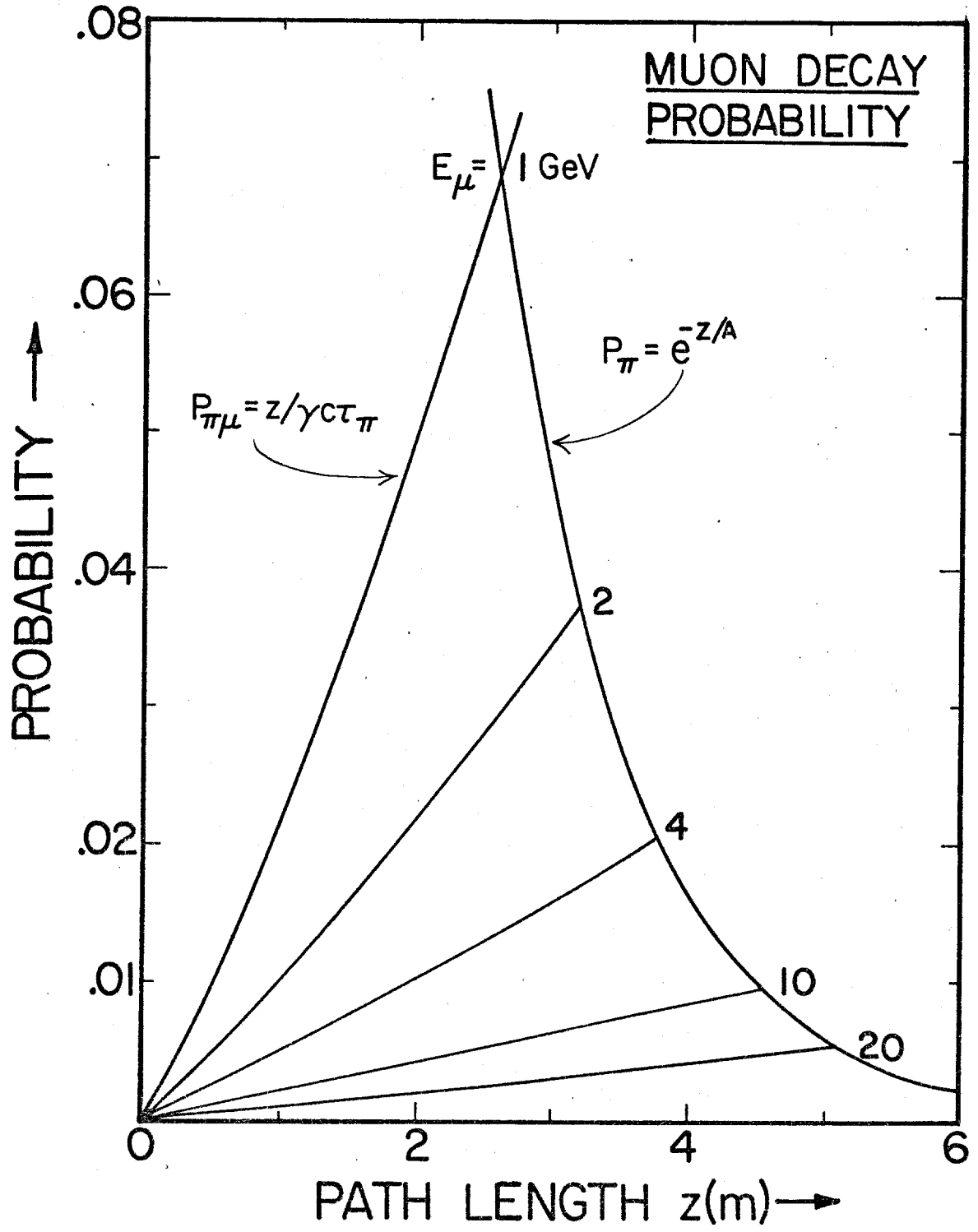
MUON DECAY
PROBABILITY
E_μ= 1 GeV
$P_\pi = e^{-z/\lambda}$
$P_{\pi\mu} = z/\gamma c\tau_\pi$
2
4
10
20
.08
.06
.04
.02
.01
PROBABILITY
0
2
4
6
PATH LENGTH z(m)

Figure 18

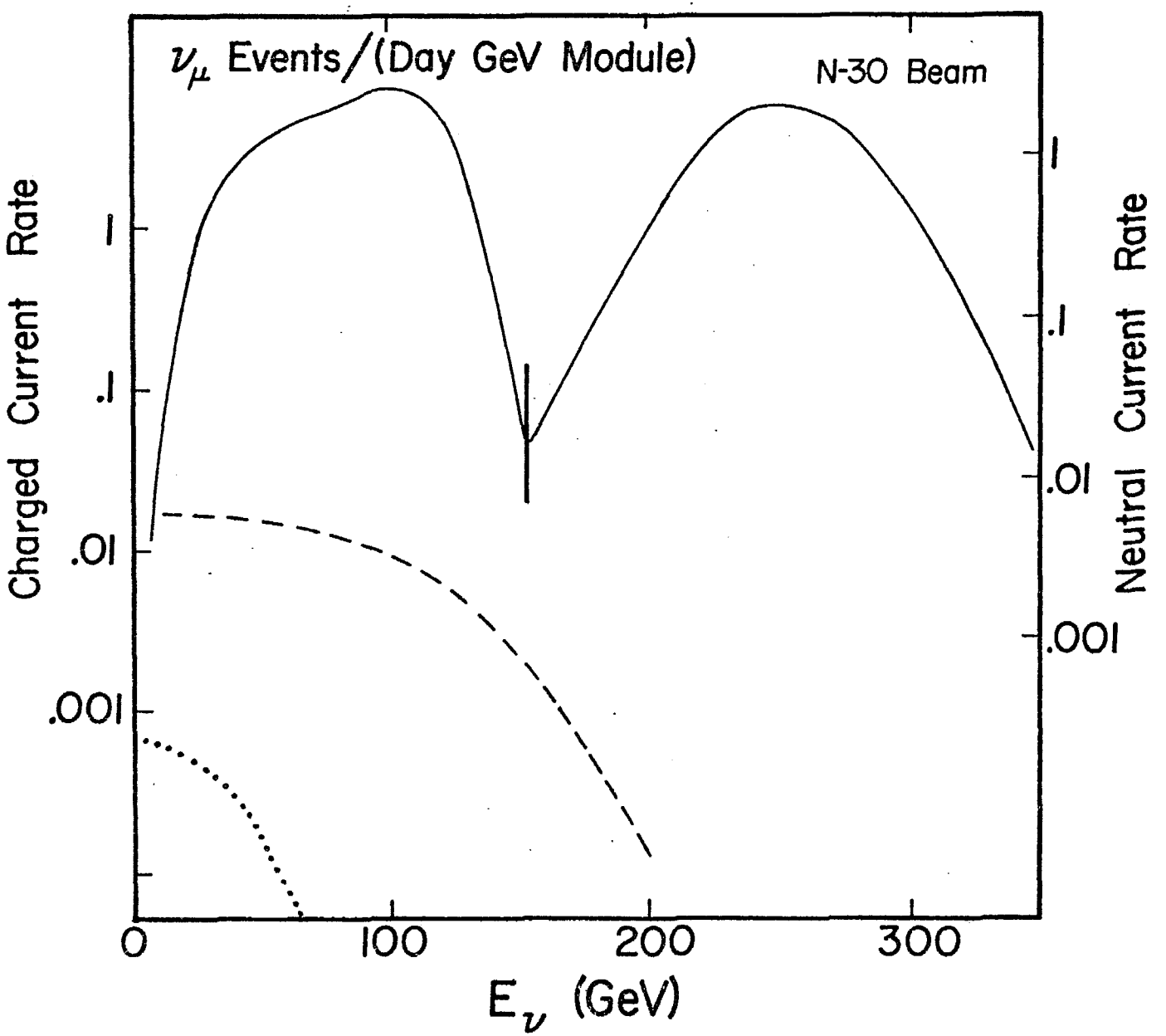
ν_μ Events/(Day GeV Module)
N-30 Beam
Charged Current Rate
Neutral Current Rate
1
.1
.01
.001
0
100
200
300
E_ν (GeV)

Figure 19a

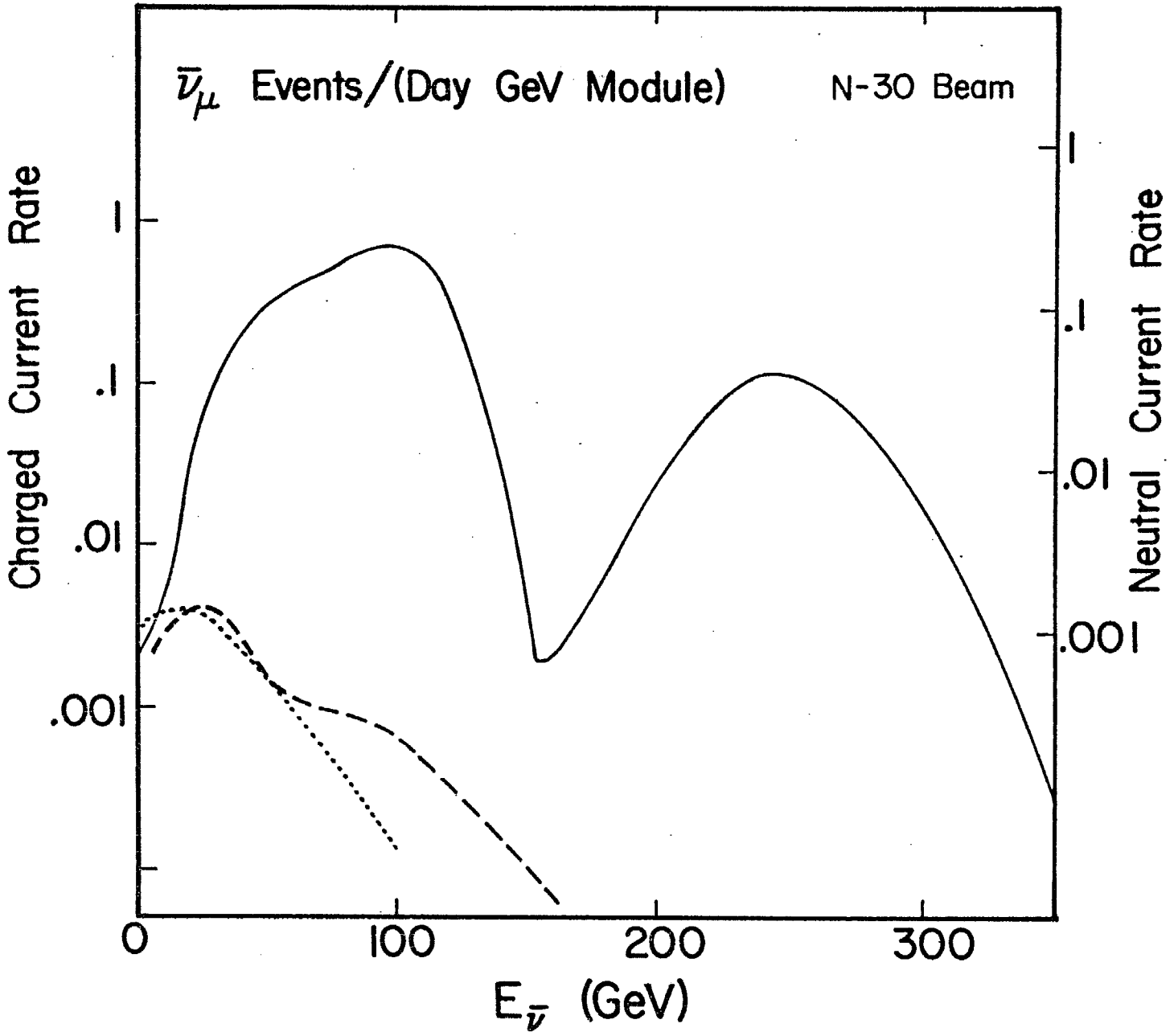
$\bar{\nu}_\mu$ Events/(Day GeV Module)
N-30 Beam
Charged Current Rate
Neutral Current Rate
1
.1
.01
.001
0
100
200
300
$E_{\bar{\nu}}$ (GeV)

Figure 19b

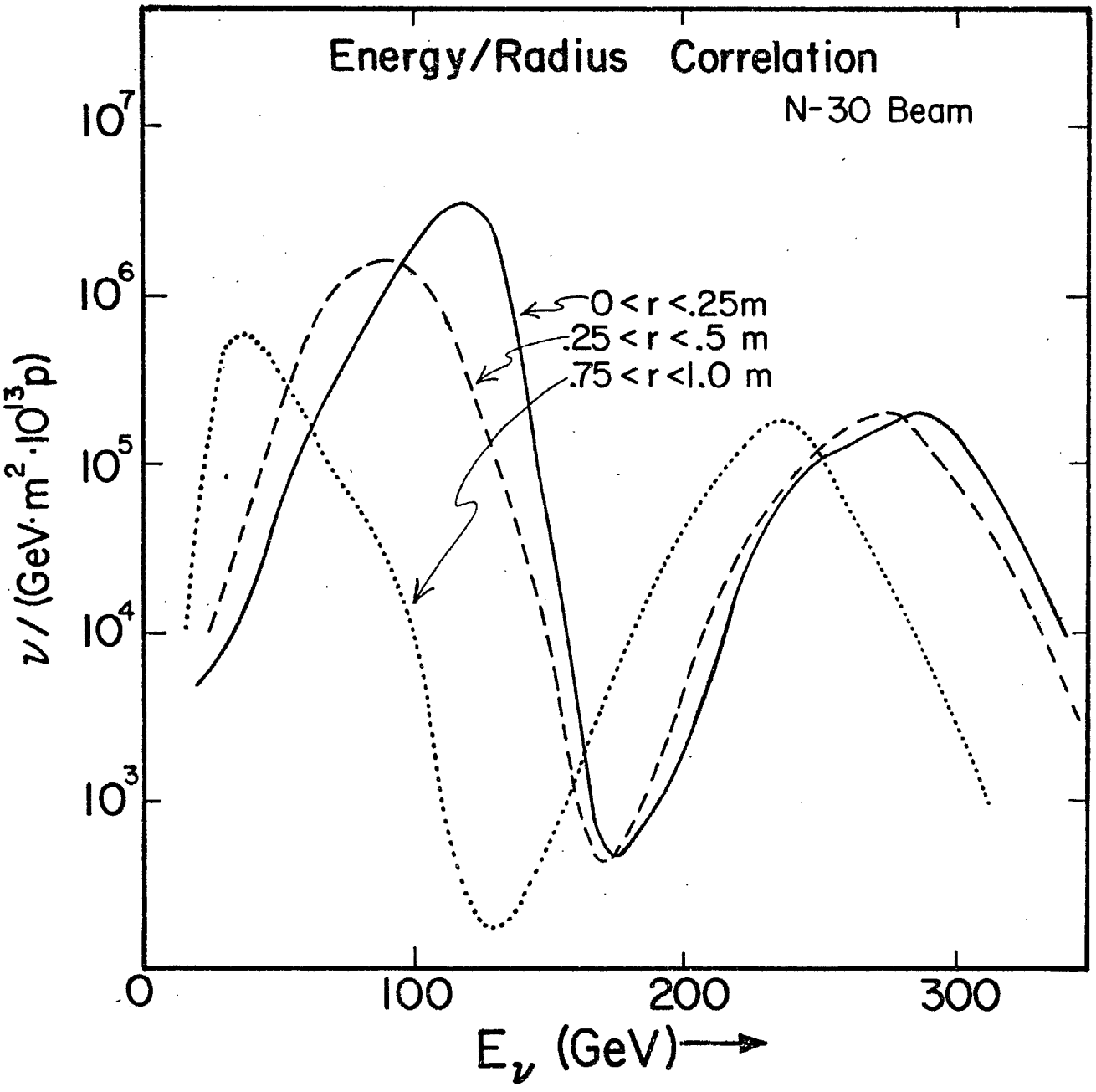
Energy/Radius Correlation
N-30 Beam
0 < r < .25m
.25 < r < .5 m
.75 < r < 1.0 m
10^7
10^6
10^5
10^4
10^3
$\nu/(GeV \cdot m^2 \cdot 10^{13} p)$
0
100
200
300
E_ν (GeV)

Figure 20.

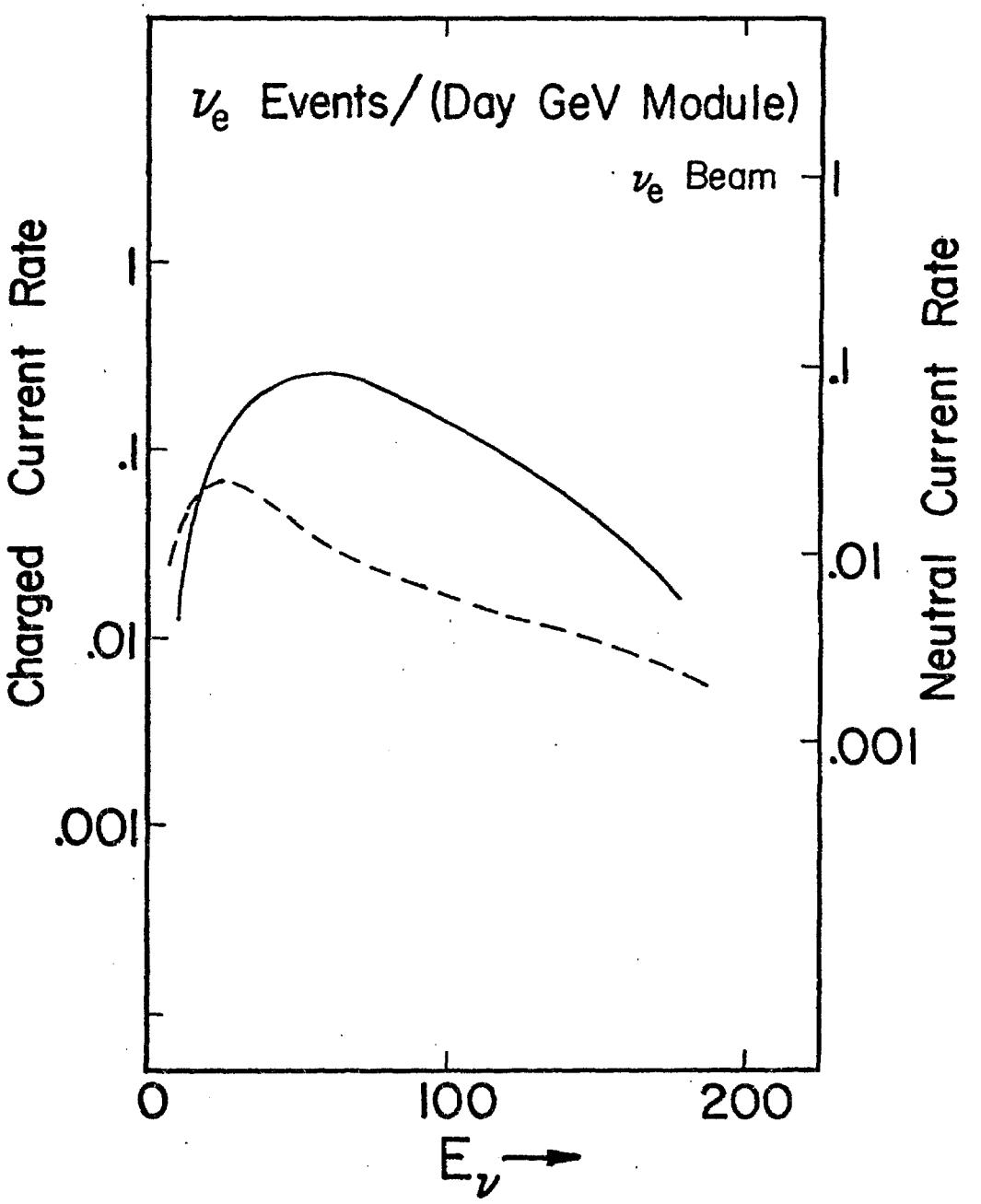
ν_e Events/(Day GeV Module)
ν_e Beam
Charged Current Rate
Neutral Current Rate
1
.1
.01
.001
0
100
200
E_ν

Figure 21a

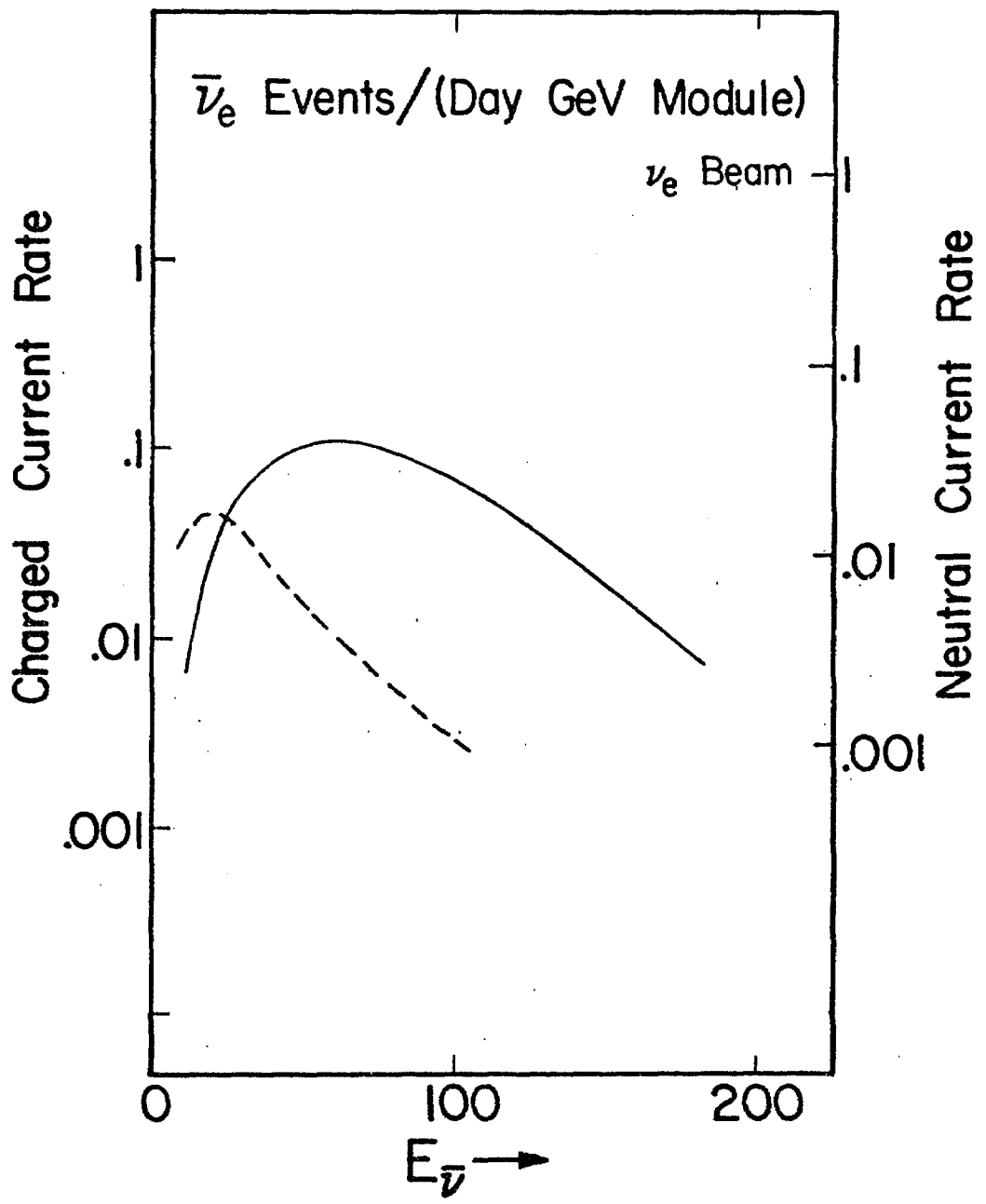
$\bar{\nu}_e$ Events/(Day GeV Module)
ν_e Beam
Charged Current Rate
Neutral Current Rate
1
.1
.01
.001
1
.1
.01
.001
0
100
200
$E_{\bar{\nu}}$ →

Figure 21 b

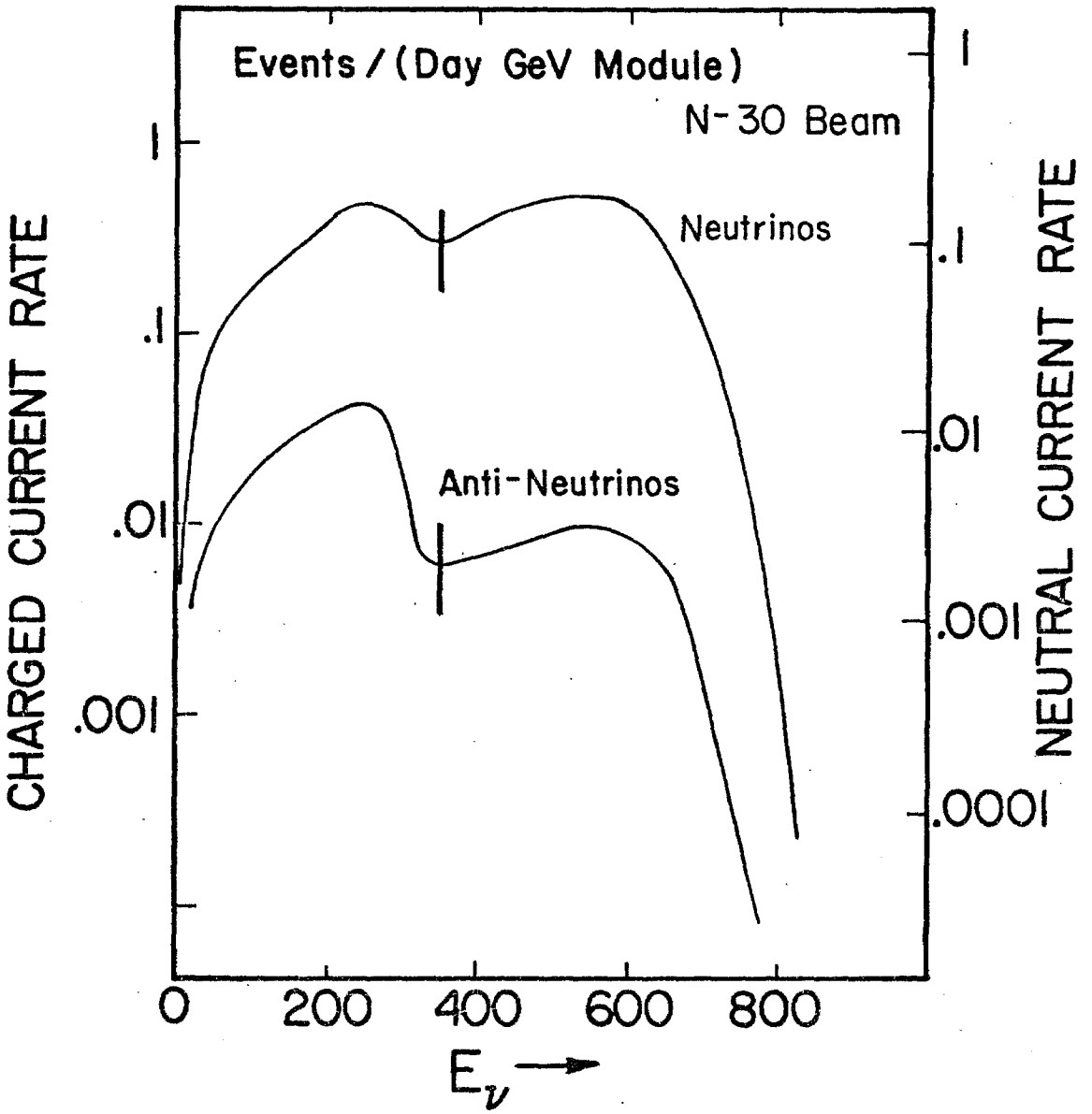
Events / (Day GeV Module)
N-30 Beam
Neutrinos
Anti-Neutrinos
CHARGED CURRENT RATE
NEUTRAL CURRENT RATE
1
.1
.01
.001
.0001
0
200
400
600
800
E_ν →

Figure 22

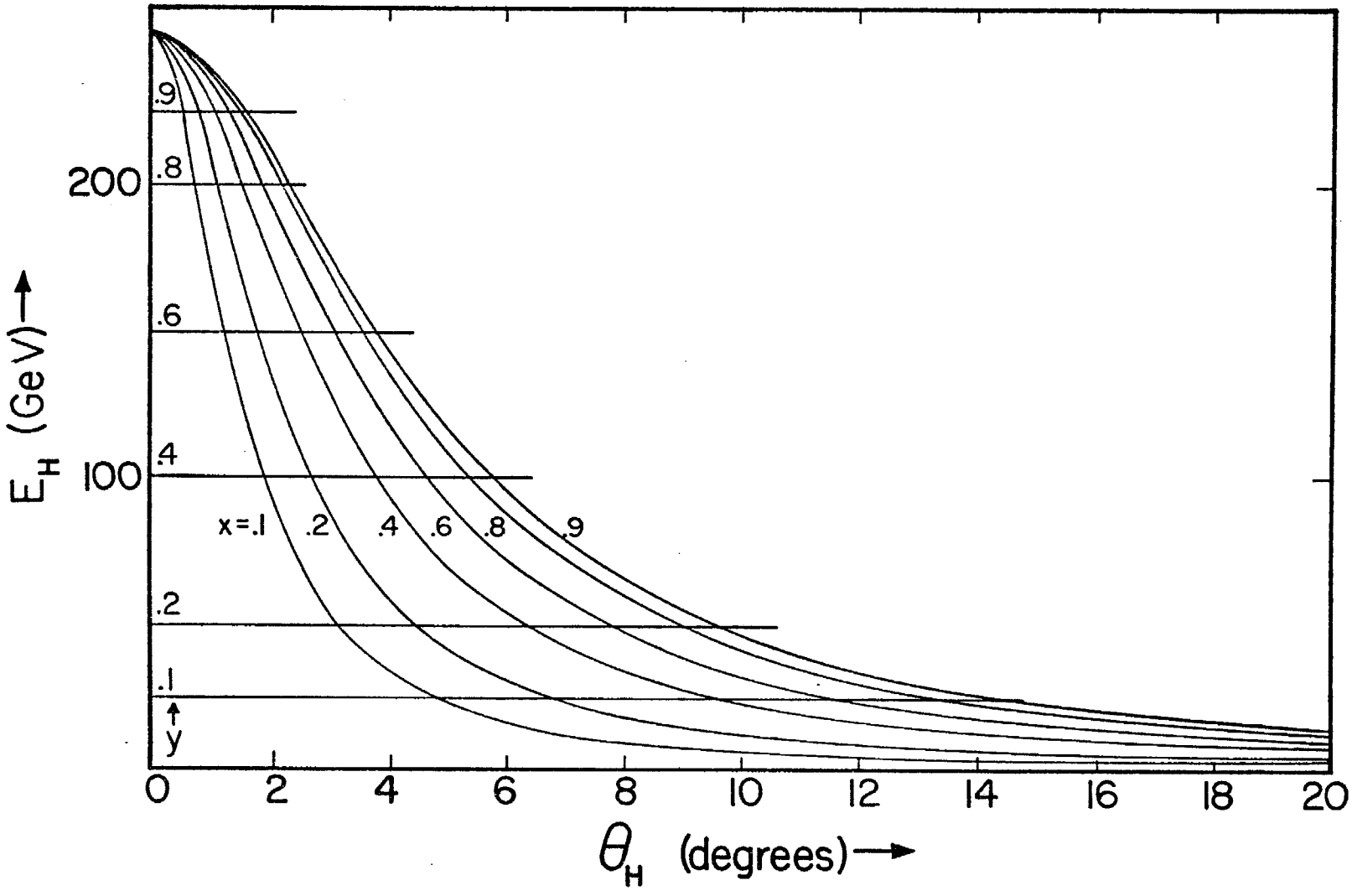
.9
.8
.6
.4
.2
.1
y
200
100
E_H (GeV)
x=.1 .2 .4 .6 .8 .9
0 2 4 6 8 10 12 14 16 18 20
θ_H (degrees)

Figure 1b

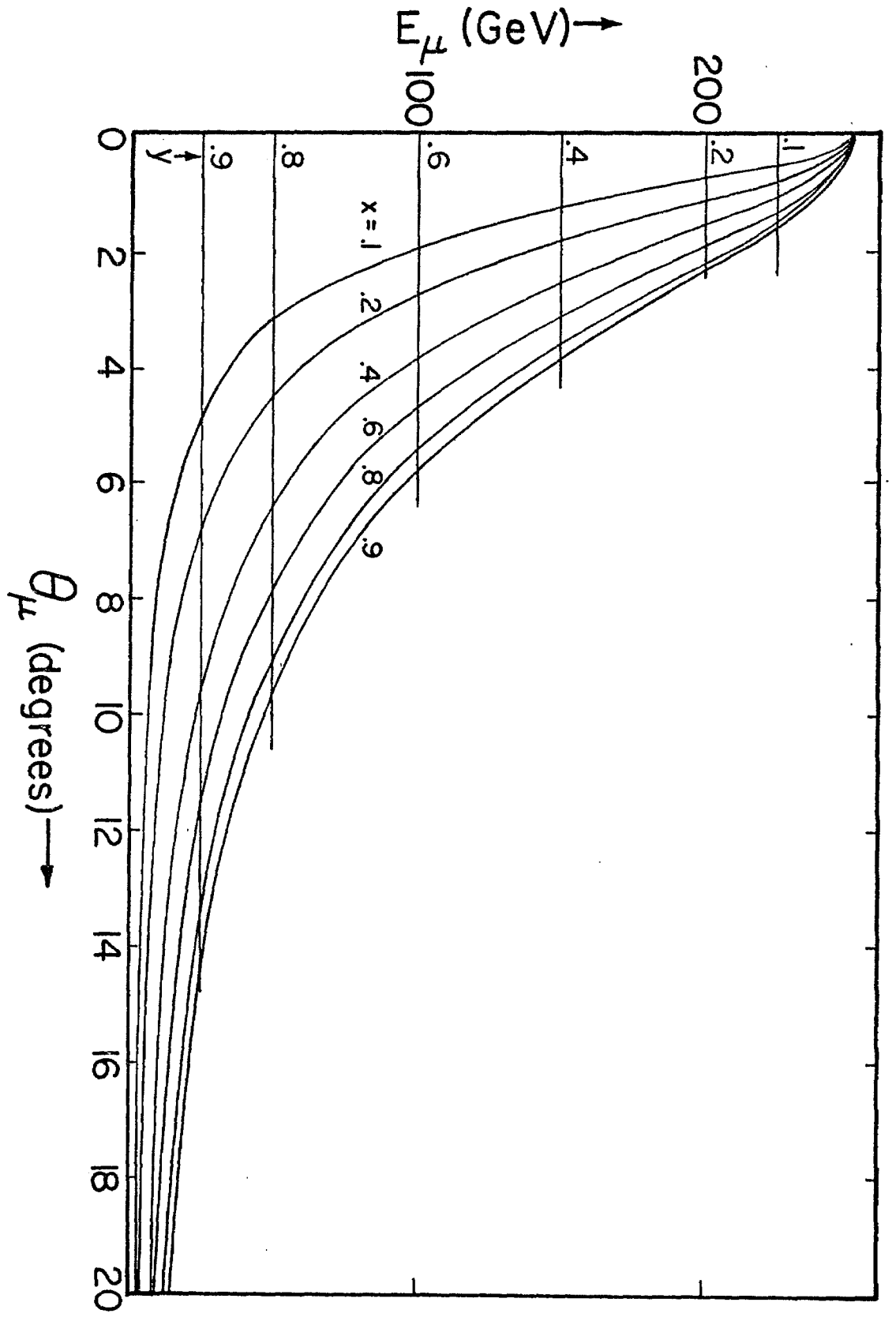
E_μ (GeV)→
100
200
0
2
4
6
8
10
12
14
16
18
20
θ_μ (degrees)→
y→
.9
.8
.6
.4
.2
.1
x=1
.2
.4
.6
.8
.9

Figure 23a

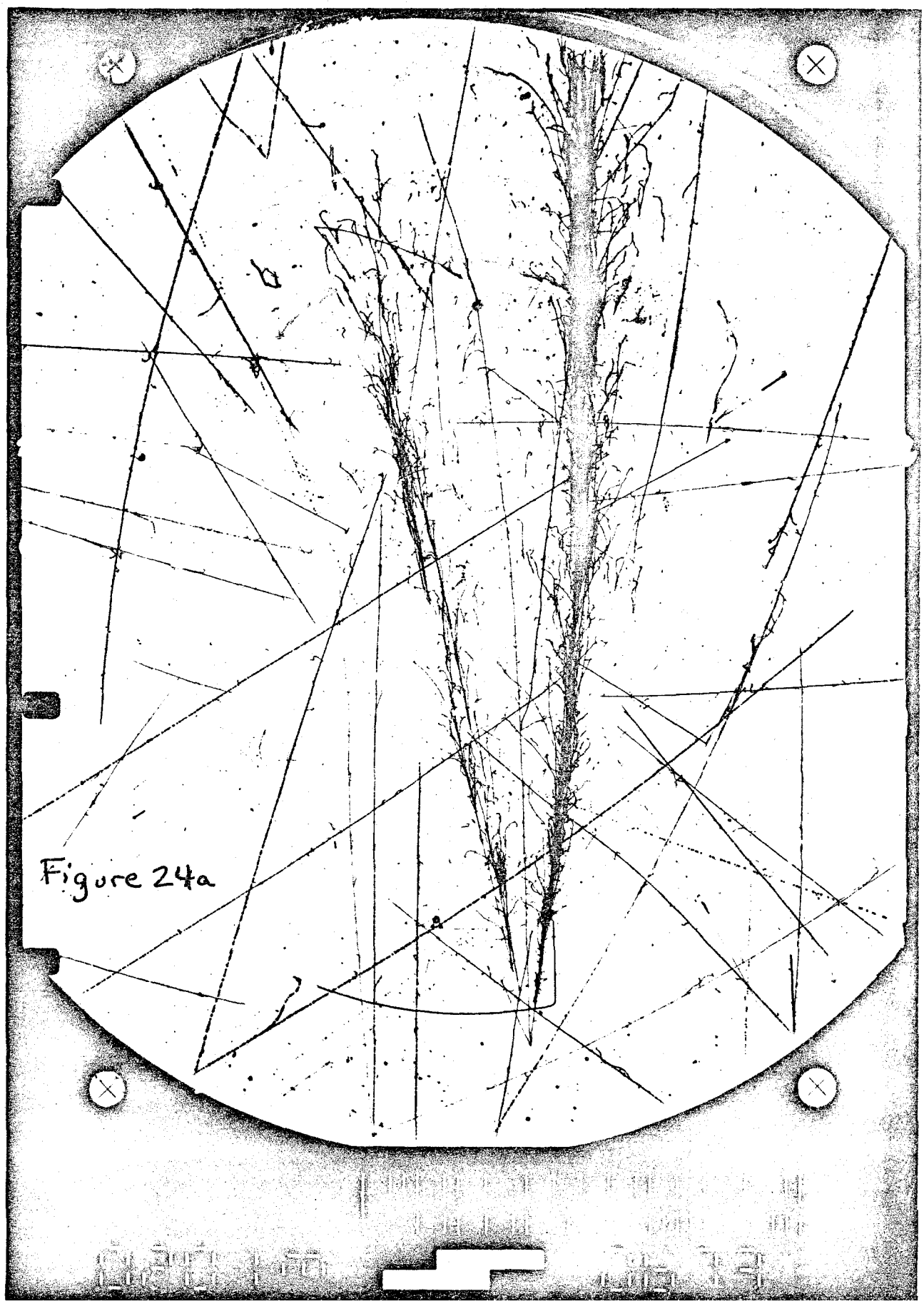

Figure 24a

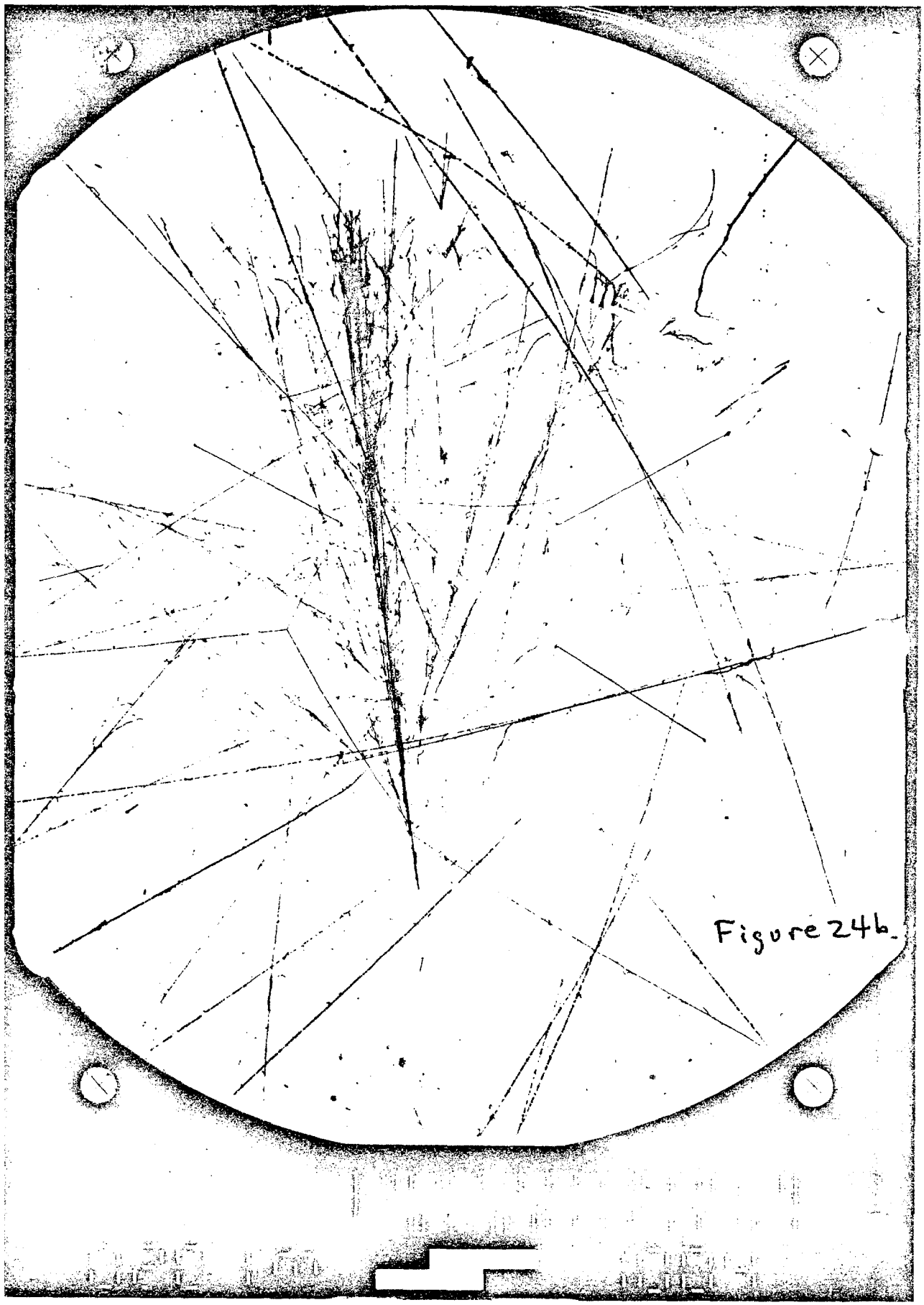

Figure 246.

ARGONAUT

A Novel Detector for Very High Energy Neutrino Interactions

G. Harigel[†], H. Kautzky, P. McIntyre[‡], and A. Van Ginneken
Fermi National Accelerator Laboratory, Batavia, Illinois 60510

ADDENDUM 1

Fermilab Proposal No. 601D

Scientific Spokesman:

Peter M. McIntyre
Fermilab and Harvard University

Telephone: (312) 840-4307

May 5, 1978

[†] On leave of absence from CERN.
[‡] On leave of absence from Harvard University.

We address here the questions posed by the PAC and by the preliminary evaluation. We also present in detail the proposed experimental program for Phase 1--Prototype Tests, as described in the proposal.

We prefer to begin by addressing the general question (VI. 1, 2) of comparing ARGONAUT with existing bubble chamber and counter experiments.

VI. 1. Bubble chamber aspects

a) An advantage of our proposed detector over the existing 15' Bubble Chamber (filled with a heavy neon/hydrogen mixture) is its larger fiducial mass (factor of merit ~25).

b) An advantage of our detector is the (immediate) availability of total calorimetry of electromagnetic and hadronic showers, whereas it is almost impossible (or at least extremely time-consuming) to obtain this information from 15' Bubble Chamber pictures.

c) An advantage of our detector is to identify muons mainly inside the liquid. (This topic is discussed in detail later.) The 15' Bubble Chamber has insufficient track length to clearly identify muons inside the chamber, necessitating an External Muon Identifier.

c) Advantages of our detector over an (hypothetical) enlarged version of the 15' Bubble Chamber (or modules equivalent to the argon chamber modules) with a fiducial

mass of about 350 tons (and perhaps equipped with a magnetic field of 3 T) are:

(1) considerably lower price. The price to increase the 15' Bubble Chamber would probably scale linearly with the volume, and the price for the magnet would scale even faster than linearly with volume.

(2) Considerably simpler chamber design with argon than with hydrogen as bubble chamber liquid. Argon is a non-explosive liquid (no major safety problems) and requires modest cryogenics.

(3) Significantly lower operating costs, because cooling system is much simpler, consumes only LN_2, the cost of liquid argon is only ~ 2% that of neon. We anticipate that ARGONANT could be operated with about the present crew size of the 15' Bubble Chamber, whereas a larger version of the 15' Bubble Chamber would require a multiple of such a crew.

(4) The reliability of each ARGONAUT module should be considerably higher than any neon/hydrogen bubble chamber. Furthermore, each module can be emptied, repaired, and refilled while the other modules are operating.

e) Liquid argon presents both advantages and disadvantages as a bubble chamber fluid. The radiation lenth X and absorption length A are considerably shorter than in hydrogen and neon/hydrogen mixtures. This facilitates total-absorption calorimetry and muon identification, but presents some limitations in identifying photon/electrons.

In this respect argon resembles Freon 13B1.

After establishing experimentally the operating characteristics of liquid argon, we will investigate several possible fluids (methane, ethane) that could be mixed with argon to vary X, A while still permitting ionization drift calorimetry.

f) The absence of magnetic field on the bubble chamber volume presents both advantages and disadvantages. Analysis for E_H, θ_H, E_e, θ_e is particularly simple in zero field. On the other hand, γ/e separation and V^o identification certainly suffer. For these latter purposes, a moderate field (~ 0.5 T) may suffice. A preliminary design and cost estimate for such a magnet is presented later.

VI. 2. Counter physics aspects

As compared to counter neutrino experiments, ARGONAUT has the following advantages:

a) We always see the vertex of an interaction clearly; this is crucial to eliminate backgrounds for rare leptonic processes, as will be discussed later.

b) We can determine in most cases the multiplicity of an interaction.

c) In ARGONAUT we can identify prompt electrons. In doing so we must distinguish between electrons (e^+, e^-, pairs) originating from the vertex within ~ 1 cm, and photon showers (π^o decays) either from the ν interaction or from secondary hadron interactions.

The ability to identify prompt electrons is difficult if not impossible in any existing or proposed counter experiment.

d) ARGONAUT has better spatial and energy resolution, for both electromagnetic and hadronic showers.

ARGONAUT is comparable to counter experiments in the following respects:

e) Muon identification would be comparable to that in the iron calorimeter of E310 at Fermilab and WA-1 at CERN (see later section). μ momentum measurement would be similar to most iron toroid spectrometers--indeed better if a magnetic field is provided on the bubble chamber itself.

f) For the beams and experiments discussed in the proposal, ARGONAUT can record all neutrino interactions without significant dead-time or cycle losses, even with the largest number of targeted protons. Multi-event capability arises naturally from the modular design. In the N-30 dichromatic beam, we would observe ~ 5 ν interactions per pulse of 2×10^{13} targeted protons; these would in general occur in separate modules.

The modular design of ARGONAUT makes it possible to rearrange or modify the detector at a later date for minimum cost. For example, a liquid hydrogen target could be located just upstream of each bubble chamber to allow detailed study of νp, $\bar{\nu} p$ processes. Magnetic field could be provided for some or all bubble chambers. Most important, ARGONAUT will retain the flexibility to be readily modified to optimally study new phenomena as we explore the energy ragne of the Energy Doubler/Saver.

ARGONAUT has been designed to achieve the best physics (event rate, background rejection, calorimetry, lepton identification) achievable with today's technology. Its cost is in line with that of major detectors at other laboratories (TPC at PEP, $\bar{p}p$ at CERN). Its operation would require a level of support comparable to that for the 15' Bubble Chamber. It represents in our opinion a true advance with respect to the present neutrino experiments at Fermilab and the formidable array of neutrino experiments at CERN.

I. Electromagnetic Phenomena

1. Without a magnetic field on the bubble chamber, we cannot separate single electrons (coming from the vertex) from Dalitz pairs. The higher the field strength the better is the separation, particularly to open the Dalitz pair before any other electromagnetic shower could obscure it. Before settling on any specific field value we will extrapolate the results from experiments E-28 and E-53 to our shorter radiation length.

2. If we understand the question correctly, you ask for the efficiency of separation of electrons and photons, each coming from the event vertex. The photons would convert later either into electron pairs or Compton electrons. The typical gap between the origin of the electron and the photon conversion point is X = .17 m. A magnetic field gives limited help since it opens up the shower.

   If we interpret your question differently, you ask if we can distinguish between a neutrino induced single electron event and a background photon. Our answer must be <u>no</u> without a magnetic field on the bubble chamber. For the required field strength similar arguments as for question I.1. are relevant.

3. As stated in the proposal, the energy resolution for an electromagnetic cascade is $\sigma_E \sim 0.5$ MeV. The major uncertainty in measuring the energy of an electron or electron pair would be the problem of separating its cascade from other e(γ) cascades. Here we expect to use the bubble chamber image to advantage. Unless two cascades overlap completely, we could make a track-count estimate

of the energy in each cascade, and apportion the measured ionization accordingly.

4. The angle of an electromagnetic shower would be measured using its statistical development, as discussed in the proposal: $\sigma_\theta \sim \sigma/6X = .001$. The corresponding resolution on transverse momentum is then $\sigma(p_\perp) \sim \sigma_E\theta + E\sigma_\theta \lesssim .001E$. This assumes of course that the cascade is separated from other $e(\gamma)$ cascades, as discussed in I.3.

5. Questions I.5, II.3., and V.1. are closely related. Measurement of invariant masses is difficult in the following instances:

   1) If there is considerable overlapping in beam direction of hadronic and electromagnetic showers. The fraction of energy contained in each shower cannot be well determined by calorimetry. The accompanying bubble chamber photo could help estimate the energy division.

   2) We believe that we can distinguish hadronic showers from electromagnetic showers, due to the latter's characteristic appearance (bremsstrahlung, pair creation, multiple scattering) and the large value $A/X \sim 6$. This means, we know the mass of the electron (positron), the direction of the shower, and the total energy.

   However, we face serious difficulties if we want to distinguish between hadronic showers of various origin. At the moment we expect to be unable to determine with sufficient confidence the mass of the primary hadron. Only a magnetic field can help.

The measurement of the angle of the center line of the shower in respect to the beam axis from the bubble chamber photos is of the order of a few mrad.

The precision of the energy measurement of showers is discussed in another chapter.

6. The probability to associate an electron shower to the primary vertex as opposed to secondary interactions can be viewed under two aspects:
Firstly, it depends upon the distance between primary vertex and secondary interaction. A small interaction length of the liquid is not desirable from this point of view. However, the interaction lengths of argon and pure neon are similar, and not much smaller than in neon/hydrogen mixtures used in the 15' Bubble Chamber. The number of unanalyzable events mainly due to close secondary interactions in experiment #546 is of the order of 2 to 3%; we expect a somewhat larger value for argon. For the high-energy N30 neutrino beam, we expect the contribution of these backgrounds to decrease, since high energy photons from secondary interactions would come mainly from charge exchange, and such cross-sections decrease with energy.

Secondly, we note that the measurement of electron angle using its statistical development is more straightforward without magnetic field. This is of course hard to quantify without measurement. The precision in the determination of the line of flight should increase with increasing energy of the shower. An experimental study of a sample of photos taken in the 15' Chamber

with and without magnetic field could help to quantify the above argument.

II. 1. See point 2 of the answer to I.5.

2. As we understand this question, it addresses the concept of using energy flow to search for final state neutrinos. This concept has been the focus of several experiments and proposals at Fermilab. (P-310,P-602D). We do not know how to model the detail of a typical hadronic final state sufficiently well to make a believable calculation of energy flow. We propose to measure experimentally this question in Phase II of ARGONAUT (the first module). We can however state with confidence that ARGONAUT will provide the best energy flow information available from calorimetry. Furthermore, in ARGONAUT we can use the image (and momenta if we have magnetic field) to refine the search for missing neutrinos.

III. 1. Without a magnetic field, we obscure a certain region after the event vertex, where we cannot find the charged decay products of K_s^o. Combining information from our calculations on shower development with scanning results on recent bubble chamber experiments leads us to estimate that the unobservable (obstructed) fraction of such decays is much smaller than 50%. It is hard to estimate how many decays within such a shower can be still identified. The probability to detect the neutral decays inside the shower is expected to be zero. However, we are optimistic

to find neutral decays outside the obscured region, provided we are able to distinguish these decays from other background, e.g., π^o.

We believe, that a short run of the 15' Chamber with an exposure of about 10 kpx, filled with 64 atomic % Neon in a wide-band neutrino beam, without magnetic field, and a subsequent comparison of results with E-53 would answer this question far better than the above estimate.

The detection efficiency in a magnetic field around the argon chamber modules increases with increasing field strength.

2. K^o regeneration: Half of the K^o, $\bar{K}^o$ produced in neutrino interactions decay as $K_s^o \to \pi\pi$ and would be observed with good efficiency in ARGONAUT. The remainder would decay as K_L^o if travelling in a vacuum. In liquid argon, however, some K_L^o's would regenerate into K_s^o, which in turn would decay and enhance the K^o identification yield.

Here we calculate the total K_L^o regeneration probability. The regeneration amplitude is $\rho(z) = \pi N \frac{|f-\bar{f}|}{k}$ where $N = 1.74 \times 10^{22}$ cm^{-3} is the density of nuclei and $k = p/hc$ is the K^o momentum [cm^{-1}].

The total regeneration probability is

$$P_r \sim \int_o^\infty \rho(z)\, e^{-z/A}\, dz = \pi N A \frac{|f-\bar{f}|}{k} \quad .$$

E-486 has recently measured the A dependence of regeneration. The find $\frac{f-\bar{f}}{k} = 25\ p^{-.59}$ mb in aluminum and $\frac{f-\bar{f}}{k} \propto A^{.74}$.

We calculate from this $\frac{f-\bar{f}}{k} = 33\ p^{-.59}$ mb in argon, and obtain

$$P_r = .18\ p^{-.59} = .045 \text{ at } p = 10 \text{ GeV/c.}$$

We thus expect regeneration to add only a small fraction to the direct K_s^o decay sample.

3. The measurement of the momentum of K_s^o should not be a problem, as long as we consider only the charged decay mode and moderate energies ($\lesssim$ 10 GeV): We can use then large-momentum relations for the charged pions. The efficiency and momentum limit depends only on the vertex distance from the exit wall of the bubble chamber.
In the case of secondary interactions we have to sum the momenta of all outgoing tracks or isolate their contribution in the segmented calorimetry. For the neutral decay mode, we expect valuable results in those events where other background is low and if we are able to do calorimetry on the electromagnetic showers of the decay particles.

For very high momentum K_s^o and charged decays, analysis requires a magnetic field.

4. K_s-Λ separation is clearly impossible without a magnetic field on the bubble chamber. See the later section on magnet for separation capability with magnetic field.

IV. 1. The direct observation of charm particles faces the same problems as such experiments in the 15' Bubble Chamber. Our resolution is somewhat worse than in hydrogen or neon/hydrogen, because of our optics and the absence of a magnetic

field on the bubble chamber (see later). Huge size and very high resolution are incompatible requirements (A nice detector for possible charm observation by proton interactions is, e.g., the Mini Bubble Chamber, as described in Fermilab proposal # 606) or hybrid emulsion experiments ("Observation of a Likely Example of the Decay of a Charmed Particle Produced in a High Energy Neutrino Interaction," E.H.S. Burhop, et al., November 10, 1976).

π-μ Decay Background

We estimate here the background from π-μ decay for multi-lepton events. There is a probability $\frac{dP_{\pi\mu}}{dp}$ (p) that a charged-current neutrino interaction will produce a pion of momentum p, which subsequently decays to a muon before interacting in the bubble chamber. We assume that all pions that interact can be rejected as candidate muons. After a length L>>A, the π-μ decay background is

$$\frac{dP_{\pi\mu}}{dp} = \frac{dN_\pi}{dp}\left[\int_o^L e^{-Z/A}\,\frac{dZ}{Dp} + e^{-L/A}\right]$$

$$\longrightarrow \frac{A}{Dp}\,\frac{dN_\pi}{dp} = \frac{.017}{P}\,\frac{dN_\pi}{dp}$$

where A = .97 m = absorption length,

D = 56 m/GeV = pion decay length.

Several groups have measured inclusive hadron production from ν interactions. The results can be parametrized as

$$\frac{dN}{dZ} = N_o\, e^{-Z/Z_o}$$

where $Z = E_\pm/E_H$ and N_o, Z_o = $\begin{cases} 12,\ .19 \text{ for } \nu N \to \pi^+ X \\ 6,\ .17 \text{ for } \nu N \to \pi^- X \end{cases}$

For $\bar{\nu}$ interactions, we assume N_o, Z_o are the same as for ν interactions, but with the sign of the pion reversed.

The number of pions in a unit energy interval is then

$$n = \frac{dN}{dp} = \frac{1}{E_H} \frac{dN}{dZ} = \frac{N_o}{yE_o} e^{-p/Z_o yE_o}$$

where $y = E_H/E_o$ and E_o is the neutrino energy.

The above expression can be averaged over y:

$$\langle n \rangle = \int_o^1 f(y)\, n\, dy = \frac{N_o}{E_o} \int_o^1 f(y) \frac{dy}{y} e^{-y_o/y} = \frac{N_o}{E_o} I(y_o)$$

$$\text{where } f(y) = \begin{cases} 1 & \text{for } \nu \text{ interactions} \\ 3(1-y)^2 & \text{for } \bar{\nu} \text{ interactions} \end{cases}$$

and $y_o = p/Z_o E_o$.

The integral $I(y_o)$ can be expressed in terms of the exponential integral $E_1(y_o)$:

$$I(y_o) = \begin{cases} E_1(y_o) & \text{for } \nu \text{ interactions} \\ 3E_o(y_o)\ [1 + 2y_o + y_o^2/2] - \frac{3}{2}\ (3 + y_o)e^{-y_o} & \text{for } \bar{\nu} \text{ interactions.} \end{cases}$$

The resulting background $\frac{dP_{\pi\mu}}{dp}$ is plotted in Fig. 1 as a function of momentum, for a neutrino energy E_o = 250 GeV. It can be parametrized as

$$\frac{dP_{\pi\mu}}{dp} = N_1 p^{-\alpha},$$

where the fitted parameters are given on Fig. 1. This expression has been integrated to obtain the total π-μ decay background above a 4 GeV energy threshold. Correction has been made for decay kinematics ($p_\mu < p_\pi$). The resulting decay background is:

$$\frac{N_\nu(\mu^+\mu^-)}{N_\nu(\mu^-)} = \frac{N_{\bar{\nu}}(\mu^+\mu^-)}{N_{\bar{\nu}}(\mu^+)} = 2.6 \times 10^{-3}$$

$$\frac{N_\nu(\mu^-\mu^-)}{N_\nu(\mu^-)} = \frac{N_{\bar{\nu}}(\mu^+\mu^+)}{N_{\bar{\nu}}(\mu^+)} = 1.1 \times 10^{-3}$$

These background estimates are to be compared with the observed signals:

$$\frac{N_\nu(\mu^+\mu^-)}{N_\nu(\mu^-)} \sim \frac{N_{\bar{\nu}}(\mu^+\mu^-)}{N_{\bar{\nu}}(\mu^+)} \simeq 1.0 \times 10^{-2}$$

$$\frac{N_\nu(\mu^-\mu^-)}{N_\nu(\mu^-)} \simeq 1.0 \times 10^{-3}$$

This corresponds to a signal/background ratio ~ 4:1 for opposite-sign dimuons, ~ 1:1 for like-sign dimuons. Both ratios can be improved by a factor of ~ 2 by using an energy threshold of 10 GeV.

Hadron Calorimetry

Results on the average spatial distribution of the energy deposited by hadron and electron showers are presented in the proposal. These are useful to study questions of size, active volume, etc. for each module. The computer codes (CASIM & AEGIS) used to calculate these average energy densities are not analogue Monte Carlo codes--they do not permit study of shower-to-shower fluctuations. Hence they cannot calculate the energy resolution of ARGONAUT as a calorimeter.

These and related problems have been studied using the computer code SHOTAM.* This is an analogue Monte Carlo simulation which calculates local calorimeter responses. Figure 2 shows the spectrum of observed ionization in an infinitely long Ar cylinder of 125 cm radius for incident pions of 10, 30 and 100 GeV. The calculation includes effects of ion recombination as discussed in the proposal. The major reasons for the difference between incident and observed energy are (a) energy spent in removing nucleons from Ar nuclei; (b) ion recombination phenomena and; (c) particles escaping radially.

All three contributions to this difference tend to increase as the radial development of the shower increases. Hence it follows that a radial weighting of the energy density should improve the resolution. Radius is measured in ARGONAUT by the arrival time of collected ionization charge. The radial dimension of the Ar cylinder is divided into equal bins. For each bin i, a linear weighting coefficient a_i is calculated by linear regression on a set of hadron showers, viz.,

*A. Van Ginniken, in preparation

$$\langle E_{obs} \rangle = \sum_{i=1}^{N} a_i \; E_{obs}\,(r_i); \quad \sum_{i=1}^{N} a_i = 1$$

where $E_{obs}\,(r_i)$ is the energy observed in a cylindrical shell (r_i, r_{i+1}). Figure 3 shows the spectrum of observed ionization using radial weighting. The improvement in energy resolution is quite substantial. For off-axis interactions and shower divergence a generalized weighting scheme could be devised.

The important point to note is that the resolution can be substantially improved by including in the calorimetry supplementary information. In addition to weighting by radial development, one might weight ionization by its longitudinal development and local density. This could compensate for the larger fraction of energy spent on nuclear binding energy as the shower develops.

One could also weight the measured ionization according to the number of observed energetic ($\geq$ 2 GeV) photons in the shower. Different radial or longitudinal weighting schemes could be employed according to the number of photons present. In general ionization response is expected to decrease in magnitude as the number of photons increases. A simple measure of the energy of electromagnetic showers in the cascade is the sum of squares of the observed energy (hence the ionization density) in a set of radial (time) and longitudinal volume bins. This could be used in lieu of a photon count from the event picture to weight the ionization response.

Several of these strategies are presently being examined using more statistics. Results will be available shortly. It would be of interest to do some quantitative studies on questions

of resolution as a function of incident energy, beam size, beam angle, etc. The effect of sampling in the iron (or uranium) calorimeter at the end of each module will also be examined.

Angle Measurement

The measurement of angle has two sources of error: spatial resolution and multiple scattering. The error in angle is

$$\sigma_\theta^2 = \theta_{meas}^2 + \theta_{m.s.}^2 = (\sigma/L)^2 + (\frac{.014}{p})^2 \, L/X$$

To minimize σ_θ we choose $L_o^3 = 8900 \, \sigma^2 X p^2$

For $\sigma = 10^{-3}$ m, X = .17 m, $L_o^3 = 1.5 \times 10^{-3} p^2$.

This corresponds to an angle error

$$\sigma_\theta \doteq .015 \, p^{-2/3} .$$

For hadrons we typically have a track length L ~ A before interaction. The optimum length L_o < A for p < 25 GeV/c. Above 25 GeV/c, the angle resolution decreases slowly, approaching the limit $\sigma_\theta \to (\sigma/A) \sim .001$

Vidicon Camera

At the time of writing our proposal, recording of bubble chamber images was envisioned using large visual CCD arrays. We observed at the time that such large arrays are not presently available, although they are being developed in industry.

Since that time, we have developed an alternative, based on a new high-resolution vidicon developed by General Electric. This device offers the following features:

1) high resolution: The novel focus-projection-scanning (FPS) design provides an effective scanning beam spot diameter of 6 μm. This is achieved by combining magnetic focus coils with electrostatic deflection. The useful lines resolution is 500 (1" tube), 2000 (1 1/2" tube), and 7000 (3" tube) for the three tube enclosures which have been designed to date.

2) response to bubble chamber illumination: Commercial vidicons are useless for high-resolution bubble chamber photography because the image persistence is only ~ 30 msec. This persistence is achieved in the vidicon by doping the middle layer of the phosphor sandwich with a "flox" to bleed the charge away at the desired rate. It is only in this way that the vidicon can accommodate motion photography. For high resolution recording, the scan time is typically several seconds. An image recorded from a single flash of light would disappear long before the scan was complete.

G.E. has recently developed a slow scan phosphor, in which this "flox" layer is absent. They have tested a 1 1/2" FPS vidicon with slow scan phosphor in conditions approximating those of bubble chamber photography: 400 f.c. illumination for 8 msec. The image of a test pattern is recorded and read out as would be the case on ARGONAUT. They observe a signal current of 250 nA, with a dark current (noise) of ~ 1 nA, and no significant signal degradation during scan time.

G.E. has proposed to develop a complete system incorporating a 3" vidicon (~ 7000 lines resolution) and all camera electronics. The proposed development is described in detail in the enclosure, and will be discussed later.

The Magnetic Field

In our proposal we took the point of view that a magnet for the bubble chambers of ARGONAUT would be prohibitively expensive. We used large magnetized iron toroids to provide total-acceptance muon momentum measurement with $\sigma_p/p \sim 13\%$.

Several features of ARGONAUT would be considerably improved by providing a magnetic field on the bubble chamber volume. Electron identification has a sizable background from e^+e^- pairs converting near the interaction vertex. A dipole field of a few kilogauss would open these pairs, and allow a much improved electron signature. V^o identification would be improved greatly by a similar field; it would be possible to reconstruct the invariant mass, and require the vector momentum sum to point to the interaction vertex.

We have since been motivated by the above considerations (and by the PAC) to examine more carefully the feasability of a magnet for the bubble chambers. In doing so, we adopt a field B = 0.5 T as being sufficient for achieving the improvements in electron and V^o identification described above. Furthermore, as will be shown, this field provides muon momentum analysis which is as good or better than that of the toroids. Thus we require for muon analysis either a $B \gtrsim .5$ T bubble chamber magnet or magnetized iron toroids but not both. This considerably reduces the net cost of adding these magnets to ARGONAUT.

We present here two possible designs for such a magnet. The designs are shown in Fig. 4 . Preliminary cost estimates are presented in Table III.

The first design is for a simple coffin magnet, $(3 \times 3 \times 150)m^3$

enclosed volume. The coil is distributed uniformly along the side walls, and carries a current IN ~ 1 MA turns. The coil and cryostat are housed in a simple steel box, 0.6 m thick, which forms the magnet flux return yoke. Total steel mass is 10,000 T. Whether the coil and cryostat would be made in a single 150 m length or in 10 separate 15 m lengths would depend on cost and design simplicity.

The field of this magnet would be extremely uniform; this facilitates event reconstruction, and avoids eddy current effects in the expansion blade. The magnet would, however, limit access to the bubble chambers, particularly if the coil is wound as a single length. This complicates operation and maintenance.

We have examined a second magnet design which appears ideal in several respects. It consists of a cos ϕ conductor distribution, mounted in a cryostat directly on the double wall of the bubble chamber pressure vessel. The cryostat shares the 120° K bubble chamber structure; the reduced heat load simplifies the insulation design. No magnetic steel is required, except possibly a modest yoke to limit fringe fields. The magnetic pressure (~ 50 psi for .5 T) represents a modest increment to the present 230 psi design pressure of the bubble chamber vessel.

The ~ 10 kA superconductor would be soldered to a hollow square tube to provide local cooling and structural support. The local cooling in particular could be designed to make the saddle coil cryostable. The coil is supported in a separate vacuum enclosure and well anchored by low-leakage stand-offs.

This magnet design would produce a relatively homogeneous field

distribution at low cost. Since the magnet shares the structure of bubble chamber itself, it would not complicate operation and maintenance. We are now performing a field design of the coil distribution, and beginning to examine in detail the mechanical design of the coil/cryostat/pressure vessel assembly.

Momentum Analysis

To analyze the momentum of a track in the bubble chamber, we measure its sagitta in the magnetic field. We assume a magnetic field B = 0.5 T. The bending radius is $R = p/.3B = 6.7p$. The sagitta for track length L is $\Delta = L^2/8R = .019L^2/p$. The momentum resolution is limited mainly by multiple scattering in liquid argon. The r.m.s. sagitta from multiple scattering is $\delta = \frac{.014L}{4\sqrt{3}\ p}\ \sqrt{L/X}$. The momentum resolution is $\sigma_p/p = \delta/\Delta = .26/\sqrt{L}$. For hadron tracks we expect L ~ 1 m, and σ_p/p ~ 26%. For muon tracks we expect L ~ 4 - 10 m (frequently the following module could be used to extend L for muons), and σ_p/p ~ 8 - 13%.

Λ-K Identification and Separation

We calculate here the measurement of the invariant mass of a V^o in an ARGONAUT bubble chamber in a 0.5 T magnetic field. The invariant mass is

$$M^2 = m_1^2 + m_2^2 + 2(E_1E_2 - p_1p_2 \cos\theta) \tag{1}$$

where θ is the lab angle between particles 1, 2. The momentum resolution is σ_p/p ~ .26; the angle resolution is $\sigma_\theta \sim .015\sqrt{(p_1^{-4/3} + p_2^{-4/3})}$. Given m_1, m_2, the mass resolution is

$$\begin{aligned} M^2\sigma_M^2 &\simeq [p_1^2\sigma_{p_1}^2 + p_2^2\sigma_{p_2}^2]\ (1 - \cos\theta)^2 + p_1^2p_2^2\sigma_\theta^2 \sin^2\theta \\ &= p_1^2p_2^2\{.14\ (1 - \cos\theta)^2 + .015^2 \sin^2\theta\ (p_1^{-4/3} + p_2^{-4/3})\} \end{aligned} \tag{2}$$

Let us take a practical case. Suppose we observe a $K_s^o \to \pi^+\pi^-$ decay with $p_K \simeq p_1 + p_2 = 10$ GeV/c, $\theta_{cm} = 30^o$: $p_1 = 8.6$, $p_2 = 1.4$, $\theta = .085$. As discussed in the proposal, the opening angle must satisfy the condition $\theta \sim 0.9/p_K$ within a factor 2 to be considered a strange particle candidate. We furthermore require that the V^o be coplanar with the interaction vertex, and that the vector $\vec{p}_1+\vec{p}_2$ point to the interaction vertex.

Assuming the V^o satisfies the above conditions, we calculate M according to two possible choices for m_1, m_2:

K^o ansatz: $m_1 = m_2 = m_\pi$. Using (1) we obtain an invariant mass $M_K = .50$.

Λ ansatz: $m_1 = m_p$, $m_2 = m_\pi$. Note that we can always assign the proton the larger momentum, simply from decay kinematics. Using (1) we obtain an invariant mass $M_\Lambda = .62$.

The mass resolution from (2) is $\sigma_M = .04$. This resolution is thus fully adequate to identify and separate K_s^o, Λ^o decays. The above analysis assumes that both tracks are well-distinguished from other secondaries, and do not interact for a length ~ 0.5 A. In practice the task of identifying V^o's in the midst of the hadron debris will be a difficult task in ARGONAUT as it is in all bubble chambers.

Experimental Program

The overall program remains as described in the proposal. We describe here in detail Phase I--design and prototype development. This phase constitutes the program for which we need immediate approval.

1) operating characteristics of liquid argon in a bubble chamber: The operations group for BEBC at CERN (in particular G. Linser), is interested in building a small bubble chamber to test the bubble and drift properties of liquid argon. We would like to work with them to design and build the chamber and test it by the spring of 1979. The group at CERN requires a formal statement of interest from Fermilab in order to initiate their own commitment.

2) cryostat design: We propose that Fermilab undertake a consultant agreement with Cryogenic Consultants, Inc. (P. Vander Arend) to prepare a detailed design of the pressure vessel/cryostat/cryogenics system for an ARGONAUT module. We have discussed the requirements with Vander Arend and believe a detailed design could be complete by the end of 1978.

3) expansion system: We propose that Fermilab undertake a consultant agreement with (SLAC) R. Watt and Battelle (M. Vagins) to prepare a detailed design of the expansion system for an ARGONAUT module. We have discussed the system with Watt and believe a detailed design could be complete by the end of 1978.

4) Vidicon camera development: G.E. has made one prototype 1 1/2" FPS vidicon (Z-7802) in their development lab, and tested it to our specifications as described earlier. We propose that Fermilab undertake a contract with G.E. to develop one full camera system--2000 lines resolution--which can be mated to the Ampex video-tape unit already in our possession. The camera would be readily adapted to the 3" FPS vidicon (Z-7803) now being developed. G.E. can deliver one camera 9 months after receipt of contract. We would then test the camera on one spare optics port of the 15' Bubble Chamber and study the image recording system in actual use. We will also require a videotape monitor and display console to study the questions of display, scale manipulation, and reconstruction which were posed by D. Bogert. For these studies we will need a dedicated PDP11 computer.

In Table I we estimate the cost of the prototype and design activities necessary to achieve complete design of an ARGONAUT module. We ask authorization to proceed with these activities immediately, so that we can prepare a full proposal for Phase II--construction of one complete module--by spring, 1979.

We have examined carefully the cost estimate in the proposal. We have modified it as suggested by W. Smart. We have furthermore attempted to verify for each item the actual cost of all commercially available and contract items. In Table II we present the revised cost estimate for Phases II and III. The only major item not easily estimated is the expansion system. A reliable cost there depends on the detailed design proposed for Phase I.

TABLE I

Phase I Cost Estimate

(in $1000)

Cryostat Design (CCI)	25
Expansion System Design (SLAC, Battelle)	25
Vidicon Camera (G.E.)	175
Videotape Monitor	25
	250

TABLE II

REVISED COST ESTIMATES

(in 1000$)

	1 Module	10 Modules
Pressure Vessel		
Stainless steel vessel	83	600
Window structures	100	900
Cooling jacket	10	100
Liquid argon	17	140
Refrigeration		
Cold box	40	200
Argon purifier	20	100
Liquid argon storage	(76)	230
Cryogenic valves and transfer	15	100
Vacuum system	40	320
Expansion System		
Cold gas valves	~100	~1000
Expansion plate/membrane	10	100
Optics		
Fisheye windows	< 250	< 2250
Wide-angle lens	125	625
Film cameras	10	(100)
Vidicon/ CCD cameras	370	1075
Video tape recorder	70	700
Scotchlite	15	150
Flashtubes and supply	12	120
Electronics		
Timing and Synchronization	5	50
500 kV power supply	20	150
500 kV fittings and hardware	10	100
Calorimeter pre-amps	50	360
CCD analog storage, digitizers	40	400
Drift chambers	40	400
Consultants	50	-
Toroids	-	3000
Buildings	-	2000
	1502	15170

TABLE III

Coffin Magnet Cost

Steel (10^4 T)	$ 3.0 M
Superconductor (1 MA turn)	.5
Refrigeration (~ 1 satellite refrigerator)	.5
Cryostat	2.0
Rigging	1.0
20 MY labor	.5
Total	$ 7.5
-Toroids	-3.0
Net Cost	$ 4.5 M

Cos ϕ Magnet Cost

Superconductor	$ 1.0 M
Refrigeration	.5
Cryostat	2.0
20 MY labor	.5
Total	4.0
-Toroids	-3.0
	$ 1.0 M

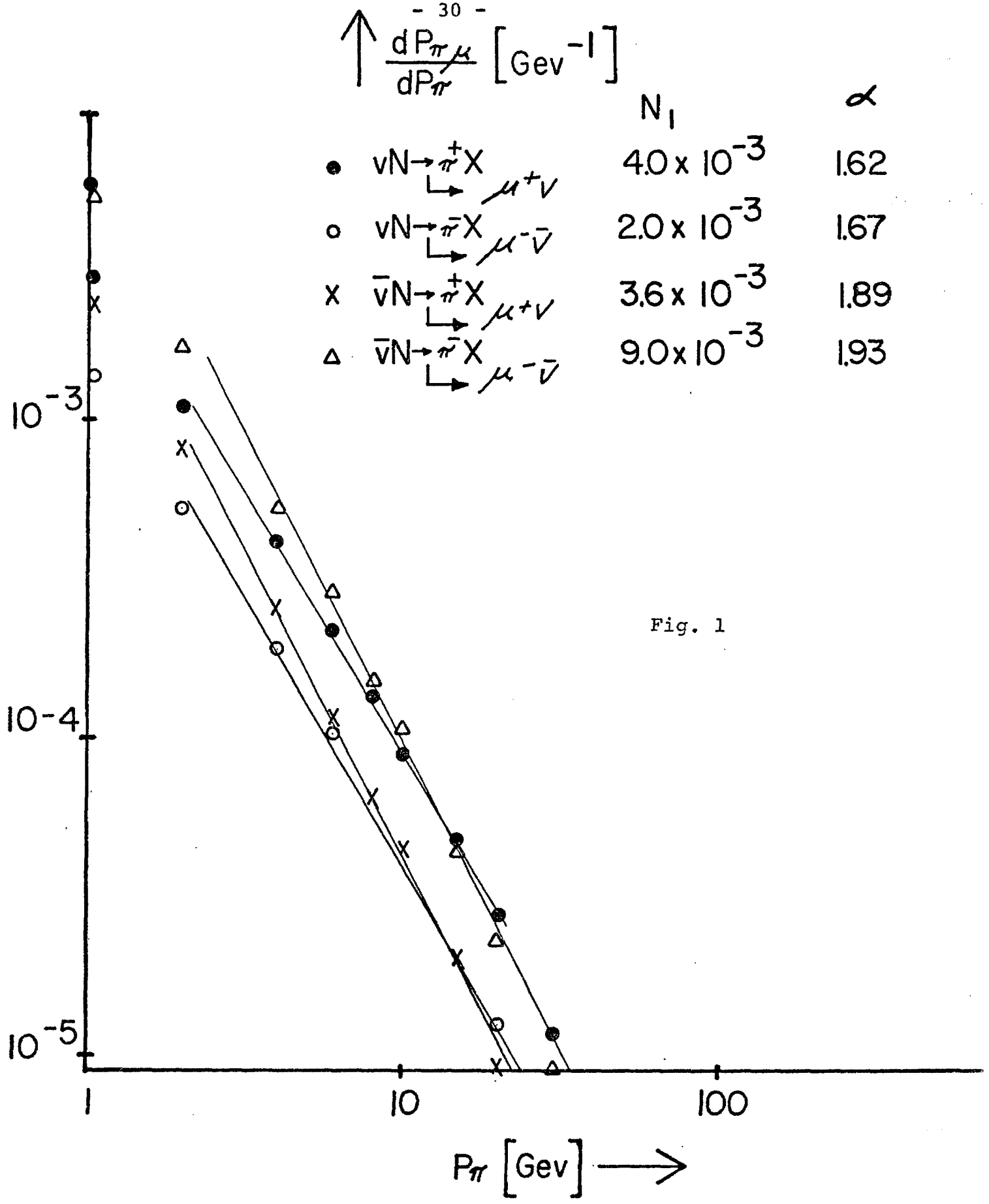
$\frac{dP_{\pi\mu}}{dP_\pi}$ [Gev^{-1}]
N_1
α
$\nu N \to \pi^+ X \to \mu^+ \nu$ 4.0×10^{-3} 1.62
$\nu N \to \pi^- X \to \mu^- \bar{\nu}$ 2.0×10^{-3} 1.67
$\bar{\nu} N \to \pi^+ X \to \mu^+ \nu$ 3.6×10^{-3} 1.89
$\bar{\nu} N \to \pi^- X \to \mu^- \bar{\nu}$ 9.0×10^{-3} 1.93
10^{-3}
10^{-4}
10^{-5}
1
10
100
P_π [Gev] ⟶

Fig. 1

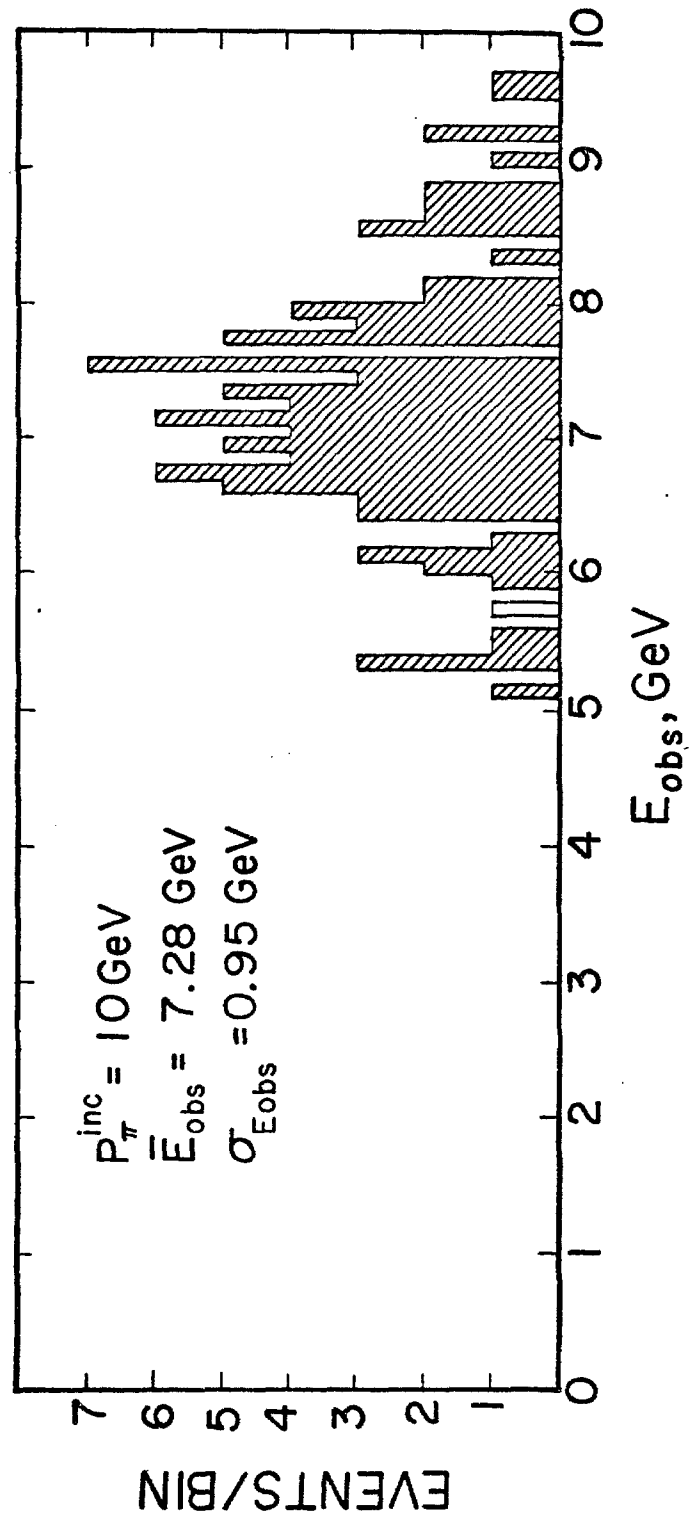
EVENTS/BIN
E_{obs}, GeV
P_{π}^{inc} = 10 GeV
$\bar{E}_{obs}$ = 7.28 GeV
σ_{Eobs} = 0.95 GeV

Fig. 2a

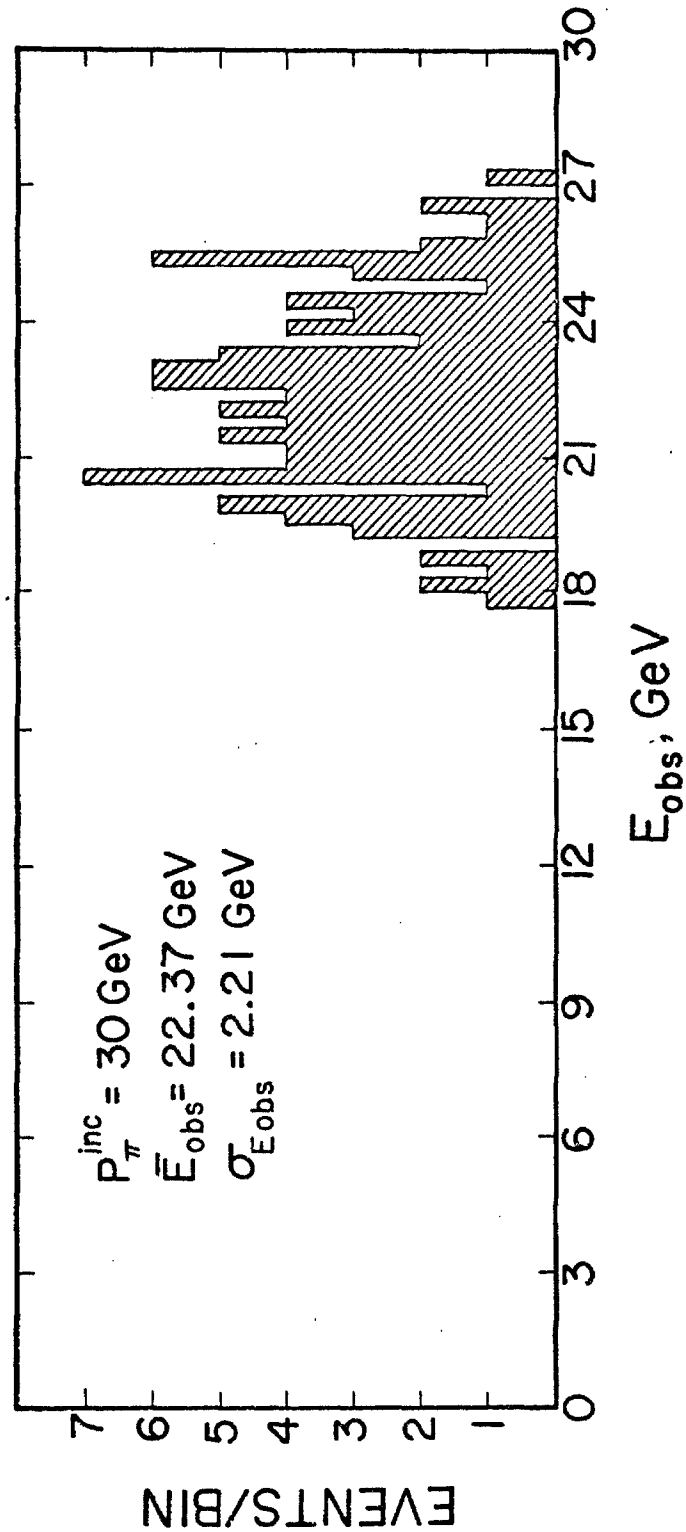
EVENTS/BIN
0
1
2
3
4
5
6
7
0
3
6
9
12
15
18
21
24
27
30
E_{obs}, GeV
P_{π}^{inc} = 30 GeV
$\bar{E}_{obs}$ = 22.37 GeV
σ_{Eobs} = 2.21 GeV

Fig. 2b

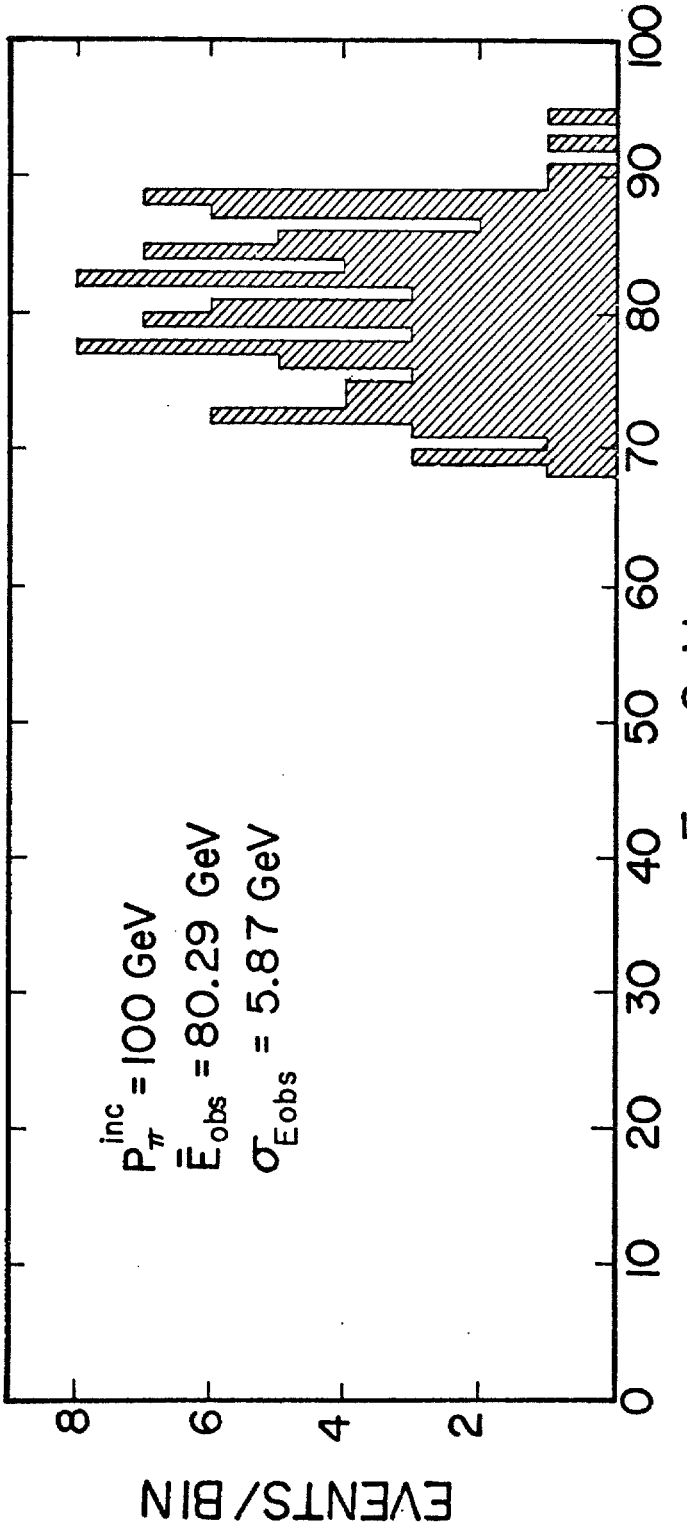
EVENTS/BIN
0
2
4
6
8
0
10
20
30
40
50
60
70
80
90
100
E_{obs} ,GeV
P_{π}^{inc} = 100 GeV
$\bar{E}_{obs}$ = 80.29 GeV
$\sigma_{E_{obs}}$ = 5.87 GeV

Fig. 2c

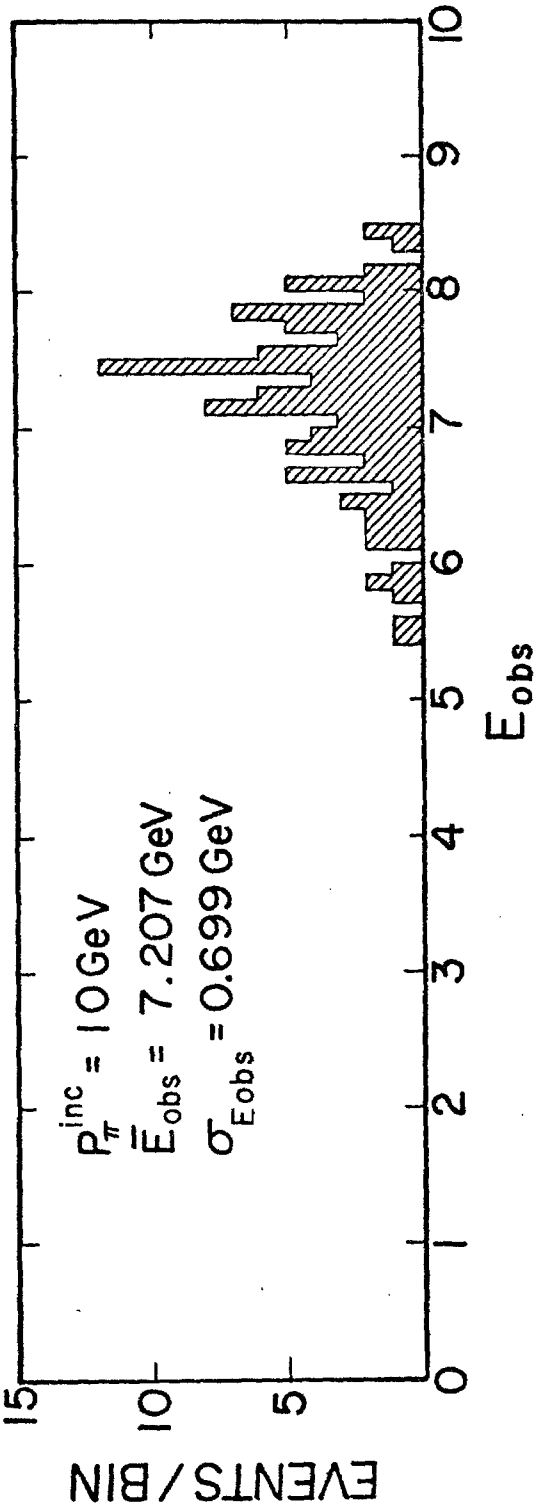
EVENTS / BIN
15
10
5
0
1
2
3
4
5
6
7
8
9
10
E_{obs}
P_{π}^{inc} = 10 GeV
$\bar{E}_{obs}$ = 7.207 GeV
$\sigma_{E_{obs}}$ = 0.699 GeV

Fig. 3a

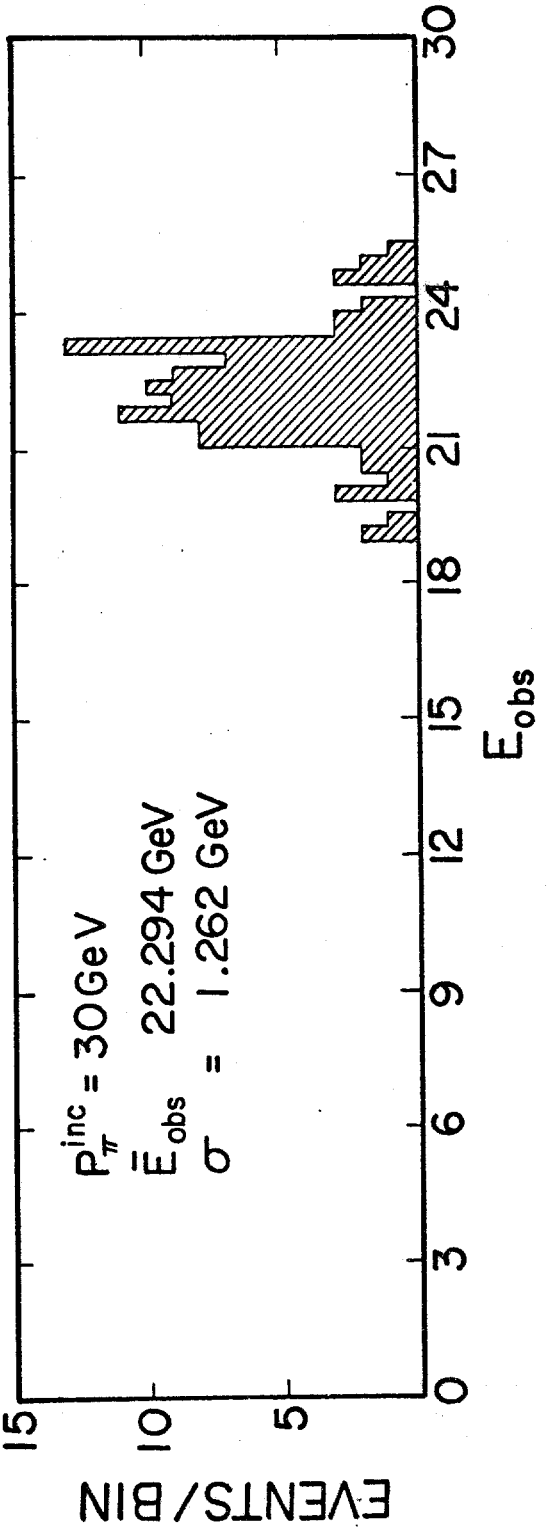
EVENTS/BIN
15
10
5
0
3
6
9
12
15
18
21
24
27
30
E_{obs}
P_{π}^{inc} = 30GeV
$\bar{E}_{obs}$ 22.294 GeV
σ = 1.262 GeV

Fig. 3b

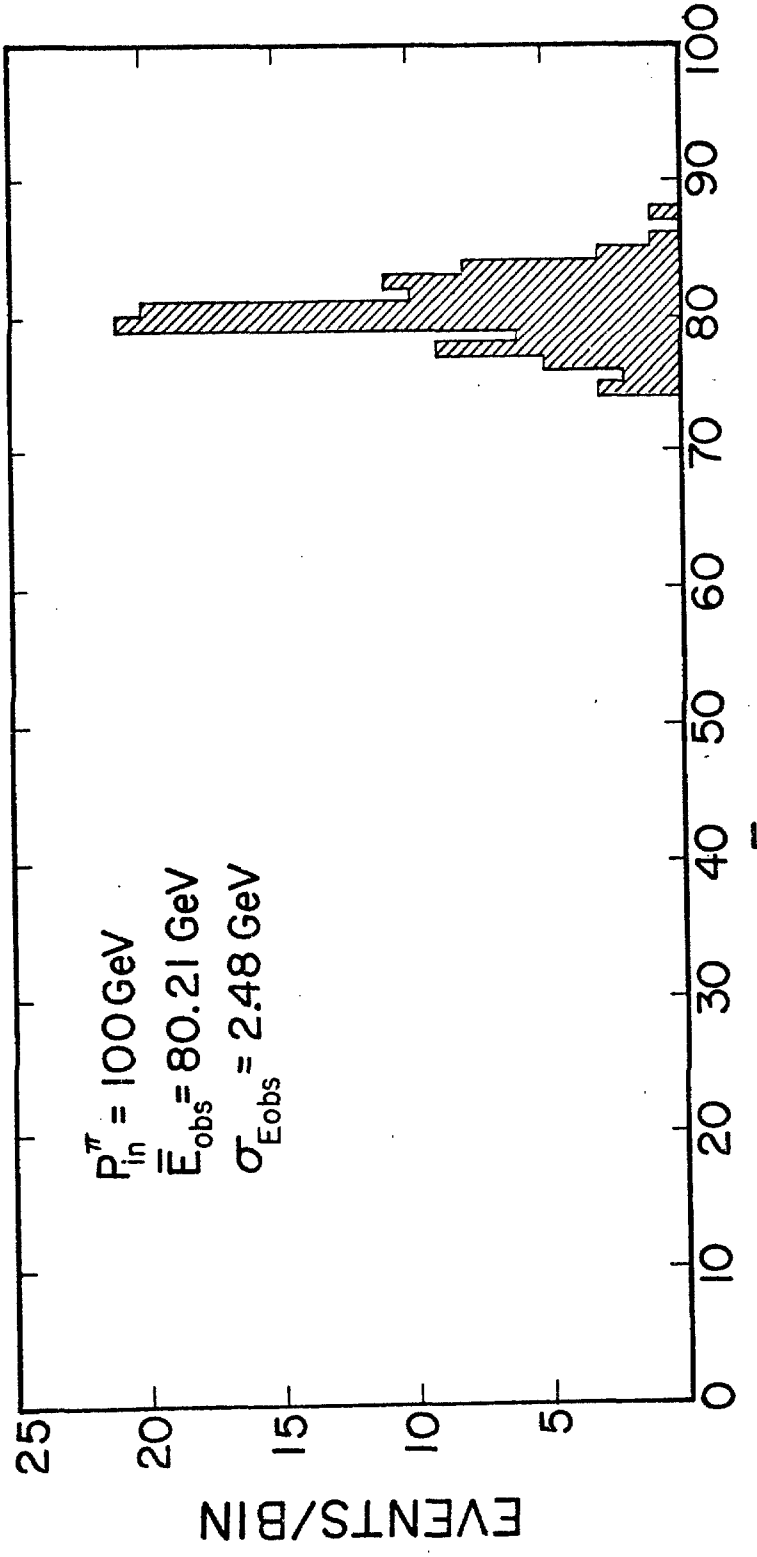
EVENTS/BIN
25
20
15
10
5
0
10
20
30
40
50
60
70
80
90
100
E_{obs}
P_{in}^{π} = 100 GeV
$\bar{E}_{obs}$ = 80.21 GeV
σ_{Eobs} = 2.48 GeV

Fig. 3c

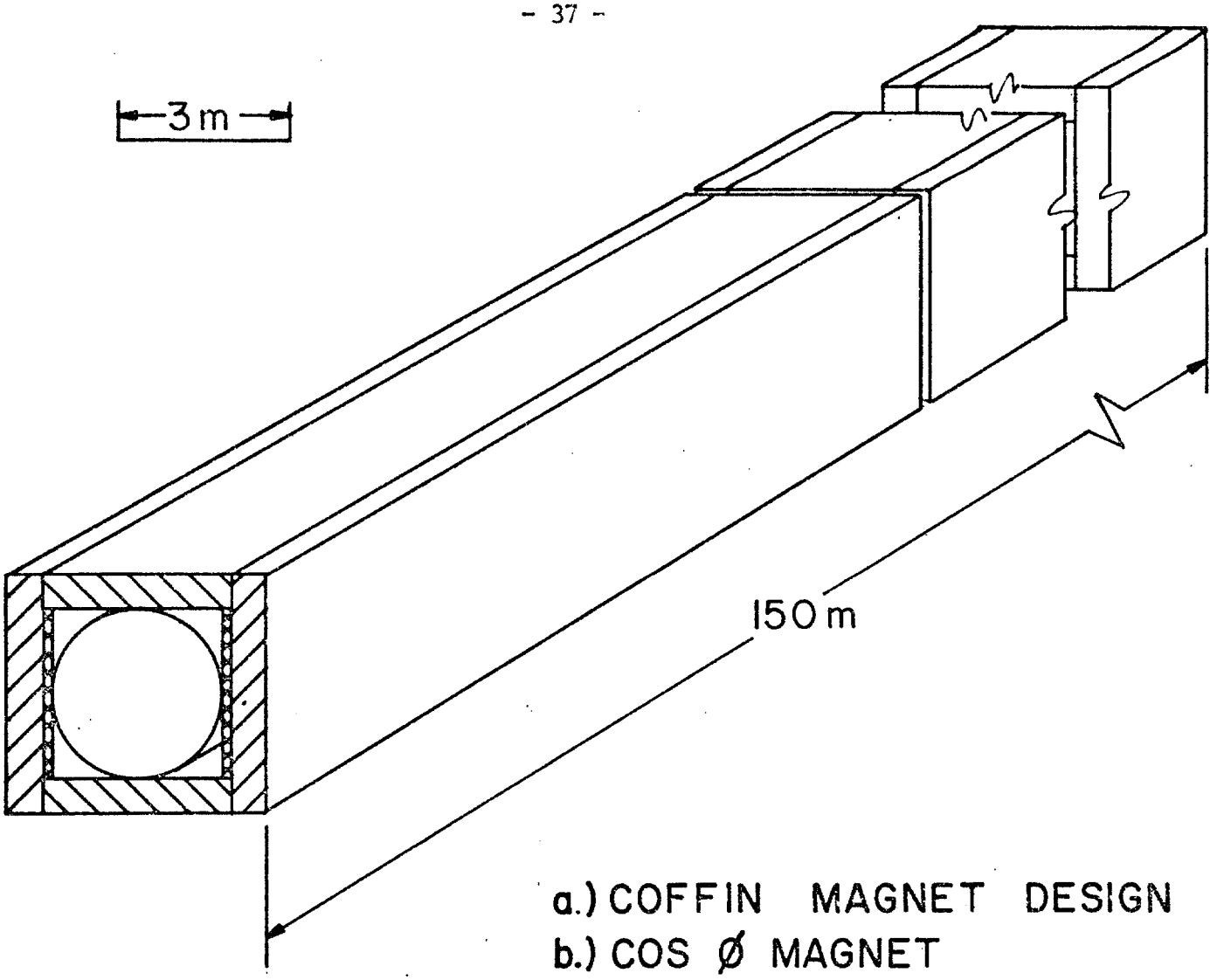

a.) COFFIN MAGNET DESIGN
b.) COS Ø MAGNET

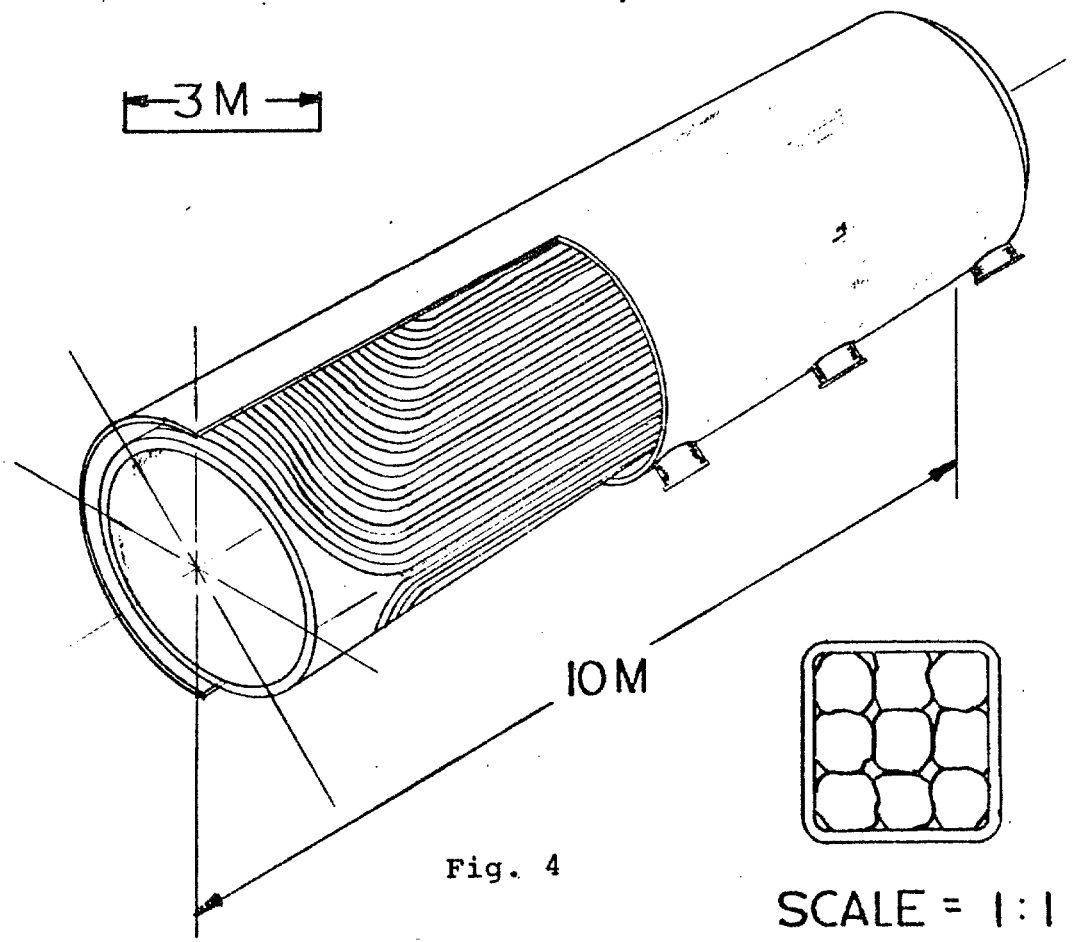

Fig. 4

GENERAL ELECTRIC

GENERAL ELECTRIC COMPANY . . . 3800 NORTH MILWAUKEE AVENUE
CHICAGO, ILLINOIS 60641, Phone (312) 777-1600

ELECTRONIC
COMPONENTS
SALES
DEPARTMENT

June 2, 1978

Mr. Peter M. McIntyre
Fermi National Accelerator Laboratory
P.O. Box 500 Batavia Road
Batavia, IL 60510

Re: High Resolution Camera Proposal for Argonaut

Dear Peter:

Thanks again for your interest in our high resolution CCTV cameras. I would like to confirm our proposal to you for these cameras.

As you recall, we proposed a two piece camera, using a vidicon similiar to our Z7802 except with slo-scan phosphors. The camera would have a minimum of 2000 vertical and horizontal scan line resolution per frame, with a 2 MHZ video output bandwidth. Additionally the camera would be able to respond to a delta function of light 3000 ft.-cdles. by 1 usec. The camera electronics to readout a single frame, non-interlace readout and have a variable gamma. The laboratory would provide the optics and we would specify the flatness of the tube faceplate, and the size of the image area needed on the tube faceplate.

Based upon these preliminary specifications outlined above, we have proposed budgetary estimates (based upon 1978 dollars) for this camera system. When system specifications have been developed, documented and reviewed, we will be able to quote firm prices. As you suggested, we have a three part proposal.

Phase I - Engineering Development and Prototype

We will develop and build one camera for delivery 9 months after receipt of your contract. Engineering development is needed for the camera head design and control unit design including the circuit design for the tube pre-amplifier, deflection, focus, sync generator, and video processing systems.

Additionally some development effort will be needed to use our slo-scan phosphors with the Z7802 FPS vidicon.

Phase I Price Estimate: $175,000.00

Phase II - Production Prototypes

Upon completion of Phase I and acceptance by the laboratory of the Phase I camera, we can build nine additional cameras for delivery four months after receipt of your contract for Phase II cameras.

Phase II Price Estimate: $189,000.00

Phase III - Production Cameras

After completion of Phase II, we can build an additional ninety cameras, delivery to start four months after receipt of a Phase III contract.

Phase III Price Estimate: $810,000.00

The above proposal utilizes our 1½ inch FPS vidicon similiar to our Z7802. As we mentioned at our May 9th meeting, we have done some conceptual development on a 3 inch FPS vidicon that would have higher resolution than the 1½ inch vidicon mentioned above. However, at the present time the 3 inch FPS tube cannot be regarded as an imminently available alternative to the 1½ inch system proposed above.

Present plans indicate 3 inch tube availability in late 1979 to early 1980, with a 3 inch camera availability six to nine months after tube availability.

Because much of the development work needed for the 1½ inch FPS vidicon system as well as the circuit similiarlty between the two systems, any existing 1½ inch FPS cameras could be converted to the 3 inch system. Since the engineering development costs in Phase I are applicable to both the 1½ inch system as well as the 3 inch system, the only additional expenses the laboratory would incur would be the cost of a 3 inch FPS vidicon and the conversion costs.

Camera conversion costs (in 1978 dollars) are estimated to be $1000.00 per camera plus a 3 inch FPS vidicon estimated to be $7000.00 to $9000.00.

Summarily, budgetary price estimates (in 1978 dollars) to convert Phase I, II, and III cameras are listed below.

To convert one Phase I camera: $8000.00 to $10,000.00.

To convert nine Phase II cameras: $72,000.00 to $90,000.00.

For Phase III cameras we expect productivity and material cost improvements due to increased volume, dropping the estimated 3 inch FPS vidicon price to $4500.00. Therefore we can revise our estimate as follows.

To convert ninety Phase III cameras: $495,000.00.

Again, let me emphasize that the 3 inch FPS vidicon is just in the early developmental, conceptual stages and feasibility has not been proven yet. When our engineering group has a higher degree of confidence in building 3 inch FPS tubes, we will modify our present proposal.

However in the interim, I strongly suggest the laboratory approve funds for Phase I utilizing the 1½ inch FPS tube. Since the 1½ inch FPS camera, and 3 inch FPS tube will probably be parallel developments, it is my feeling that most of the Phase III cameras will probably use the 3 inch tube and therefore the laboratory will not incur the total 3 inch conversion costs previously mentioned. Moreover, since the Phase I engineering development costs are applicable to both the 1½ inch as well as 3 inch FPS camera systems, the laboratory, in essence, is only paying for one development, i.e., a specialized FPS camera for your application.

Peter, in closing, I look forward to hearing that the laboratory has approved your Argonaut program and has approved funding for Phase I as described above. Thanks again for this opportunity and I am hoping to be able to begin the specification discussions at your earliest convenience, so we can start to implement Phase I as soon as possible.

Sincerely yours,

John R. Siefkin
JRS: da